University of Tennessee, Knoxville
TRACE: Tennessee Research and Creative Exchange

Doctoral Dissertations | Graduate School

5-2023

Synchrotron infrared spectroscopy of domain walls and high pressure phases of multiferroics

Kevin A. Smith Jr
University of Tennessee, Knoxville, ksmit162@vols.utk.edu

Follow this and additional works at: https://trace.tennessee.edu/utk_graddiss

Recommended Citation

Smith, Kevin A. Jr, "Synchrotron infrared spectroscopy of domain walls and high pressure phases of multiferroics. " PhD diss., University of Tennessee, 2023.
https://trace.tennessee.edu/utk_graddiss/8167

This Dissertation is brought to you for free and open access by the Graduate School at TRACE: Tennessee Research and Creative Exchange. It has been accepted for inclusion in Doctoral Dissertations by an authorized administrator of TRACE: Tennessee Research and Creative Exchange. For more information, please contact trace@utk.edu.

To the Graduate Council:

I am submitting herewith a dissertation written by Kevin A. Smith Jr entitled "Synchrotron infrared spectroscopy of domain walls and high pressure phases of multiferroics." I have examined the final electronic copy of this dissertation for form and content and recommend that it be accepted in partial fulfillment of the requirements for the degree of Doctor of Philosophy, with a major in Chemistry.

Janice L. Musfeldt, Major Professor

We have read this dissertation and recommend its acceptance:

Craig E. Barnes, Sharani Roy, Bin Hu

Accepted for the Council:

Dixie L. Thompson

Vice Provost and Dean of the Graduate School

(Original signatures are on file with official student records.)

Synchrotron infrared spectroscopy of domain walls and high pressure phases of multiferroics

A Dissertation Presented for the

Doctor of Philosophy

Degree

The University of Tennessee, Knoxville

Kevin A. Smith

May 2023

© by Kevin A. Smith, 2023
All Rights Reserved.

Acknowledgements

First and foremost, I would like to thank my advisor Professor Janice L. Musfeldt for her unending support and guidance throughout my graduate studies. The numerous discussions we have had over the years have shaped me as a scientist, and her vast knowledge spanning the topics of chemistry, physics, and material science has proved an invaluable resource during my time as her student.

I am grateful for Professors Sharani Roy, Craig Barnes, and Bin Hu for serving on my committee and for their continued interest in my work and professional development.

I wish to acknowledge all of members of our research group: Judy Cherian, Amal al-Wahish, Yanhong Gu, Ken O'Neal, Brian Hollinsworth, Michael Yokosuk, Amanda Clune, Shiyu Fan, Nathan Harms, Sabine Neal, Avery Blockmon, Kiman Park, Ashley Glover, Brian Taylor, Sambridhi Shah, and Brandon Chapman for their collaboration, encouragement, and support over the years. I am thankful for all of the faculty and staff in the Department of Chemistry that have helped during my time as a graduate student.

I also would like to thank all of my many collaborators including: Drs. Elizabeth Nowadnick, Larry Carr, Michael Martin, Hans Bechtel, Stephanie Gilbert Corder, Sang-Wook Cheong, Zhenxian Liu, Omar Khatib, Kai Du, Sriram Ramkumar, and Steve McGill for all of the amazing discussions over the years which have shaped and guided me.

I would like to thank my mom, dad, great-grandmother, and friends that have always been my greatest advocates. Finally, I thank my partner Greyson Dickey and our three cats for their abiding love and compassion. I would never have been able to complete my degree without all of their support, patience, and encouragement.

Abstract

Synchrotron light sources provide high throughput, broadband infrared light enabling the development of novel techniques, inaccessible using traditional sources. High pressure techniques benefit greatly, as significant signal loss occurs from focusing the light through diamonds into a small area. Intense infrared light offers an avenue to perform spatially-resolved spectroscopy in areas smaller than the diffraction limit by focusing the light within the near-field limit. We take advantage of the synchrotron light source to perform infrared studies at high pressures and on spots smaller than 20×20 nm^2. We investigate nanoscale heterogeneity with spatially resolved techniques and reveal pressure-induced phase transitions via high pressure spectroscopy. We then unravel these complicated findings by incorporating group theoretical symmetry analysis and lattice dynamics calculations. The utilization of a synchrotron light source offers the broadband, high throughput infrared light that unifies these projects and enables the understanding of how vibrational modes contribute to unexplored phenomena.

Because multiferroic materials exhibit heterogeneity in the form of domains and domain walls, $Ca_3Ti_2O_7$ and h-$Lu_{0.6}Sc_{0.4}FeO_3$ provide platforms to reveal the infrared response of different domain walls. These nanoscale objects have eluded study due to their size, but near-field infrared spectroscopy provides an opportunity to investigate domain walls, by performing a line scan over a wall of interest. We reveal that the domain walls widths in $Ca_3Ti_2O_7$ and h-$Lu_{0.6}Sc_{0.4}FeO_3$ are 60-100 nm wide and remain insulating.

We perform high pressure infrared spectroscopy to reveal pressure-induced structural phase transitions. Combined with symmetry analysis and complimentary lattice dynamics calculations, we assign high pressure phases by comparing experimentally observed changes in the vibrational response with predicted mode patterns for a series of candidate space

groups. For the case of hybrid improper ferroelectric $Sr_3Sn_2O_7$, we discover that the set of structural phase transitions as a function of pressure mirror the reported sequence as a function of temperature. A similar analysis is performed on multiferroic h-$Lu_{0.6}Sc_{0.4}FeO_3$. We reveal a structural transition from a polar $\rightarrow$ antipolar space group at 15 GPa. We relate this distortion to changes in the bipyramidal tilting modes and competing structural trends in this linear magnetoelectric ferrite.

Table of Contents

1 Introduction **1**

1.1 Traditional polar materials 1

1.2 Traditional displacive and order-disorder ferroelectric materials 2

1.3 Improper ferroelectric oxides 2

1.4 Hybrid improper ferroelectrics and the Ruddlesden-Popper series 5

1.5 Domain and domain walls 6

1.6 Pressure-induced phase transitions 7

1.7 Synchrotron-based spectroscopy 8

1.7.1 Spatially resolved techniques using synchrotron radiation 8

1.8 Improper and hybrid improper ferroelectrics of interest in this work 9

1.8.1 The n=2 members of the Ruddlesden-Popper series 9

1.8.2 The hexagonal rare earth ferrite h-$Lu_{0.6}Sc_{0.4}FeO_3$ 11

1.9 Outline of this thesis 12

2 Literature survey **21**

2.1 Ferroelectric oxides 21

2.2 Development of new ferroelectric oxides 23

2.2.1 Perovskite-derived oxides 24

2.2.2 Improper ferroelectrics 26

2.2.3 Towards more modern layered multiferroic oxides with hybrid improper mechanisms 27

2.3 Project specific details 28

2.3.1 Domains and domain walls 28

2.3.2 Pressure-induced phase transitions in the various families of ferroelectrics 30

3 Methods **42**

3.1 Spectroscopic techniques 42

3.1.1 Beer-Lambert law 42

3.1.2 Fourier transform infrared spectroscopy 43

3.1.3 Raman scattering spectroscopy 44

3.1.4 Far and near-field spectroscopy: the diffraction limit & spatial resolution 46

3.2 Synchrotron-based spectroscopy 47

3.2.1 High pressure spectroscopy using a diamond anvil cell 47

3.2.2 High pressure infrared spectroscopy 50

3.2.3 Near-field infrared nanospectroscopy 50

3.3 Project specific details: growth, measurement, and theoretical calculations . 51

3.3.1 Crystal growth 51

3.3.2 Mapping and locating domain walls 51

3.3.3 Spectroscopic measurements 53

3.3.4 Lattice dynamics calculations and group theoretical analysis 64

4 Infrared nano-spectroscopy of ferroelastic domain walls in hybrid improper ferroelectric $Ca_3Ti_2O_7$ **66**

4.1 Structure and order parameters across the domain boundary 67

4.2 Locating domain walls in different fields of view 69

4.3 Near-field imaging of ferroelastic domain walls 69

4.4 Relating near-field amplitude to the order parameters 74

4.5 Order parameter trends vs. near-field response of ferroelastic domain walls . 76

5 Revealing pressure-driven structural transitions in hybrid improper ferroelectric $Sr_3Sn_2O_7$ **79**

5.1 Infrared properties of $Sr_3Sn_2O_7$ 79

5.2 Understanding the symmetry of the high pressure phases 83

5.3 Structure-property relations in $n = 2$ Ruddlesden Popper hybrid improper ferroelectrics 92
5.4 Developing the schematic temperature-pressure phase diagram of $Sr_3Sn_2O_7$. 97

6 Pressure-induced phase transition and phonon softening in h-$Lu_{0.6}Sc_{0.4}FeO_3$ 100
6.1 Infrared response of $Lu_{0.6}Sc_{0.4}FeO_3$ under pressure 100
6.2 Raman scattering response under pressure 107
6.3 Structure-property relationships and comparison with the rare earth manganites and other materials 111

7 Real space infrared spectroscopy of ferroelectric domain walls in multiferroic h-(Lu,Sc)FeO_3 114

8 Summary and outlook 125

Vita 145

List of Tables

1.1 Summary of spontaneous polarization values for select ferroelectrics. Values are reported from Refs. [5, 6, 7, 8, 9, 10, 11] 3

3.1 Operational parameters for Bruker IFS 113v 57

3.2 Operational parameters for infrared microscopy 60

5.1 Calculated Γ-point phonon frequencies (in cm^{-1}) of the $Sr_3Sn_2O_7$ $A2_1am$ phase. 82

5.2 Tolerance factor (τ) and amplitudes of the X_3^- and X_2^+ octahedral rotations for selected n=2 members of the Ruddlesden-Popper series. The octahedral rotation amplitudes are obtained by decomposing ambient pressure $A2_1am$ structures with respect to the high-symmetry $I4/mmm$ structure, and are reported for a 24 atom cell in units of Å. The tolerance factors were calculated using A-O and B-O bond lengths obtained from the bond valence model [100, 101, 102], assuming 12- and 6-fold coordination for the A and B cations, respectively. The experimental values–except the P_C for $Sr_3Sn_2O_7$ reported in this work–were obtained from literature [103, 104, 105, 106, 81, 82]. 95

6.1 Summary of mode assignments for h-$Lu_{0.6}Sc_{0.4}FeO_3$ at ambient conditions in the $P6_3cm$ space group. For assignments containing both Lu and Sc, we list the frequency of the Lu mode first. Table is reproduced from [28]. 102

List of Figures

1.1 The (a) displacive ferroelectric mechanism and its unperturbed paraelectric structure are provided to illustrate how the Ti atom displaces to generate the polarization. The (b) ferroelectric hysteretisis loop obtained from a thin film heterostructure of $PbTiO_3$ and $SmFeO_3$ demonstrates its switchable nature. Reproduced from Refs. [12, 13] 4

1.2 A modified version of the classical displacive mechanism takes place in $BiFeO_3$. Instead of being driven by the displacement of the B-site atom, the motion of a lone pair of electrons from Bi induces the polarization. Reproduced from Ref. [14]. 13

1.3 The orthorhombic $Pbnm$ (a) and hexagonal $P6_3cm$ (b) phases of $R\mathrm{MnO}_3$. The A-site atoms are provided as green spheres, with oxygen in orange and manganese in purple. Image reproduced from Ref. [19]. 14

1.4 (a) Counterclockwise and (b) clockwise cycloidal spin structure which generate the improper ferroelectric polarization. The (c) canted antiferromagnetic magnetic structure is another related magnetic arrangement that generates a spontaneous polarization. Image reproduced from Ref. [18]. 15

1.5 The $A2_1am$ ground state structure of $Ca_3Mn_2O_7$ is provided in (a). The shematic of the octahedral rotation (b) and tilt (c) responsible for obtaining the ground state structure from the $I4/mmm$ parent structure are given on the right. Image reproduced from Ref. [21]. 16

1.6 (a,b) Two views of the $A2_1am$ ground state structure in $Ca_3Ti_2O_7$ showing how the Ca atoms from the rock salt (R) layer displace oppositely to the Ca in the perovskite (P) layer to generate the net dipole moment. Image reproduced from Ref. [22]. 17
1.7 (a) Image of ferroelastic twin domains are provided alongside (b) the piezo-force response of ferroelectric and ferroelastic boundaries in $Ca_3Ti_2O_7$. Image reproduced from Ref. [22]. 18
1.8 (a) Summary of beamlines at the Advanced Light source and (b) a comparison of the infrared spectral coverage of the synchrotron and other commercially available sources. The red dashed line is the theoretical brightness of the synchtrotron and the solid curves are the coverage using different sources. The main feature to note is the brightness of the synchrotron is many orders of magnitude more than a classic blackbody source. Image reproduced from Ref. [24]. 19
1.9 Images of (a) stripe and (b) vortex domain patterns and the (c) optical conductivity and Born effective charge calculated from reflectance measurements in $ErMnO_3$. Image reproduced from Ref. [25]. 20

2.1 Summary of the different symmetry requirements for the different ferroic orders. Image reproduced from Ref. [37]. 25
2.2 (a) Plot of the lattice constant a as a function of A-site ionic radius for selected $RMnO_3$ systems. (b) Magnetic phase diagram for different rare earth manganites as a function of temperature. Images reproduced from Refs. [38, 39]. 33
2.3 The spontaneous polarization of $TbMnO_3$ as a function of temperature at various pressures and magnetic fields shows a distinct enhancement above 5 GPa. Image reproduced from Ref. [9]. 34
2.4 The different types of (a) ferroelectric and (b) magnetic domain walls present in materials are given. Image reproduced from Ref. [47, 49]. 35

2.5 The (a) ferroelastic domain walls in $Sr_3Sn_2O_7$ are visualized using polarized transmission optical microscopy. (b,c) Two different orientations of piezo-force microscopy images of ferroelectric walls in $Sr_3Sn_2O_7$ reveal the ferroelectric domains within ferroelastic domains. A (d) composite image of (b,c) shows all combinations of ferroelastic and ferroelectric domains. Images (b-d) reproduced from Ref. [50]. 36

2.6 The ferroelectric hysteresis loop characterizes the switchability and magnitude of the polarization in h-$Lu_{0.6}Sc_{0.4}FeO_3$. Image reproduced from Ref. [52]. . . 37

2.7 (a) AFM topography of h-$Lu_{0.6}Sc_{0.4}FeO_3$ reveals a flat spot suitable for PFM (c) and cAFM (d). (b) Provides the topological defect density as a function of cooling for a few different ferroelectrics. Piezo-force mapping reveals ferroelectric domains with strong contrast. The cAFM map reveals ferroelectric domain walls with significant widths that are more conducting than their surroundings. Image (b) reproduced from Ref. [52]. 38

2.8 (a) Subgroup relations are provided for the $R\bar{3}c$ space group with high-pressure polar phases indicated in blue and red corresponding to the (b) phase diagram. Images reproduced from Ref. [10]. 39

2.9 (a) Neutron diffraction results of the normalized intensity of the (1,2,0) and (0,3,3) reflections which correspond to the octahedral rotation and tilt distortion for $Ca_3Mn_{1.9}Ti_{0.1}O_7$ reveal a phase transition at 7 GPa. (b) The calculated change in the rotation and tilt angles as a function of pressure is also provided. Image reproduced from Ref. [56]. 40

2.10 The (a) orthorhombic and (b) hexagonal phases of $LuFeO_3$ are provided alongside the (c) pressure dependence of the spin-crossover. Images reproduced from Ref. [57]. 41

3.1 Typical schematic view of a Michelson interferometer used in a Fourier transform infrared instrument. 45

3.2 (a) Typical schematic view of a diamond anvil cell showing beam passing through the diamonds (red), the ruby for pressure calibration (red circle) and sample (blue oval) loaded into a gasket (grey rectangle) with a pressure transmitting medium. (b) Low profile (left) and standard (right) diamond anvil cells used in this work. (c) Typical ruby fluorescence shows the clear separation of peaks at various pressures. 48
3.3 A schematic of the near-field infrared nanospectroscopy setup at the Advanced Light Source at Lawrence Berkeley National Lab [24]. The MCT detector is replaced by a far infrared, helium cooled Cu/Ge bolometer detector for low frequency (320-800 cm^{-1}) measurements. 52
3.4 (a) Optical (top) and cross-polarized transmittance images of $Ca_3Ti_2O_7$ reveal domain walls a straight, parallel lines. Cross-polarized image clearly shows the different ferroelastic domains in red and gold. (b) Domain walls are imaged using the camera attached to an atomic force microscope prior to measurements. 54
3.5 (a) Optical images of the crystal surface showing the location of interest. (b) Topographical map of h-$Lu_{0.6}Sc_{0.4}FeO_3$ obtained by atomic force microscopy. (c) Piezo-force microscopy reveals ferroelectric domains in the same region scanned in (b). The same gold marker appears in the top right corner of each image and is used to ensure the proper position is maintained. 55
3.6 Bruker113v IFS spectrometer schematic showing the main components. . . . 58
3.7 Bruker Equinox 55 spectrometer optical path diagram with primary components labeled. 1,16-visible light source; 2,19- visible light aperture; 3,22-motorized switch mirror; 4,18- optional iris or knife edge aperture; 5,9,10,17-beamsplitter changer; 6- Objective lens; 7- Sample; 8- Iris or knife edge aperture which defines the area of sample analyzed; 12- binocular eyepiece; 13- two position detector selection mirror; 14- mirror routing to detector; 15-detector; 20- condenser; 21- IR beam (from spectrometer); 23,24-camera port; 25,26,27- polarizer. 59
3.8 Near-field infrared set-up at the Advanced Light Source beamline 5.4. 63

3.9 High pressure far infrared instrumentation at NSLS-II 22-IR-1 beamline. . . 65

4.1 **Bulk crystal and ferroelastic domain wall structure.** (a) Crystal structure of $Ca_3Ti_2O_7$ (space group $A2_1am$). The two $CaTiO_3$ perovskite slabs are shown in light and dark grey, with the Ca cations in light blue. The structure of the two orthorhombic twin domains is shown in (b) real space and (c) order parameter space. The order parameters for the X_3^- octahedral tilt and X_2^+ octahedral rotation are shown with blue and red arrows, respectively, in (c) and the corresponding atomic motions are highlighted using the same colors in (b). The bold black arrows show the setting of the orthorhombic relative to the tetragonal axes. The rotation direction of the Γ_5^- order parameter is indicated by the arrows with a P, indicating polarization direction, above the structures. Upon crossing a ferroelastic domain wall, the octahedral rotation order parameters rotate by 90°; at the midpoint, the local structure is space group $C2mm$. (d, e) The order parameter amplitudes are plotted as a function of the normalized wall width. These amplitudes (reported for a $Z = 2$ cell) were obtained using Density Functional Theory calculations of a trajectory through the bulk energy surface. The units of these structural order parameters are distance (in Å) because they are measuring the amount of distortion - which is calculated by adding up how much all of the atoms in the unit cell are displaced from their high symmetry positions [26]. 68

4.2 **Combining microscopy techniques to locate domain walls.** (a, b) Atomic force microscopy (AFM) images of the crystal surfaces showing the two ferroelastic domain walls of interest (at the edges of the dark blue stripes). These ferroelastic walls separate domains of different spontaneous strain and are also 90° ferroelectric walls. DW 1 and DW 2 refer to domain walls 1 and 2. Red arrows indicate direction and path of the line scans. The nano-spectroscopic line scans are taken perpendicular to the wall, and the contact angle from one domain to another is 90°. (c) AFM topography of a smooth area near an identified surface defect (indicated by a green circle) and step edge of approximately 100 nm height (indicated with a red arrow) compared with (d) the piezoresponse force microscopy (PFM) image of the same area revealing the placement and orientation of the 180° ferroelectric domains, indicated by yellow(+) or blue(-) regions with black or white arrows to indicate the polarization direction). All of these structures are present at room temperature [26]. 70

4.3 **Near-field infrared spectroscopy of $Ca_3Ti_2O_7$.** (a, b) Contour plots of the near-field amplitude normalized to a gold reference across two different domain walls as indicated in Fig. 4.2(a, b). We label these walls as DW 1 and DW 2. The step size is 20 nm, and the tip resolution is 20 × 20 nm^2. The black dashed lines indicate the domain wall locations, and the brackets denote effective wall widths. (c) Fixed distance cuts of the contour spectra in panel (b) show $A(\omega)$ at the ferroelastic domain wall compared with two different point scans away from the wall. Average changes in the near-field amplitude, calculated as $\Delta\bar{A}(\omega) = \bar{A}(\omega)_{\text{DW 2}}$ - $\bar{A}(\omega)_{\text{Domain}}$, reveal the difference and, at the same time, reduce the noise. Here, the bars denote an average response. This analysis demonstrates that wall phonons have reduced amplitude and a slight blue shift. The 6 A_1 modes within the experimental energy window are indicated by double-sided orange arrows. (d) Fixed frequency cuts of the contour data in panel (b) showing how intensity at 460 and 640 cm^{-1} varies across DW 2. According to the calculation of $\Delta\bar{A}(\omega)$ in panel (c), these frequencies are most sensitive to the presence of the domain wall. They are also very near the calculated A_1 symmetry vibrational modes (shown as orange arrows in panel (c)). 71

4.4 **Phonon overlaps and calculated displacement patterns.** (a) The 19 A_1 symmetry phonon eigenvectors projected onto the $I4/mmm$ symmetry adapted modes. The labels are the calculated phonon frequencies. (b-e) Atomic displacement patterns of four selected phonons from (a). The black arrows display the largest atomic motions within each displacement pattern. The 428 cm^{-1} and 466 cm^{-1} phonons largely consist of Ti-O-Ti bond angle bends. The 546 cm^{-1} and 652 cm^{-1} phonons are bond-stretching modes in the *ab* plane and along the *c*-axis, respectively [26]. 75

4.5 **Order parameter trends across the structural domain wall.** (a-d) Comparison of predicted X_3^- (tilt, blue diamonds) and X_2^+ (rotation, red triangles) order parameters with the measured near-field amplitude at 460 and 640 cm^{-1} across the two walls of interest from Fig. 3(a, b). Both the normalized distance across each wall (treated here as a scalable parameter) as well as the actual line scan positions (determined from the near-field response) are shown. The microscopic distortions across the wall relax more slowly than topography would suggest [26]. 77

5.1 (a) Infrared response of $Sr_3Sn_2O_7$ measured using traditional spectroscopic techniques at 300 K (black) and inside the diamond anvil cell at ambient pressure (green). Colored symbols indicate predicted mode positions, symmetries, and intensities. (b) Infrared response of $Sr_3Sn_2O_7$ under pressure at room temperature. The curves are offset for clarity only. The color scheme denotes the four structural phases. The labels α, β, and γ indicate the 150, 225 and 280 cm^{-1} features, respectively, as mentioned in the text. (c) Frequency vs. pressure plot of selected modes that show the critical pressures $P_{C,2}$ and $P_{C,3}$. The filled and open circles denote separate runs. Error bars are on the order of the symbol size. (d) Contour plot of the data in panel (b). The vibrational features of the ambient pressure phase and the critical pressures are labeled [27]. 81

5.2 Structural phases of $Sr_3Sn_2O_7$ that are accessible via temperature [81] and pressure. Starting with the high-symmetry parent structure $I4/mmm$, the condensation of $a^0a^0c^-$, $a^-a^-c^0$, and $a^0a^0c^+$ octahedral rotation patterns leads to structures with $Acaa$, $Amam$, and $Acam$ symmetries, respectively. The symmetries of these octahedral rotations are given by irreducible representations of $I4/mmm$ as indicated. Combining the $a^-a^-c^0$ and $a^0a^0c^+$ rotations leads to the polar $A2_1am$ structure, whereas combining $a^-a^-c^0$ and $a^0a^0c^-$ rotations leads to the $Pnab$ structure. In each of these structures, a third distortion, primarily consisting of Sr displacements, is induced by a coupling to the octahedral rotations. In $A2_1am$, there is a net Sr displacement in each perovskite layer (green arrows), leading to a polarization, whereas in $Pnab$ the displacements in each layer cancel (blue arrows) [27]. 84

5.3 Structural phases of $Sr_3Sn_2O_7$ considered in this work. The X_2^+, X_3^-, and X_1^- irreducible representations of $I4/mmm$ generate the space groups shown in the top row, while their combinations generate the space groups in the bottom row. The order parameter directions that define each space group are to the left of the space group symbol (color coded with the relevant irreducible representation). The total energies obtained from DFT structural relaxations of $Sr_3Sn_2O_7$ with symmetry constrained to each of these space groups are given in meV per formula unit with respect to the $I4/mmm$ energy [27]. . . 85

5.4 Infrared spectrum of $Sr_3Sn_2O_7$ in the HP1 high pressure phase at 11.9 GPa compared with computed mode positions, symmetries, and intensities for three candidate space groups. The space groups considered are: (a) $C2/c$, (b) $Pnam$, and (c) $Pnab$. $Pnab$ provides the superior match in terms of most prominent features and overall pattern - as indicated by the heading in red [27]. 86

5.5 (a) Infrared reflectance of $Sr_3Sn_2O_7$ as a function of temperature across $T_{C,1}$. The curves are shifted for clarity. (b) Reflectance differences highlighting the temperature-induced spectral changes across $T_{C,1}$. The green and red curves correspond to the $A2_1am$ and $Pbna$ phases, respectively [27]. 88

5.6 (a) Main atomic motions that contribute to the $B_1(1)$ phonon of $Sr_3Sn_2O_7$ in the $A2_1am$ structure. (b) Predicted evolution of the frequency of the $B_1(1)$ phonon with pressure [27]. 90

5.7 Infrared spectrum of $Sr_3Sn_2O_7$ at 16.85 GPa (blue curve) taken in the diamond anvil cell compared with calculated mode positions and intensities for four candidate space groups. Calculated vibrational modes and intensities for $I4/mmm$, $Amam$, $P4_2/mnm$, and $Acaa$ space groups as compared with the measured spectrum. Symmetries of theoretically predicted modes are given by colored markers. (a, c) For $I4/mmm$ and $P4_2/mnm$, the A_{2u} and E_u modes are indicated by grey spheres and maroon pentagons respectively. (b, d) For $Amam$ and $Acaa$, the B_{1u}, B_{2u}, and B_{3u} modes are indicated by green hexagons, black stars, and teal diamonds, respectively. The $Acaa$ space group provides superior overall agreement as indicated by the red label [27]. 91

5.8 Infrared spectrum of $Sr_3Sn_2O_7$ at 21.55 GPa (orange curve) taken in the diamond anvil cell compared with calculated mode positions and intensities for three candidate space groups. Calculated vibrational modes and intensities for $I4/mmm$, $Amam$, and $Acaa$ space groups as compared with the measured spectrum. Symmetries of theoretically predicted modes are given by colored markers. (a) For $I4/mmm$, the E_u and B_u modes are indicated by maroon pentagons and grey spheres respectively. (b-c) For $Amam$ and $Acaa$, the B_{1u}, B_{2u}, and B_{3u} modes are indicated by green hexagons, black stars, and teal diamonds, respectively. The $I4/mmm$ space group provides superior agreement as indicated in red [27]. 93

5.9 Schematic temperature - pressure (T - P) phase diagram of $Sr_3Sn_2O_7$ developed from the critical pressures identified in this work as well as the critical temperatures from literature [82]. These values are indicated by yellow spheres. Error bars are on the order of symbol size. Blurring indicates uncertainly in the position and shape of the phase boundaries - especially in the intermediate temperature and pressure regime [27]. 98

6.1 (a) Traditional (black) and diamond anvil cell (green) infrared spectrum of $Lu_{0.6}Sc_{0.4}FeO_3$ at ambient conditions. Theoretical mode positions and intensities of the end member compounds $LuFeO_3$ and $ScFeO_3$ in the $P6_3cm$ space group are shown with blue squares and red triangles, respectively. The modes are grouped together to show how we assign various predicted excitations to the observed experimental features. Table 6.1 summarizes these assignments in tabular rather than graphical form. (b) Infrared response of $Lu_{0.6}Sc_{0.4}FeO_3$ as a function of pressure. The spectra are off-set for clarity, and the color (green vs. red) indicates the phase. (c) Contour plot of the same data as in panel (b). The critical pressure (P_C) is indicated with a dashed line at 15 GPa [28]. 101

6.2 Group-subgroup relationship along with the corresponding distortion modes between high-symmetry $P6_3/mmc$ and low-symmetry $P6_3cm$ (polar)/$P\bar{3}c1$ (antipolar) structures of hexagonal (Lu/Sc)FeO_3. The K_3 mode distortions are given in terms of a two-component order parameter (Q, Φ) similar to the hexagonal manganites [114] [28]. 103

6.3 Group-subgroup relationship along with the corresponding distortion modes between the high-symmetry $P6_3/mmc$ (non-polar) and the low-symmetry $P6_3cm$ (polar)/$P6_3mc$ (polar)/$P6_3/mcm$ (non-polar) structures of $LuFeO_3$ [28]. 104

6.4 Infrared spectrum of $Lu_{0.6}Sc_{0.4}FeO_3$ in the high pressure phase (at 20 GPa) compared with calculated mode positions, symmetries, and intensities for four candidate high-pressure space groups: (a) $P6_3/mmc$, (b) $P6_3cm$, (c) $P\bar{3}c1$, and (d) $Pbnm$. The calculations are performed for the end-member compound $LuFeO_3$. The match between experiment and theory for the space group $P\bar{3}c1$ is superior and indicated in red [28]. 105

6.5 (a) Close-up view of the low frequency Raman response of $Lu_{0.6}Sc_{0.4}FeO_3$ in the low and high pressure phases. Mode assignments (E_2 and $E_1 + E_2$) are indicated. (b) Frequency vs. pressure for the modes in (a) showing how they soften under pressure, consistent with our calculations. The theoretical data (red, purple and orange spheres connected by black lines) has been rigidly shifted by a few wavenumbers to overlap with the experimental results (blue and teal spheres). (c) Close-up view of the high-frequency Raman response of $Lu_{0.6}Sc_{0.4}FeO_3$ in the low and high pressure phases. (d) Frequency vs. pressure results for the measurements in (c) along with complementary calculations. Theoretical modes are indicated by green, black, blue, and burgundy spheres connected with black lines with mode symmetries indicated in matching colors. Experimental points are given by green, grey and maroon spheres. (e, f) Contour plots summarize the pressure dependence of the low and high frequency Raman scattering response. Intensity is consistent across both plots and is represented by colors ranging from purple to red corresponding to low and high intensity, respectively. Mode assignments are indicated along the bottom, and the critical pressure is indicated by a horizontal dashed line. The vertical dashed line in (e) is a guide to the eye and highlights the mode softening [28]. 108

6.6 Atomic displacements that contribute to the Raman active $E_2(1)$, $E_2(2)$, and $E_1(1)$ modes computed at zero pressure for the ground state $P6_3cm$ structure of $LuFeO_3$ and $ScFeO_3$. The atomic displacement patterns of $Lu_{0.6}Sc_{0.4}FeO_3$ are qualitatively similar, as the primary effect of the mixed Lu/Sc composition is a change in mass [28]. 110

7.1 Overview of chemical and physical heterogeneity in h-$Lu_{0.6}Sc_{0.4}FeO_3$. (a) Crystal structure of the unit cell of h-$Lu_{0.6}Sc_{0.4}FeO_3$. The space group is $P6_3cm$. [52] Teal, purple and red spheres represent Lu/Sc sites, Fe atoms, and O atoms respectively. (b) Atomic force microscopy showing the topography of an area of interest with marks indicating the location of point spectra. (c) Point spectra corresponding to the locations indicated in (b). Curves are labeled and colored to match the different types of spectra observed in the various local composition areas. (d) Piezo-force microscopy of the ferroelectric vortex domains over the same area scanned in (b). Red lines show the positions of line scan 1 (LS1) and line scan 2 (LS2) taken in the 1:1 and 3:4 compositional regions, respectively. 115

7.2 Comparison of far and near-field infrared spectra of h-$Lu_{0.6}Sc_{0.4}FeO_3$. (a) The far field infrared spectrum and (b) near-field amplitude and phase are in good agreement. We can assign the features of the near-field spectrum based upon our complementary lattice dynamics calculations. The theoretical modes are given by blue squares or red triangles for Lu- or Sc-containing modes, respectively. This figure focuses on the frequency range of the near-field response. (c) Three selected mode displacement patterns (at 428, 511 and 557 cm^{-1}, computed for $LuFeO_3$). Displacement patterns calculated for $ScFeO_3$ are the same but with slightly higher frequency. 118

7.3 Near-field infrared response across a ferroelectric domain wall in h-$Lu_{0.6}Sc_{0.4}FeO_3$. (a) Color contour plot presents the near-field infrared response as a function of distance across a ferroelectric domain wall, indicated by the horizontal dashed lines, in the 1:1 Lu:Sc composition region. The image corresponds to line scan 1 in Figure 1d. The spatial resolution is 20×20 nm^2, and the spectrum is sampled every 10 nm along the line scan. The color indicates near-field amplitude as shown by the scale bar. (b) Constant distance curves, extracted from the real space infrared image in panel (a). Cuts are taken before, after, and at the ferroelectric domain wall. Difference spectra ($A(\omega)$ at the wall - $A(\omega)$ away from the wall) are shown at the top of this panel. (c) Fixed frequency cuts of the image in panel (a). These data reveal how the near-field amplitude evolves as a function of distance at the indicated frequencies which correspond to particular vibrational modes. The frequencies are selected to provide contrast at the ferroelectric domain wall in the 1:1 Lu:Sc compositional regime. 120

7.4 Near-field infrared response across a ferroelectric domain wall in h-$Lu_{0.6}Sc_{0.4}FeO_3$. (a) Color contour plot presents the near-field infrared response as a function of distance across a ferreoelectric domain wall, indicated by the horizontal dashed lines, in the 3:4 Lu:Sc composition region. The image corresponds to line scan 2 in Fig. 1(d). The spatial resolution is 20×20 nm^2, and the spectrum is sampled every 10 nm along the line scan. The color indicates near-field amplitude as shown by the scale bar. (b) Constant distance curves, extracted from the real space infrared image in panel (a). Cuts are taken before, after, and at the ferroelectric domain wall. Difference spectra ($A(\omega)$ at the wall - $A(\omega)$ away from the wall) are shown at the top of this panel. (c) Fixed frequency cuts of the image in panel (a). These data reveal how the near-field amplitude evolves as a function of distance at the indicated frequencies which correspond to particular vibrational modes. The frequencies are selected to provide contrast at the ferroelectric domain wall in the 3:4 Lu:Sc compositional region. 121

7.5 Close-up view of the frequency shifts at the ferroelectric domain walls. (a-c) Data are taken within the 1:1 Lu:Sc compositional region and (d-f) are taken from the 3:4 Lu:Sc compositional region. Data are taken at (red curves) and away from (blue curves) the domain wall to emphasize the frequency shifts associated with the wall. 123

Chapter 1

Introduction

Ferroelectrics are fascinating and useful materials that maintain a spontaneous, switchable electrical polarization. This is analogous to ferromagnetism, where the alignment of magnetic moments leads to a net magnetic moment but instead involves the ordering of electric dipoles [1]. These types of arrangements are broadly referred to as ferroic orders, and interestingly, some materials known as multiferroics, exhibit more than one simultaneously. Multiferroics display unique properties that manifest as a result of the interplay between charge, structure, magnetic, and orbital degrees of freedom. This leads to cross-coupling between the ferroic orders, for example, in a magnetoelectric, applying an electric field leads to a magnetization. Of course, there are other ferroic orders, but ferroelectricity is one of the most useful because of its involvement in magnetoelectric coupling. Commonly studied ferroelectrics often exhibit the $AB\mathrm{O}_3$ perovskite structure. The earliest studies of ferroelectrics focused on materials with the traditional displacive and order-disorder mechanisms, while more recent studies have identified complex ferroelectric mechanisms which involve coupling to magnetic spins or require specific geometric distortions of the crystal lattice.

1.1 Traditional polar materials

Polar symmetry is a requirement for pyroelectricity and ferroelectricity. Of the 1651 magnetic space groups, 440 are polar [2]. One of the unifying aspects of these space groups is a lack of

inversion symmetry. These materials exhibit a spontaneous polarization as a consequence of their crystal structure. While both pyroelectrics and ferroelectrics maintain a polarization, the latter is unique in that the direction of the polarization is switchable with an applied electric field. This functionality is the reason ferroelectric materials are desirable for device applications, especially when combined with magnetism for sensing and memory applications.

1.2 Traditional displacive and order-disorder ferroelectric materials

Ferroelectric materials exhibit a spontaneous polarization in response to the application of electric field. These systems display hysteresis meaning that the response of the polarization as a function of electric field is double-valued. A typical example of ferroelectric hysteresis is provided in Fig. 1.1(a). $PbTiO_3$ and $BaTiO_3$ are two of the prototypical ferroelectric materials that undergo the displacive ferroelectric mechanism involving the off-centering of the B-site octahedrally coordinated atom. As such, these first ferroelectrics have been historically utilized in many devices, as early as the 1950's when $BaTiO_3$ was utilized in the development of SONAR technology [3]. Another displacive mechanism takes place in $BiFeO_3$, depicted in Fig. 1.2 and is driven by the spontaneous motion of a lone pair of electrons from Bi formig an electric dipole then causing a shift of the FeO_6 octahedra. Order-disorder driven ferroelectricity in an additional traditional mechanism that frequently involves hydrogen bonding to establish an ordered state with appropriate polar symmetry below the transition temperature [4]. A list of spontaneous polarization values for a few prototype materials that will be discussed is provided in Table 1.1.

1.3 Improper ferroelectric oxides

Unlike traditional ferroelectricity, improper ferroelectrics break inversion symmetry by coupling with another order parameter such as charge ordered states, magnetic order, or a geometric distortion [15]. The mechanism is referred to as improper because unlike the displacive mechanism, the electric polarization is a secondary effect induced by the primary

Table 1.1: Summary of spontaneous polarization values for select ferroelectrics. Values are reported from Refs. [5, 6, 7, 8, 9, 10, 11]

Material	Type	Spontaneous polarization (μC/cm^2)
$PbTiO_3$	Displacive	66
$BaTiO_3$ (tetragonal)	Displacive	28
h-$YMnO_3$	Improper	5.5
$BiFeO_3$ (bulk)	Displacive	6.1
$BiFeO_3$ (thin film)	Displacive	50-60
o-$TbMnO_3$ (ambient)	Improper	≤ 0.1
o-$TbMnO_3$ (at 5 GPa)	Impoper	≈ 1.0
$[(CH_3)_2NH_2]Mn(HCOO)_3$	Order-disorder	1.5
$Ca_3Mn_2O_7$	Hybrid improper	7
$Ca_3Ti_2O_7$	Hybrid improper	15

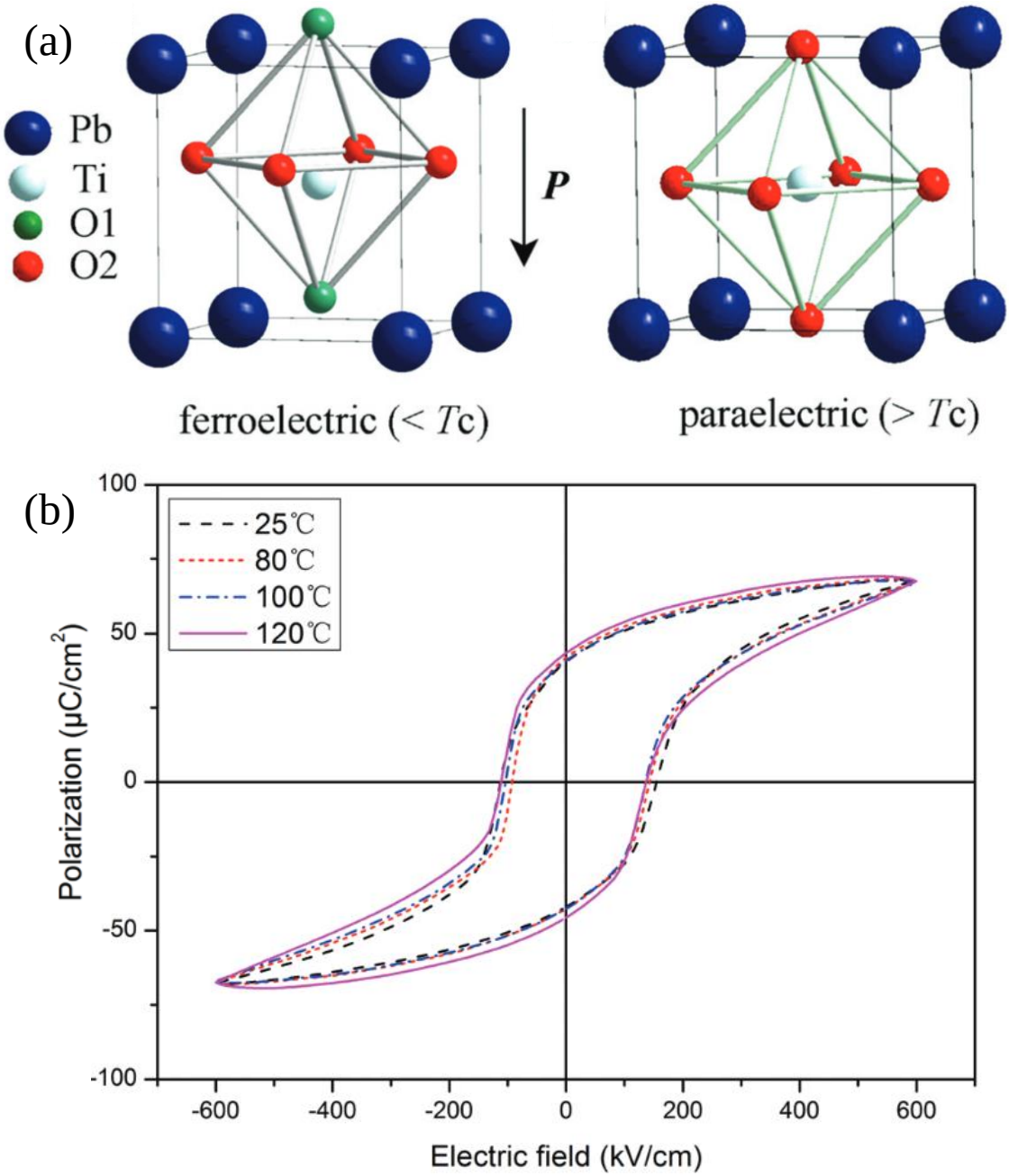

Figure 1.1: The (a) displacive ferroelectric mechanism and its unperturbed paraelectric structure are provided to illustrate how the Ti atom displaces to generate the polarization. The (b) ferroelectric hysteretisis loop obtained from a thin film heterostructure of $PbTiO_3$ and $SmFeO_3$ demonstrates its switchable nature. Reproduced from Refs. [12, 13]

order parameter in the material. As a result of this coupling, multiferroicity states arise when ferroelectricity and magnetism coexist in a single phase. The rare earth mangnatites are one such class of materials which commonly exhibit such behavior and have been extensively studied as a result.

Rare earth manganites of general form RMnO$_3$, often display magnetoelectric coupling that manifest depending on the crystal structure and nature of the improper ferroelectric mechanism. Generally, these materials either adopt an orthorhombic or hexagonal symmetry depending upon the selection of rare earth element. Typically, the resulting structure can be predicted by considering the radius of the rare earth element, with larger atoms generating the orthorhombic structure and smaller atoms yielding the hexagonal structure. Hexagonal (h)-YMnO$_3$ has an improper ferroelectric mechanism involving the tripling of the unit cell, resulting in the trimerization of the MnO$_5$ bipyramids resulting in Y displacements to generate the polarization. This mechanism contrasts with the orthorhombic rare earth manganites where magnetic spins are the driving force and the Mn resides in a octahedral environment [16, 17]. The different structures are provided in Fig. 1.3. Orthorhombic (o)-TbMnO$_3$ attracted attention as an improper ferroelectric with a noncollinear cycloidal spin structure that induces ferroelectricity via a spin-orbit coupling mechanism [15, 18]. A schematic representation of how different spin structures generate the polarization for the improper ferroeoelctric mechanism is provided in Fig. 1.4. An interesting consequence of the magnetic ordering in o-TbMnO$_3$ is a spin-driven enhancement of the spontaneous polarization under pressure. This pressure-induced spin crossover increases the spontaneous polarization from 0.1 to 1.0 μC/cm^2 and changes the collinear spin spiral to an up-up-down-down antiferromagnetically ordered state known as E-AFM [9].

1.4 Hybrid improper ferroelectrics and the Ruddlesden-Popper series

Another logical extension from the perovskite structure is the Ruddlesden-Popper series. This series consists of repeating units of a number, n, of perovskite layers followed by a rock

salt layer and is expressed generally as $A_{n+1}A'_2B_n\mathrm{X}_{3n+1}$, where A,A', and B are cations and X is the anion. [20] Typically, for most systems, n=1-3 or ∞ and for the systems discussed herein, X=O. Similar to the rare earth manganites, the distortions of the octahedra are the key driving force responsible for the broken inversions symmetry required for ferroelectricity. Specfically, the apical oxygens of the $B\mathrm{O}_6$ octahedra are sterically hindered, resulting in rotational and tilting mechanisms to relieve the strain [20].

Ruddlesden-Popper systems with n=2 of the form $A_3B_2\mathrm{O}_7$ have been the subject of many recent studies due to their hybrid improper ferroelectric mechanisms which arise from a trilinear coupling mechanism between three modes. These modes are responsible for generating the ground state $A2_1am$ structure from the $I4/mmm$ parent structure. The three modes are a polar zone-centering mode, an octahedral rotation, and an octahedral tilt, and unlike traditional ferroelectrics, the polar structure of n=2 Ruddlesden-Popper systems is generated solely from these geometric distortions. [21] The ground state structure and schematics of the rotational and tilting modes are provided in Fig. 1.5. These distortions result in displacements of the rock salt layer cation, resulting in a net moment within the unit cell shown in Fig. 1.6. As a result, vibrations of the lattice are intimately linked to the ferroelectric properties of the system. Despite some n=2 systems adopting the appropriate $A2_1am$ ground state crystal structure required for robust ferroelectricity at room temperature, some combinations of A and B atoms generate centrosymmetric symmetries that lack the desired ferroelectric properties. Similar to the manganites, careful consideration of size effects is critical when considering these n=2 Ruddlesden-Popper systems as potential hybrid improper ferroelectrics.

1.5 Domain and domain walls

Multiferroic oxides possess natural heterogeneity in the form of domains and domain walls. This is especially true for hybrid improper ferroelectrics where the distortions of the lattice often also host ferroelastic properties as well. The coupling of these orders gives rise to piezoelectricity where the application of strain modulates the polarization of the system. This effect is a consequence of the intimate connection between the specific order parameters

which generate the non-centrosymmetric structure. The simultaneous orders also yield a structure where the crystal lattice orients in order to minimize strain between adjacent domains. While long anticipated, domain walls have only been studied in detail in the last decade. Ferroelectric domains and the walls between them are only visualized via pizeo-force microscopy that locally applies a voltage into the material to generate a polarization response. For the case of rare earth manganites, stripe and vortex domain patterns develop as a consequence of the magnetoelectric coupling. However, the walls between ferroelastic domains are much easier to visualize as they typically appear as straight lines on the crystal surface in systems such as $Ca_3Ti_2O_7$ as shown in Fig. 1.7. Ferroelectric domains also manifest within the different ferroelastic domains in the sample as meandering lines provided in Fig. 1.7(b,c). Visualization under cross-polarized light provides an additional method to locate ferroelastic walls as separate domains appear as different colors. Moreoever, these ferroelastic walls simultaneously host 90° ferroelectric walls, due to the hybrid improper ferroelectricity in the system. Many studies on domain walls focus on revealing the basic domain patterns and physical properties, like conductivity, leaving the mechanisms of how phonons dissipate strain at domain wall underexplored.

1.6 Pressure-induced phase transitions

Traditionally high pressure studies have been used to understand earth and planetary phenomena. However, studies of multifunctional materials under pressure have revealed remarkable findings such as the high pressure studies of $TbMnO_3$ which revealed an increase in the spontaneous polarization around 5 GPa due to a spin-crossover mechanism [9]. A similar spin-crossover mechanism is responsible for the insulator-metal transition in $BiFeO_3$ above 55 GPa [23]. Analogous to other external tuning parameters, such as temperature and magnetic field, the application of pressure frequently triggers structural phase transitions. In order to fully understand the mechanisms of these transitions, spectroscopy is employed to monitor spectral changes as a function of pressure. Modes in a given material typically harden under pressure. Phase transitions manifest in various forms. Ferroelectric materials are ideal candidates for high pressure studies because of their reliance on specific distortions

to induce ferroelectricity. Because the application of pressure to a material changes the bond lengths and angles as well as the overall symmetry, the key distortions responsible for the ferroelectric properties may be modulated in various ways leading to new, unique properties and states of matter.

1.7 Synchrotron-based spectroscopy

Synchrotron facilities provide the unique advantage of a broadband, high-brightness radiation source. This light greatly improves the signal to noise ratio for all infrared spectroscopic techniques. Moreover, it enables the development of novel spectroscopies that previously had been inaccessible due to a lack of appropriate sources. Synchrotron radiation pulses on the order of picoseconds, which in addition to the brightness and spectral coverage, makes it amenable for use in time-resolved techniques. An overview of the beamlines and spectral coverage of the Advanced Light source is provided in Fig. 1.8. The high-brightness synchrotron source enables high-pressure infrared spectroscopy as it generates the throughput required to transmit through diamonds with small culet sizes capable of reaching the highest pressures. Moreover, incorporation of the synchrotron source into near-field spatially resolved techniques enables broad-band, infrared spectroscopy to be performed on spots on the order of 20×20 nm^2. This spatial resolution can be applied in a variety of ways including imaging of heterogeneous materials.

1.7.1 Spatially resolved techniques using synchrotron radiation

Motivated by previous studies of rare earth manganites examining domain patterns, we reveal the dynamics of domain walls in related transition metal oxides using synchrotron based spectroscopy. The spectral response of domain walls has remained elusive. Synchrotron-based microscopy techniques revealed changes caused by the density of domain walls present in $ErMnO_3$ samples either slow cooled or quenched [25]. Generally, this work revealed that the presence of more domain walls resulted in a higher Born effective charge, and a summary of the results of this study is provided in Fig. 1.9. Unfortunately, this work is unable to reveal the properties of a single wall, and instead, reveals an average response based upon

the density of domain walls. In order to achieve the spatial resolution required to image individual domain walls, techniques that utilize either apertures or sharp tips operating within the near-field limit ($\leq \frac{\lambda}{2\pi}$, where λ is the wavelength of the light) are required. Before the application of synchrotron radiation, only lasers generated light with enough intensity to conduct such measurements, limiting studies to narrow spectral ranges. This limits the capability to study phonons in transition metal oxides, as broadband far infrared sources are limited by their brightness, and lasers do not have enough bandwidth to probe the full set of vibrations present in a given material.

1.8 Improper and hybrid improper ferroelectrics of interest in this work

1.8.1 The n=2 members of the Ruddlesden-Popper series

$Ca_3Mn_2O_7$ and its nonmagnetic analog $Ca_3Ti_2O_7$ became a target of much research after theory predicted how these two n=2 Ruddlesden-Popper systems could establish their polar ground state through the hybrid improper ferroelectric mechanism [21]. While both systems belong to the polar ground state symmetry of $A2_1am$, it was revealed that only the manganite required a polar distortion in addition to the geometric distortions of the lattice, and $Ca_3Ti_2O_7$ navigates to its ground state from the parent $I4/mmm$ structure via a purely geometrically distortive pathway. As a result, $Ca_3Ti_2O_7$ exhibits a much larger polarization than the Mn analog due to stronger coupling between ferroelectricity and the geometric distortions. As such, n=2 members of the Ruddlesden-Popper series have become attractive systems to investigate under pressure for the confirmation of this mechanism is considered a major triumph.

Another result of hybrid improper ferroelectricity is the formation of complex domain patterns. Similar to the hexagonal rare earth manganites which display fascinating vortex patterns due to the coupling between magnetic order and improper ferroelectricity, $Ca_3Ti_2O_7$ exhibits coupled ferroelectric and ferroelastic domains. As a result, the ferroelastic domains, which manifest as twin boundaries also possess ferroelectricity. This offers a distinct

advantage for the understanding of domains and domain walls, as most ferroelectric domain patterns are unable to be observed without specialized techniques like piezo-force microscopy. Twin boundaries, on the other hand, are readily identifiable via simple optical microscopy as they appear as straight lines on the surface. At these interfaces, the crystal lattice is rotated by 90° and are also known as 90° ferroelectric walls. Unlike their 180° counterparts, these walls are much easier to study via spatially resolved techniques as they are visible with modest magnification.

In order to understand the dynamics of domain walls in hybrid improper ferroelectric $Ca_3Ti_2O_7$, we performed near-field infrared spectroscopy at the ferroelastic domain boundaries and compared our findings with models for the evolution of the structural order parameters across the wall. We report large widths for the 90° ferroelastic walls on the order of 100 nm, a finding that contradicts the idea that domain walls are atomically thin [26]. Moreover, experimentally observed phonons at the domain wall and calculations for band gap using the structure of the wall reveal that the wall remains strongly insulating. This finding contrasts with many conducting atomic force microscopy studies which suggest that domain walls are metallic. While we do observe a slight decrease in the band gap, the system remains fully gapped at the domain wall.

$Sr_3Sn_2O_7$ is a hybrid improper ferroelectric system with a set of well-understood temperature-induced phase transitions. It has one of the lowest coercive fields of the n=2 members of the Ruddlesden-Popper series, indicating that its polarization is easily switchable. Starting from the polar $A2_1am$ space group, there is a transition to the paraelectric $Pnab$ phase at 410 K. There are further transitions at 700 and 900 K to the $Acaa$ and $I4/mmm$ phases respectively. Remarkably, pressure drives the system through the same series of phases at room temperature, allowing for a set of structure-property relations to be developed [27]. The ferroelectric to paraelectric transition is accessible with a relatively low pressure of 2 GPa, making it highly attractive as a key component of a switchable device that could be easily manipulated by chemical pressure or strain at room temperature.

1.8.2 The hexagonal rare earth ferrite h-$Lu_{0.6}Sc_{0.4}FeO_3$

In an effort to more strongly couple magnetic and ferroelectric properties in multiferroics to generate materials with higher operating temperatures improper ferroelectrics were developed. Hexagonal rare earth manganites are a class of improper ferroelectrics which received much attention due to the strong coupling between magnetic order and ferroelectricity in h-$YMnO_3$. Similar to their manganite analogues, hexagonal rare earth ferrites such as $BiFeO_3$ also host robust multiferroic properties like, switchable polarization and higher operating temperatures. $LuFeO_3$ is another well understood orthorhombic system that displays linear magnetoelectricity and a spin crossover with applied pressure. Recently, A-site substitution was found to stabilize the hexagonal phase in h-$Lu_{0.6}Sc_{0.4}FeO_3$. The hexagonal structure is only stable with a stoichiometric range between $Lu_{0.6}Sc_{0.4}FeO_3$ and $Lu_{0.4}Sc_{0.6}FeO_3$ and allows for an investigation into nanoscale heterogeneity and how improper mechanism evolves under pressure.

Building upon previous pressure studies on related materials, high pressure infrared spectroscopy reveals a polar to antipolar phase transition in h-(Lu,Sc)FeO_3 at 15 GPa. This structural phase transition from $P6_3mc \rightarrow P\bar{3}c1$ occurs via the modulation of the FeO_5 bipyramidal tilts which modulate the ferroelectricity of the material [28]. Importantly,these findings reveal the distortion pathways responsible for stabilizing the hexagonal phase and for understanding how the competing phases manifest in order to develop more complicated systems.

Ferroelectric walls are traditionally considered nanoscale objects, spanning only a few unit cells from a structural point of view. However, previous work on $Ca_3Ti_2O_7$ suggests that domain walls perturb the phonons at the wall in a way that generates a wide ($\approx$100 nm) response [26] likely to relieve strain at the interface. h-$Lu_{0.6}Sc_{0.4}FeO_3$ provides a unique platform to investigation the infrared response of domain walls as the contrast between domains is strong. Near-field infrared spectroscopy reveals two key features of h-$Lu_{0.6}Sc_{0.4}FeO_3$: (i) the system displays chemical heterogeneity on the scale of a few microns and (ii) the ferroelectric domain walls are approximately 100 nm wide, remain insulating, and display frequency shifts of up to 3.4 cm^{-1}. These findings enable new technologies which

utilize domain walls as functional devices such as racetrack memory [29] and provide insight into the natural heterogeneity that may manifest in other substituted systems.

1.9 Outline of this thesis

This dissertation is organized as follows. Chapter 2 presents a literature survey of multiferroic materials, real-space spectroscopy, high pressure techniques, and project specific details. Chapter 3 provides the fundamentals of spectroscopy and reviews the different instruments and techniques employed in this work as well as their experimental and theoretical backgrounds. The following publications are based upon the work presented in this thesis and are discussed in Chapters 4-6: "Infrared nano-spectroscopy of ferroelastic domain walls in hybrid improper ferroelectric $Ca_3Ti_2O_7$," "Revealing pressure-driven structural transitions in the hybrid improper ferroelectric $Sr_3Sn_2O_7$," and "Pressure-induced phase transition and phonon softening in h-$Lu_{0.6}Sc_{0.4}FeO_3$" [26, 27, 28]. Chapter 7 examines the ferroelectric domain walls in multiferroic h-(Lu,Sc)FeO_3 using real space infrared spectroscopy. Finally, Chapter 8 brings the entirety of the work together in a summary.

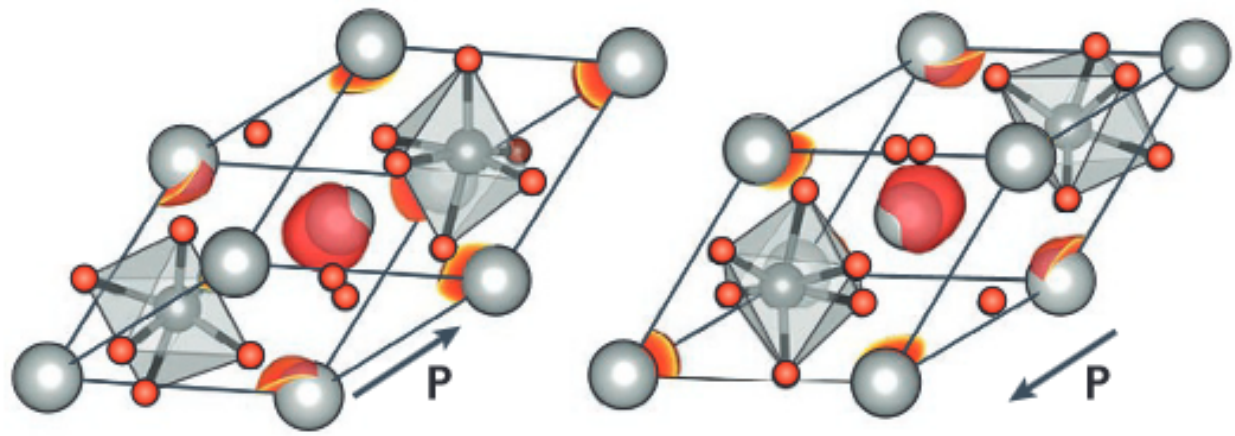

Figure 1.2: A modified version of the classical displacive mechanism takes place in $BiFeO_3$. Instead of being driven by the displacement of the B-site atom, the motion of a lone pair of electrons from Bi induces the polarization. Reproduced from Ref. [14].

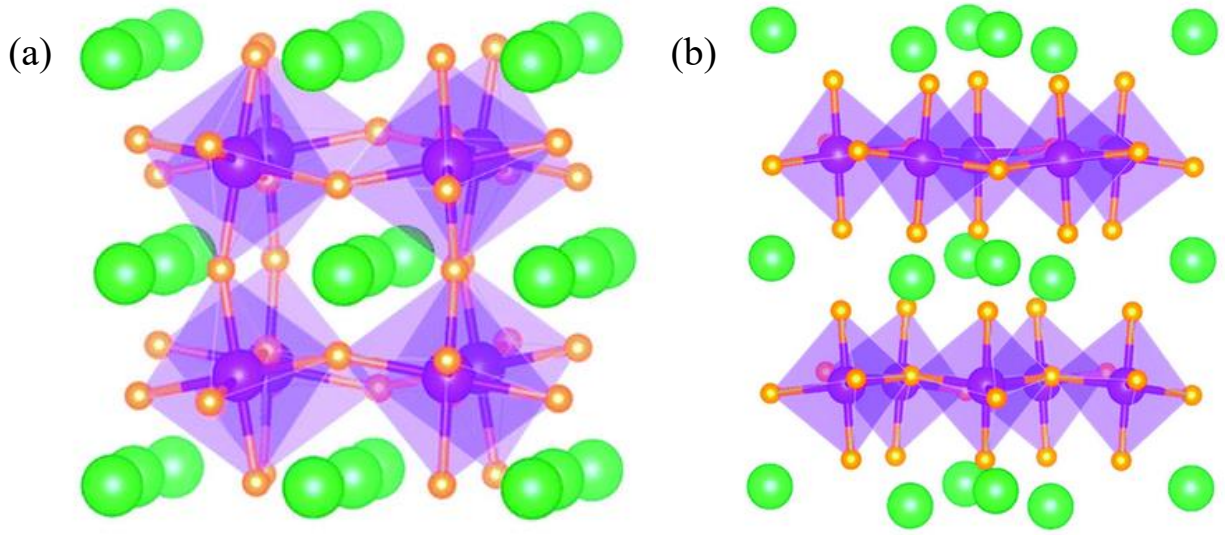

Figure 1.3: The orthorhombic *Pbnm* (a) and hexagonal $P6_3cm$ (b) phases of $R\mathrm{MnO}_3$. The *A*-site atoms are provided as green spheres, with oxygen in orange and manganese in purple. Image reproduced from Ref. [19].

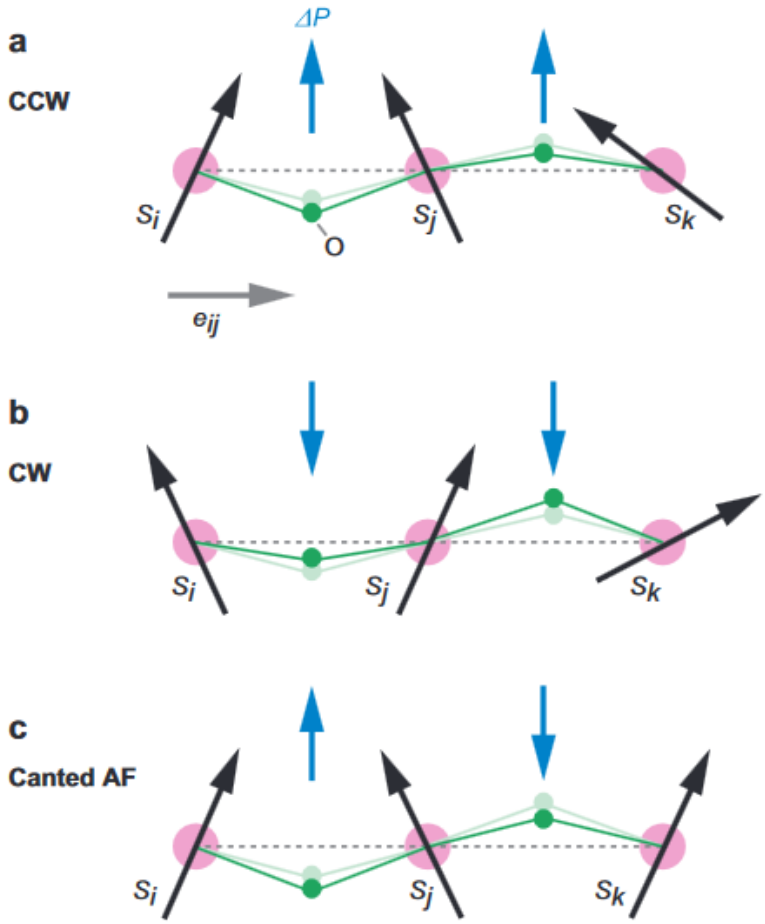

Figure 1.4: (a) Counterclockwise and (b) clockwise cycloidal spin structure which generate the improper ferroelectric polarization. The (c) canted antiferromagnetic magnetic structure is another related magnetic arrangement that generates a spontaneous polarization. Image reproduced from Ref. [18].

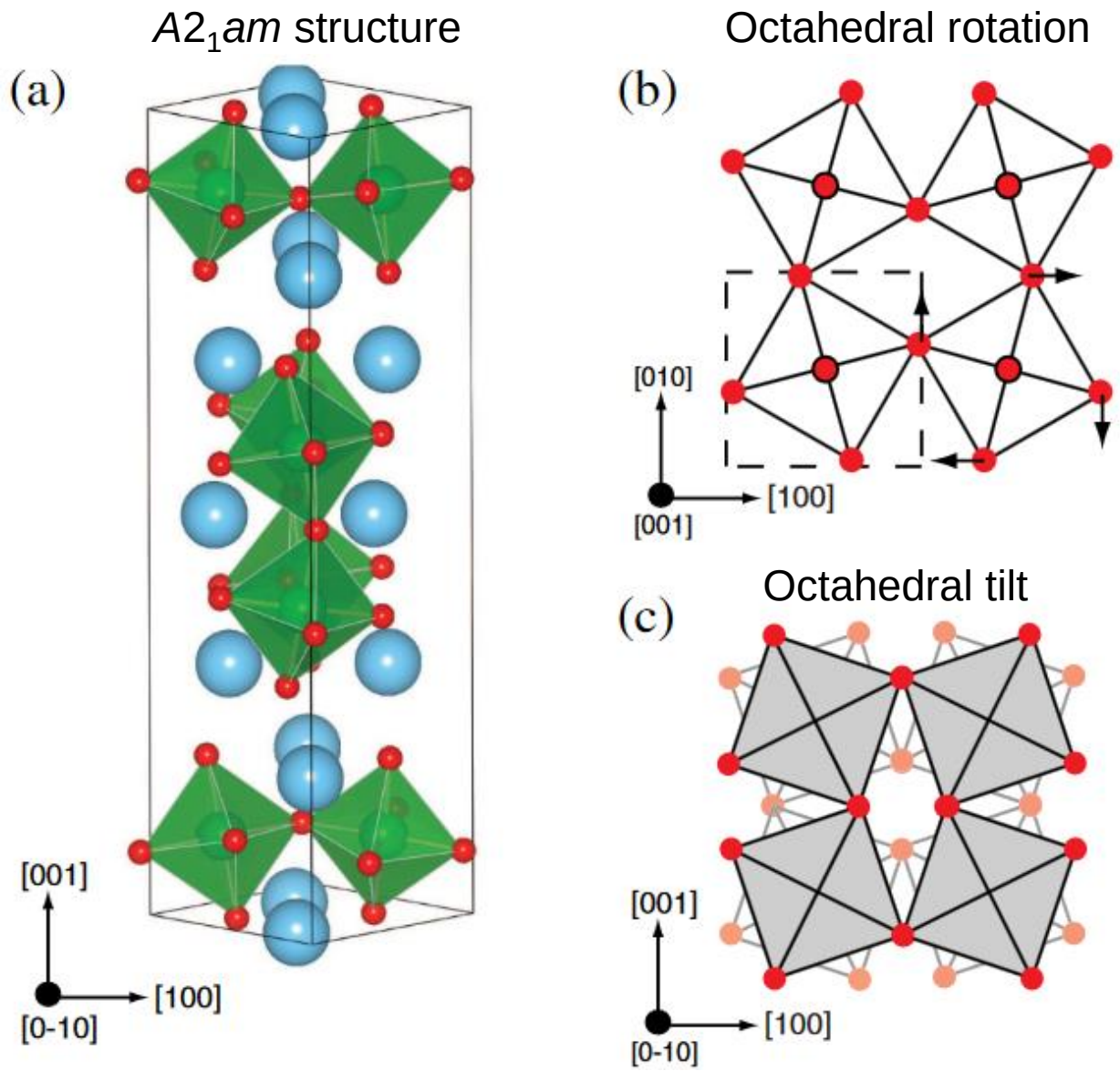

Figure 1.5: The $A2_1am$ ground state structure of $Ca_3Mn_2O_7$ is provided in (a). The shematic of the octahedral rotation (b) and tilt (c) responsible for obtaining the ground state structure from the $I4/mmm$ parent structure are given on the right. Image reproduced from Ref. [21].

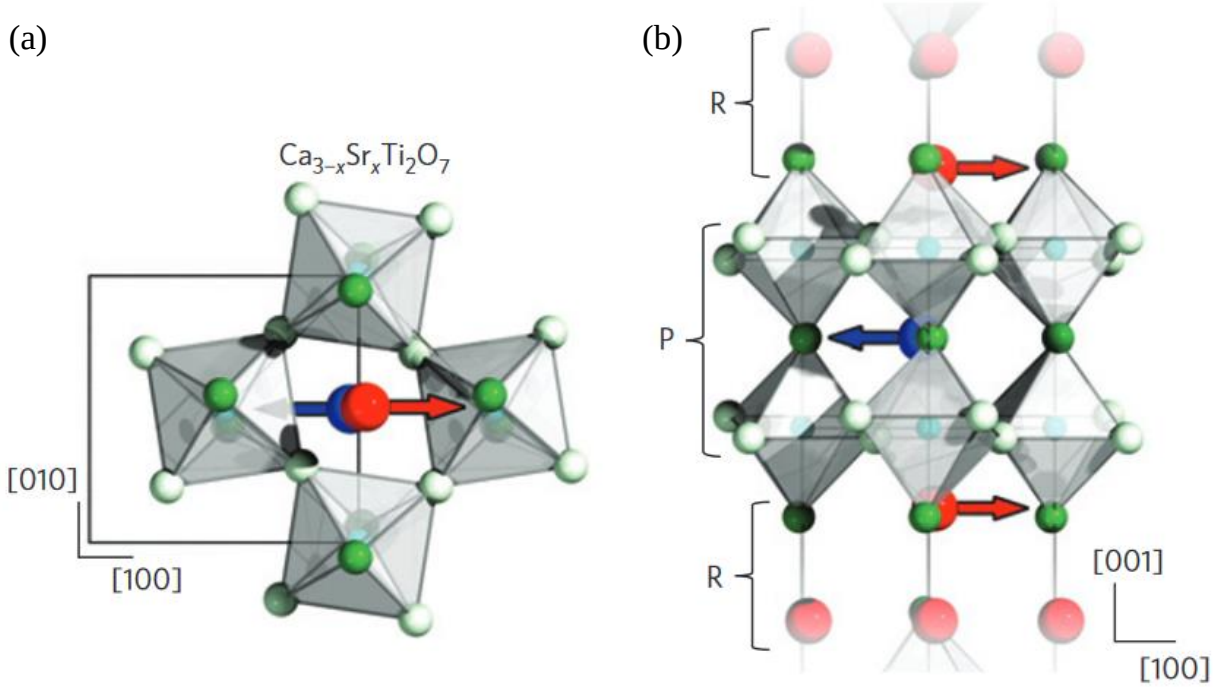

Figure 1.6: (a,b) Two views of the $A2_1am$ ground state structure in $Ca_3Ti_2O_7$ showing how the Ca atoms from the rock salt (R) layer displace oppositely to the Ca in the perovskite (P) layer to generate the net dipole moment. Image reproduced from Ref. [22].

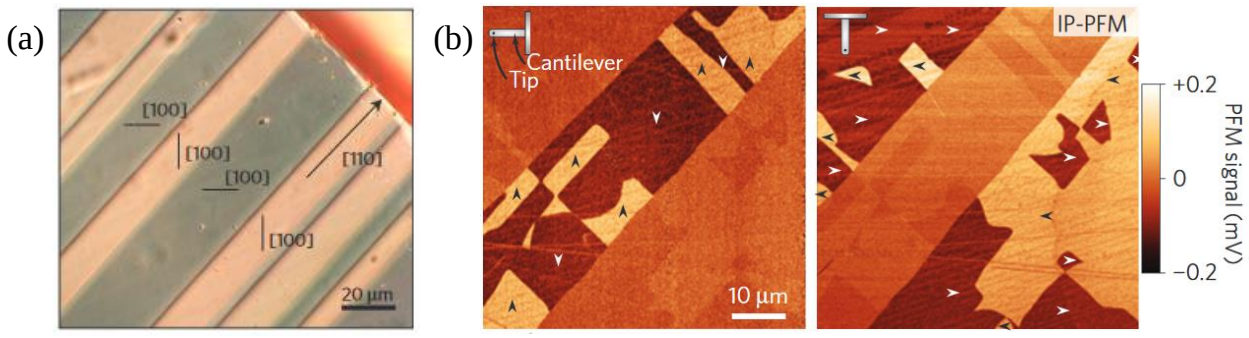

Figure 1.7: (a) Image of ferroelastic twin domains are provided alongside (b) the piezo-force response of ferroelectric and ferroelastic boundaries in $Ca_3Ti_2O_7$. Image reproduced from Ref. [22].

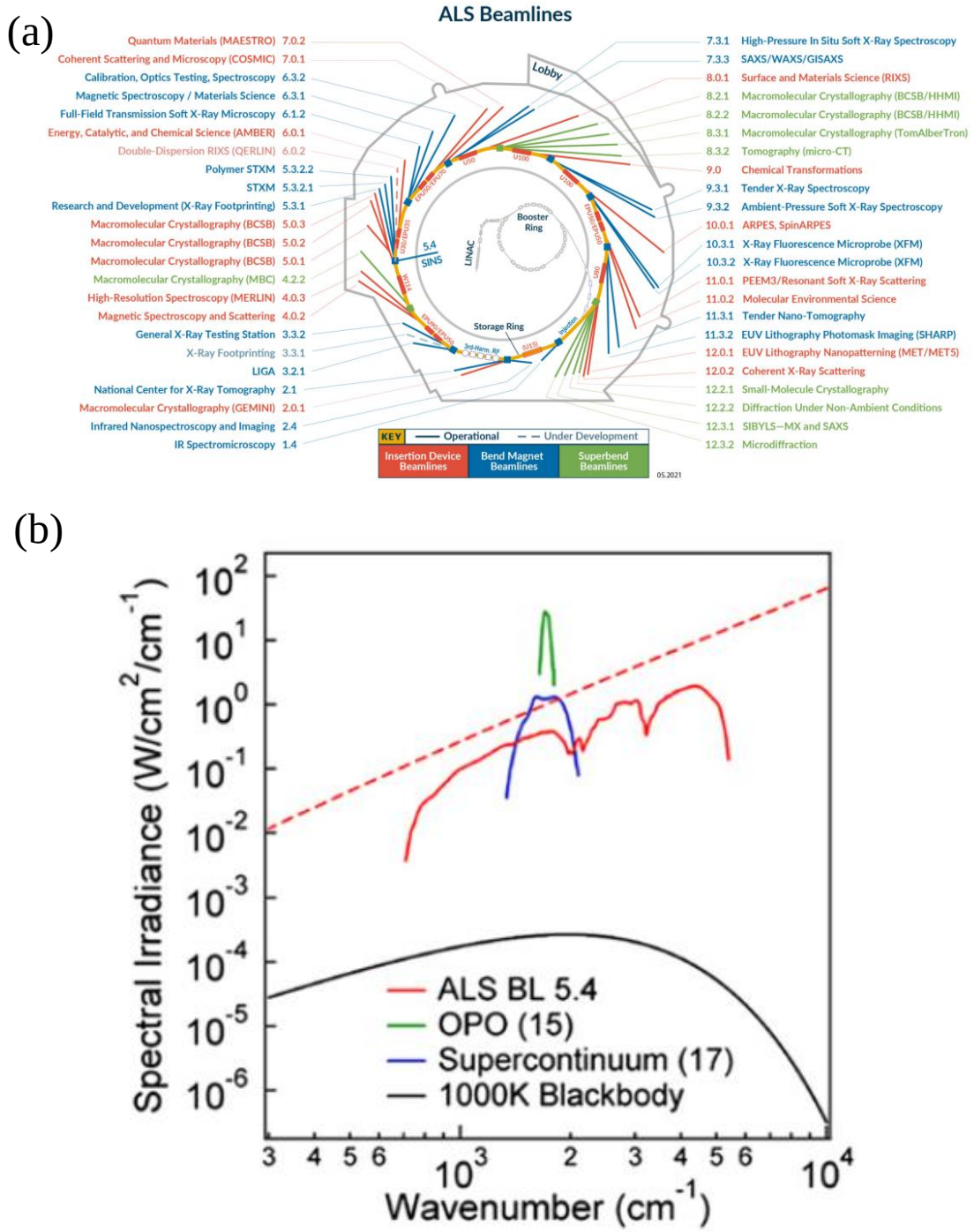

Figure 1.8: (a) Summary of beamlines at the Advanced Light source and (b) a comparison of the infrared spectral coverage of the synchrotron and other commercially available sources. The red dashed line is the theoretical brightness of the synchtrotron and the solid curves are the coverage using different sources. The main feature to note is the brightness of the synchrotron is many orders of magnitude more than a classic blackbody source. Image reproduced from Ref. [24].

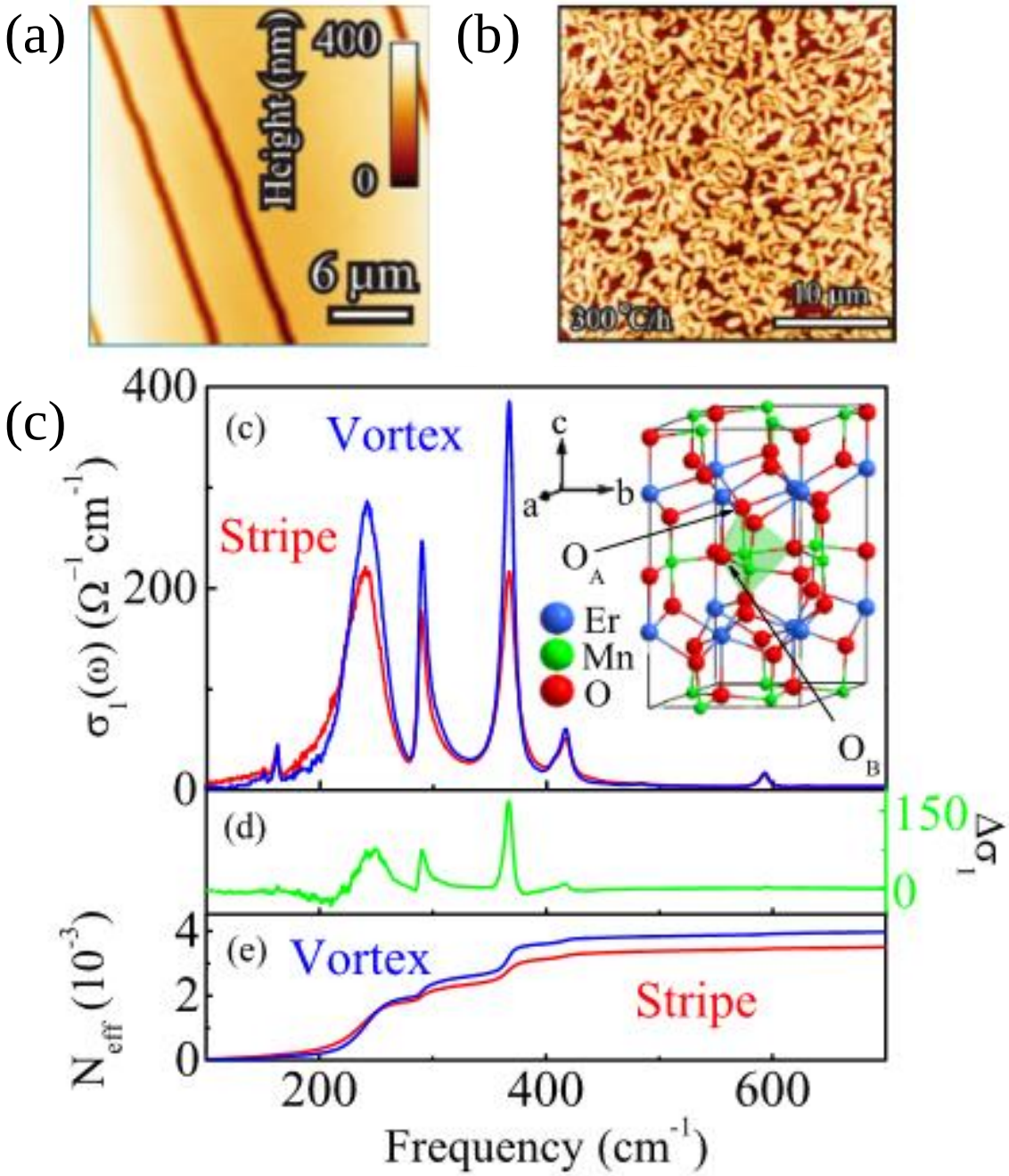

Figure 1.9: Images of (a) stripe and (b) vortex domain patterns and the (c) optical conductivity and Born effective charge calculated from reflectance measurements in $ErMnO_3$. Image reproduced from Ref. [25].

Chapter 2

Literature survey

2.1 Ferroelectric oxides

Ferroic oxides offer an exemplary avenue to explore the coupling between charge, spin, lattice and orbital degrees of freedom. Ferroelectrics, specifically those based upon the perovskite ABO_3 structure, have been rigorously studied due to their prototypical mechanism to break inversion symmetry required for ferroelectricity. The mismatch in size of the A and B cations drives the distortion pathways to generate the spontaneous polarization. When the cations are similar in size, the ideal cubic perovskite $Pm\bar{3}m$ is maintained and the material will not be ferroelectric. Careful consideration of A and B cations is critical to the development of new ferroelectrics with additional properties like magnetism. The competing phases which drive the coupling of the different degrees of freedom in perovskite oxides are responsible for their multifunctionality. By revealing the fundamental mechanisms for how the particular order parameters interact is the key to predicting and identifying new ferroelectics with desirable properties.

In one of the first attempts to understand the structural phases ferroelectrics adopt, Goldschmidt put forth a relation to rationalize the predisposition of a perovskite to undergo a distortion based upon the degree of steric frustration arising from the ionic radii of the A and B cations. The ideal relation is provided in Eqn. 2.1 and is used to determine the

tolerance factor t, defined in Eqn. 2.2 [30].

$$r_A + r_O = \sqrt{2}(r_B + r_O). \tag{2.1}$$

$$t = \frac{r_A + r_O}{\sqrt{2}(r_B + r_O)}. \tag{2.2}$$

To understand what the tolerance factor reveals, we must consider the different values that t may take. When Eqn. 2.1 holds true ($t \approx 1$), the ideal cubic perovskite structure is maintained. For the case of traditional ferroelectrics like $BaTiO_3$ and $PbTiO_3$ $t > 1$. Essentially, the large A atom maintains an oxygen octahedron around the B-site that is too large to bond properly, causing the B atom to displace up or down, generating the polar distortion that breaks inversion symmetry as required for ferroelectricity to develop. In the opposite case, so long as t is not exceptionally small, AO_6 octahedral distortions drive the ferroelectric mechanism instead. For instance, where $t \gg 1$ or $\ll 1$, the material does not adopt the perovskite or related structure. This formalism, while deceptively simple, has shaped how new ferroelectrics are developed and continues to remain relevant for rationalizing the relationship between strain and structure in this broad classification of materials.

Due to the importance of structural distortions in ferroelectrics, external tuning parameters are frequently utilized to unravel how structural modifications influence their fundamental properties. Traditional ferroelectrics frequently have high paraelectric-ferroelectric transition temperatures (e.g. 763 K for $PbTiO_3$ and 391 K for $BaTiO_3$), where the distortion away from the ideal cubic symmetry take place [31, 32]. Pressure offers an alternate route to induce structural phase transitions in materials, and has been demonstrated to modify the displacive ferroelectric mechanism in a variety of materials. $PbTiO_3$ has the highest transition temperature of the displacive ferroelectrics, and it was previously proposed that applying pressure to the system would eliminate or reduce the ferroelectricity. While this prediction is partially correct, it fails to predict what happens at the highest pressures. For $PbTiO_3$, the material adopts a pseudo-cubic phase around 12 GPa, consistent with a decrease in the polarization [32]. More interestingly, at pressures above 20 GPa, the system reverts to its tetragonally distorted $P4mm$ phase and displays an enhancement of ferroelectricity.

This behavior is related to the mixing of the O $2s$ and Ti $3d$ orbitals, and this mechanism is dubbed high-pressure ferroelectricity, to distinguish it from traditional mechanisms [33]. The properties of other displacive ferroelectrics, like $BaTiO_3$ and $SrTiO_3$ are similar, but differ slightly due to the lack of the highly deformable Pb cation [32]. Understanding how ferroelectrics respond to pressure is essential for designing new ferroelectrics that utilize strain to stabilize particular phases with enhanced functionality.

2.2 Development of new ferroelectric oxides

Traditional, displacive ferroelectrics, while displaying large, switchable spontaneous polarizations, require specific symmetry and chemical properties that inhibit other desirable functionalities. While these materials require empty d orbitals for the polar instability, magnetism requires unpaired electron spin to generate a magnetic moment [14]. Despite this fundamental incompatibility, combining these two properties in a single material is essential to develop new technologies such as spin memory devices and magnetic field sensors [34]. While the magnetoelectric effect was first observed in Cr_2O_3 in 1960 [35], the development of single-phase magnetoelectrics remained a significant challenge for many years. The symmetry requirements for the different ferroic orders are provided in Fig. 2.1. The opposing symmetry requirements for ferroelectricity and magnetism are the reason for the difficulty in realizing new magnetoelectric materials, requiring unique design strategies to develop. To further understand the coupling consider the expansion of the free energy as a function of electric and magnetic field provided in Eqn. 2.3 [36].

$$F(\vec{E},\vec{H}) = F_0 - P_i^S E_i - M_i^S H_i - \frac{1}{2}\epsilon_0 \chi_{ij}^e E_i E_j - \frac{1}{2}\mu_0 \chi_{ij}^m H_i H_j - \alpha_{ij} E_i H_j ... \tag{2.3}$$

Looking at the important terms in the equation, the first is the free energy, the second is the static polarization, the third is the static magnetization, and the sixth term represents the magnetoelectric coupling with coefficient α. Taking the derivative of this equation with respect to electric or magnetic field provides the following equations for polarization and

magnetization:

$$P_i = \frac{\partial F}{\partial E_i} = P_i^S + \epsilon_0 \chi_{ij}^e E_j + \alpha_{ij} H_j ... \tag{2.4}$$

$$M_i = \frac{\partial F}{\partial H_i} = M_i^S + \mu_0 \chi_{ij}^m H_j + \alpha_{ij} E_i ... \tag{2.5}$$

Here, P_i^S and M_i^S are the spontaneous polarization and magnetization with ϵ_0 and μ_0 as electric and magnetic susceptibilities. These relations demonstrate how polarization can be induced by magnetic field and magnetization can be induced by electric field. Taking the derivative of the polarization or magnetization allows the linear magnetoelectric coefficient α to be extracted in the following way:

$$\alpha_{ij} \approx (\frac{\partial P_i}{\partial H_j})_{E_i=H_i=0} \approx (\frac{\partial M_i}{\partial E_j})_{E_i=H_i=0}. \tag{2.6}$$

There are higher order magnetoelectric coupling terms, but most research is focused on the linear effect.

2.2.1 Perovskite-derived oxides

Success in developing new magnetoelectric oxides was realized by revisiting the perovskite derived systems. Theoretical models predicted $BiMnO_3$ to be a candidate magnetoelectric with ferroelectric and ferromagnetic properties, unlike Cr_2O_3 which displays antiferromagnetism [40]. Despite successfully demonstrating magnetoelectricity below its T_C of 105 K, substitution and eventual replacement of Mn with Fe led to realization of a room temperature multiferroic $BiFeO_3$. Unlike its Mn analog, the magnetically ordering is antiferromagnetic, but as a single-phase multiferroic, $BiFeO_3$ remains the only room temperature magnetoelectric with a traditional displacive mechanism driving its ferroelectricity [14]. The displacive mechanism is unique in that it is driven by a lone pair of $6s$ electrons from the Bi^{3+} cation that generate an electric dipole, leading to a spontaneous polarization of 6 $\mu C/cm^2$ in the bulk. [8]. The $6s$ lone pair helps to stabilize the distorted structure, driving the ferroelectricity [41]. $BiFeO_3$ also displays unique 71°, 109°, and 180° domain walls as a consequence of its magnetoelectricty. Furthermore, the iron atoms, which

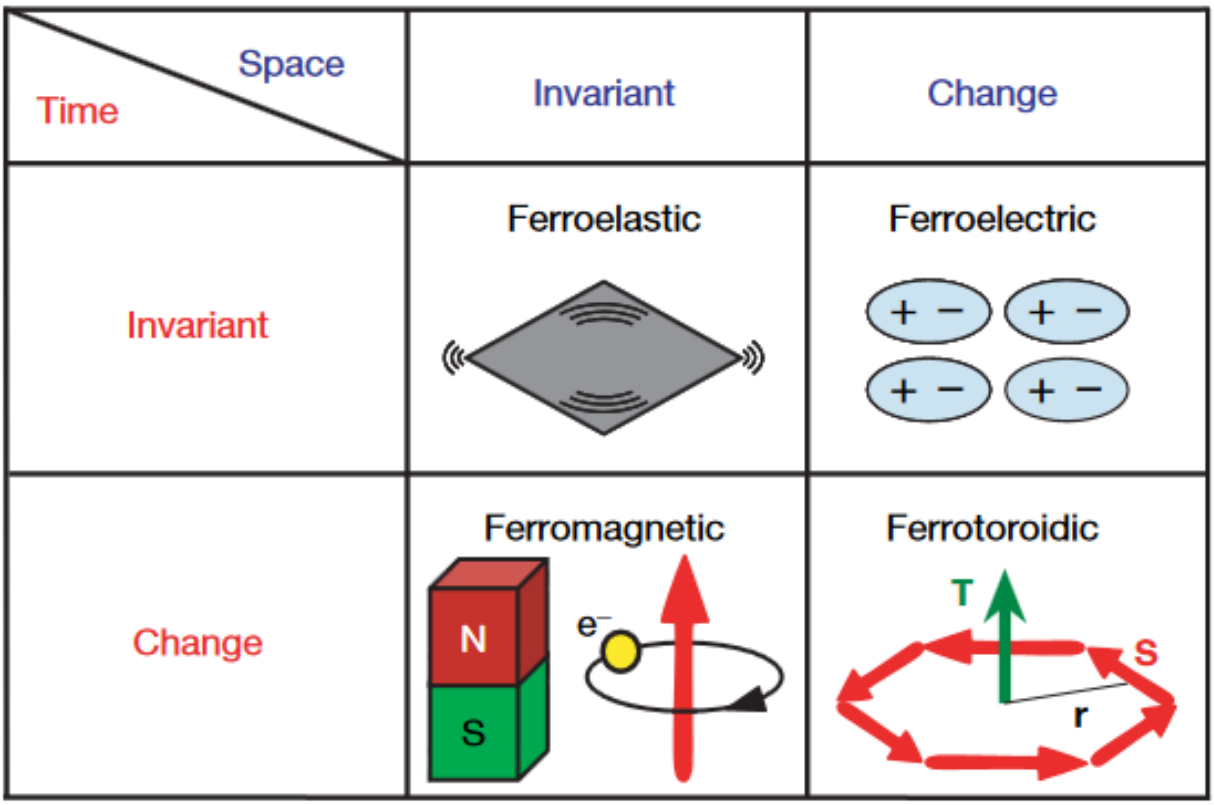

Figure 2.1: Summary of the different symmetry requirements for the different ferroic orders. Image reproduced from Ref. [37].

bring in the magnetic ordering, are also responsible for a spin-crossover that takes place at 50 GPa and results in an insulator-to-metal transition [23].

2.2.2 Improper ferroelectrics

In a similar extension of the perovskite-derived Bi-containing systems, rare earth manganites of the form RMnO$_3$ provide another avenue for exploring magnetoelectricity. As Mn^{3+} is well known to display magnetism as a result of its unpaired electrons, the demonstration of a switchable, spontaneous polarization in TbMnO$_3$ and YMnO$_3$ revitalized the search for new multiferroic oxides. As perovskite-derived ferroelectrics, the manganites display different structures and ferroelectric mechanisms depending on the size of the A-site cation. In an analogous fashion, small A sites generate structures in which geometric distortions induce the ferroelectricity. For the case of a large A cation, the manganites exhibit an improper ferroelectric mechanism where the magnetism from the Mn drives the ferroelectric mechanism. These materials typically couple ferroelectricity and antiferromagnetic orders, generating vortex domain patterns. Moreover, these materials display different crystal structures as a consequence of the deviation from the ideal perovskite structure. The tendency for a given system to adopt an orthorhombic or hexagonal symmetry is summarized in Fig. 2.2(a). Like the traditional ferroelectrics, improper systems navigate a series of different states when probed with various tuning parameters. The magnetic configurations of various RMnO$_3$ systems as a function of temperature have been generalized in the phase diagram provided in Fig. 2.2(b). Generally, for the orthorhombic rare earth manganites below the antiferromagnetic transition temperature, they adopt an incommensurate antiferromagnetic state [38]. Further lowering of the temperature results in two distinct phases depending of the radius of the rare earth element. The systems with the larger radii adopt an A-type antiferromagnetic state, and those with smaller radii enter a locked-in antiferromagnetic state with a large spontaneous polarization. TbMnO$_3$ displays an enormous enhancement of its spontaneous polarization with moderate compression due to the modification of the cycloidal spin state shown in Fig. 2.3 [9]. In the hexagonal YMnO$_3$ the high pressure phases undergo a spin reorientation due to the trigonal bipyramidal MnO$_5$ becoming less distorted,

adopting a nearly triangular lattice leading to magnetic frustration and the realization of a spin-liquid phase at high pressure [42].

2.2.3 Towards more modern layered multiferroic oxides with hybrid improper mechanisms

Combining the ferroelectric perovskite functional unit with layers of another material has led to the discovery of new classes of multifunctional materials. Some early and modern approaches involve combining different perovskite units in a layered heterostructure known as a superlattice [43]. The demonstration of improper ferroelectricity in these engineered structures motivated efforts to develop materials that naturally stack in single crystalline form. The Aurivillius phases are one example of this combined functionality, where Bi_2O_2 slabs and m perovskite-like ($A_{m-1}B_mO_{3m+1}$) layers are alternated [30]. Different values of m and combinations of A and B cations lead to different functionality, but they display robust ferroelectricity and may host magnetism so long as magnetic ions are included in the perovskite-like unit.

Motivated by this layered approach to generating ferroelectricity via an improper mechanism, the Ruddlesden-Popper series attracted interest as an alternative, naturally layered system that could host multiferroicity via an improper mechanism in a single crystal. Comprised of a number, n, of ABO_3 perovskite layers followed by a AO rock salt layer in a periodic stacking pattern where n can take values from 1,2, 3, or ∞, some Ruddlesden-Popper systems were predicted to possess ferroelectric ground states. Other interesting properties can be coupled with the ferroelectricty when magnetic ions are included into the structure, similar to the Aurivillius phases. Furthermore, including Ir in the B-site of new Ruddlesden-Popper systems enables new research into J_{eff}=1/2 and 3/2 states [44]. The ferroelectricity in these materials is unique and for the n=2 members specifically, the mechanism involves the trilinear coupling of three separate lattice distortions [45]. The trilinear coupling relation is expressed in Eqn. 2.7.

$$\mathcal{F} = \alpha Q_{X_{3-}} Q_{X_{2+}} Q_{X_P}. \tag{2.7}$$

$Q_{X_{3-}}$ and $Q_{X_{2+}}$ are the amplitudes of the hybrid improper distortion, and Q_{X_P} is the polar distortion. This relation reveals that reversing the direction of one of the improper distortions reverses the polarization. But if both $Q_{X_{3-}}$ and $Q_{X_{2+}}$ are reversed, the polar distortion remains the same [46]. Unlike the improper ferroelectric distortions in rare earth manganites, the ferroelectric mechanism for the n=2 members of the Ruddlesden-Popper series involves multiple distortions simultaneously to generate the net dipole moment shown in Fig. 1.6. This hybrid improper mechanism leads to the development of ferroelasticity where strain and polarization become coupled.

2.3 Project specific details

2.3.1 Domains and domain walls

The presence of simultaneously ordered states in ferroics leads to the formation of natural heterogeneity in the form of domains and domain walls. As all of the ferroic oxides examined in this dissertation display multiferroicity, understanding the patterns and mechanisms for the formation of domain walls is essential. Despite being nanoscale features, domain walls possess functionalitiy distinct from the bulk that derives from the types of ferroic order present in a system. Simply considering the types of ferroelectric walls, there are charged (positive or negative) and neutral walls in addition to 90° and 180° orientations to yield a total of 6 distinct types provided schematically in Fig. 2.4(a). Ferroelectric walls are considered to be Ising-like, meaning that the polarization decreases in magnitude close to the wall, then switches direction at a given angle (typically 180°), and proceeds to grow in magnitude. For magnetically ordered systems, the spins must rotate across the wall and give rise to Nèel and Bloch walls shown in Fig. 2.4(b). Combining ferroelectric and magnetic ordering complicates this situation further and gives rise to $Z_2 \times Z_3$ vortices in the rare earth manganites, odd angled walls in $BiFeO_3$, and various other patterns depending on the type of ferroic order [47]. The rate of cooling is another factor in determining domain structure, with fast quenched samples displaying much higher densities of walls [25]. Magnetoelectric materials possess domain walls that can be utilized in the development of new memory

architectures. The walls in nanowires are able to act as a bit that can be read by a magnetic tunnel junction [29]. The speed at which the bits are read or encoded is determined by the field that pushes the domain walls through the read or write head at exceptionally high speeds determined by the domain wall velocity [48].

Hybrid improper ferroelectrics display unique domain patterns due to the coexistence of ferroelectricity and ferroelasticity. The coupling arises as a consequence of the hybrid improper mechanism involving the trilinear coupling of octahedral distortions. The domain structure of $Sr_3Sn_2O_7$ is provided in Fig. 2.5. Unlike purely ferrroelectric domains, the ferroelastic domains are visible using an optical microscope with a linear polarizer (Fig. 2.5(a)). The straight lines are orthorhombic twins where there crystal lattice is rotated by 90°. As a result, they interact with the linearly polarized light in a way that makes them optically distinct. Within individual ferroelastic domains, ferroelectric domains are also present. Unfortunately, ferroelectric domains require special techniques like piezo-force microscopy or conducting atomic force microscopy to visualize, making them more challenging to study. Despite this limitation, hybrid improper ferroelectric have strong coupling between their ferroelectric and ferroelastic orders, and the ferroelastic walls are simultaneously 90° ferroelectric walls. This distinction is important because the ferroelectric walls within the ferroelastic domains are 180° walls. An example of piezo-force mapping in $Sr_3Sn_2O_7$ is provided in Fig. 2.5(b,c). The straight lines between twins A and B are the ferroelastic walls, and the domains marked with black or white arrows indicate the polarization direction for individual ferroelectric domains. By applying a localized electric field, individual domains can be moved and switched [22]. These domain patterns are present for the other n=2 Ruddlesden-Popper members and in the case of $Sr_3Sn_2O_7$, the application of electric field is able to detwin the material due to its lower switching barrier. The ability to detwin a material has tremendous potential for device application as it is possible to control the defect density in the material by poling the sample with an electric field or by applying strain [50].

Similar to the related rare earth manganites, h-$Lu_{0.6}Sc_{0.4}FeO_3$ exhibits a $Z_2 \times Z_3$ vortex pattern as a result of the magnetoelectric coupling. Like in $YMnO_3$, the presence of this domain pattern is a consequence of coupling between ferroelectric and antiferromagnetic

domains at room temperature. This system has been investigated using a variety of different near-field scanning techniques including, magnetic force microscopy, microwave impedance microscopy, conducting atomic force microscopy (cAFM), and piezo-force microscopy (PFM), in order to image and understand its domain walls and switchable polarization [51, 52]. A hysteresis loop demonstrating the ferroelectricity in h-$Lu_{0.6}Sc_{0.4}FeO_3$ is given in Fig. 2.6. The microwave and conductance studies reveal a significant increase in the conductivity of the domain wall as compared to the surrounding domain, attributed to an excess of mobile carriers [51]. Additionally, PFM and cAFM images on the same area reveal similar the vortex domain patterns with enhanced conductivity at the interface Fig. 2.7(c,d). Like the related rare earth manganites, the rate of cooling has a strong effect on the density of domain walls 2.7(b). However, due to the A-site substitution, the defect density is even higher for fast cooled h-$Lu_{0.6}Sc_{0.4}FeO_3$ when compared with the manganites. This is similar to how Sr substitution in $Ca_3Ti_2O_7$ creates a much more complex domain pattern with a much higher density of walls [22]. h-$Lu_{0.6}Sc_{0.4}FeO_3$ has a $T_N \approx$440 K and a second transition at 163 K to a canted antiferromagnetic state [53]. A combination of PFM and magnetic force microscopy are employed to investigate the coupling between ferroelectricity and magnetism in the canted antiferromagnetic state. Surprisingly, these states are not strongly coupled, unlike the room temperature phases, and display largely independent domain patterns [52]. Taken together, these findings reveal significantly conducting domain walls with strong magnetoelectric coupling at room temperature and a low temperature magnetic phase that is largely decoupled from the ferroelectricity, providing fundamental groundwork to understand how different phases are coupled in multiferroics.

2.3.2 Pressure-induced phase transitions in the various families of ferroelectrics

Because ferroelectricity is intimately linked to the crystal structure distortions, ferroelectrics are ideal targets to study with high pressure techniques. The application of pressure leads to changes in a material's bond lengths and bond angles frequently resulting in the development of new structural phases. As a result, pressure-induced structural phase transitions often

drive a material into a new phase, distinct from its ferroelectric ground state, such as the tetragonal to cubic transition in $PbTiO_3$ and development of the antipolar *Pbam* phase in $BiFeO_3$ [54, 55]. Structural phase transitions are frequently revealed by x-ray or neutron diffraction, as these techniques directly probe the average atomic positions in the lattice. Spectroscopic techniques, like infrared and Raman, are also used to probe high pressure phases, as they both reveal how particular vibrational modes change as a function of pressure. The development of the phase diagram of $[(CH_3)_2NH_2]Mn(HCOO)_3$ is a prime example of how Raman spectroscopy is used to identify multiple structural phases at various combinations of temperature, pressure and magnetic field to unravel the series of symmetries accessed by different tuning parameters [10]. Remarkably, the polar phase is accessible in this order-disorder ($T_{O/D}$=185 K) ferroelectric at room temperature under modest pressure ≈3 GPa. By analyzing the subgroups of $R\bar{3}c$ (Fig. 2.8(a)) for $[(CH_3)_2NH_2]Mn(HCOO)_3$, the phases accessible with temperature, field and pressure (Fig. 2.8(b)) are predicted and verified by analyzing how modes split or coalesce, indicating a change in structure. In the case of improper and hybrid improper ferroelectrics, the sensitivity of the vibrational properties to these effects is intrinsic due to the coupling of ferroelectricity and specific distortion pathways.

The intimate link between structural distortions and the multiferroic properties of hybrid improper ferroelectrics makes them ideal candidates to investigate under pressure. $Ca_3Mn_{1.9}Ti_{0.1}O_7$ is a prototypical n=2 member of the Ruddlesden-Popper series that is nominally $Ca_3Mn_2O_7$ that uses a small amount of Ti to stabilize the $A2_1am$ ground state structure [56]. This material is investigated with high pressure x-ray and neutron techniques to determine how the tilt and rotational angle are modified as a function of temperature and pressure to identify structural transitions. The pressure dependence of the rotation is relatively invariant, whereas the tilt changes much more dramatically, indicating its importance in stabilizing the high pressure phase above 7 GPa shown in Fig. 2.9. When compared with the pressure dependence of $Ca_3Ti_2O_7$, the role of the partially filled d orbital is revealed to inhibit the rotational distortion, as both the tilt and rotation in $Ca_3Ti_2O_7$ are enhanced with compression [56]. This conclusion motivate future work and design of new

hybrid improper ferroelectrics with different A and B site chemistry to achieve enhancement of particular functionalities.

Similar to the related rare earth manganites, the ferrites display unique ferroic properties due to the competition of different structural and magnetic phases. h-$Lu_{0.6}Sc_{0.4}FeO_3$ is stabilized in its hexagonal phase by the inclusion of Sc atoms. Without Sc, $LuFeO_3$ crystallizes into an orthorhombic symmetry and the Fe is octahedrally coordinated. In an analogy to the rare earth manganites, the hexagonal phase consists of FeO_5 bipyramids. Examples of the orthorhombic and hexagonal phases are provided in Fig. 2.10(a,b). By performing x-ray emission experiments as a function of pressure on o-$LuFeO_3$ and comparing the results with h-$Lu_{0.6}Sc_{0.4}FeO_3$, it is revealed that the hexagonal phase inhibits the pressure-driven spin crossover that takes place at 50 GPa in the orthorhombic system [57]. By considering the crystal field splitting, provided in Fig. 2.10(c), the difference in the pressure-induced behavior of these materials is rationalized as follows. For the octahedral case, the orbitals spit into the well known t_{2g} and e_g levels, whereas, for the bipyramidal case, the d_{z^2} orbital occupies a high energy singly degenerate state, with two doubly degenerate levels below. The high-to-low spin crossover observed for $LuFeO_3$ is driven by increasing the energy spacing between the orbital levels, leading the e_g electrons to pair up with the low energy t_{2g} electrons to form the low-spin state. In the case of the bipyramidal spitting, the filling pattern stabilizes the high spin state, inhibiting this mechanism and no spin crossover is observed up to 70 GPa. It is predicted that there is a possibility of a pressure-induced spin-crossover to an intermediate state when the energy spacing of the d_{z^2} orbital becomes too great, leading to the formation of an intermediate spin state S=3/2, but this has not been observed experimentally, motivating future high-pressure studies to confirm whether this spin-crossover occurs to further understand pressure-induced spin-crossover mechanisms in rare earth ferrites.

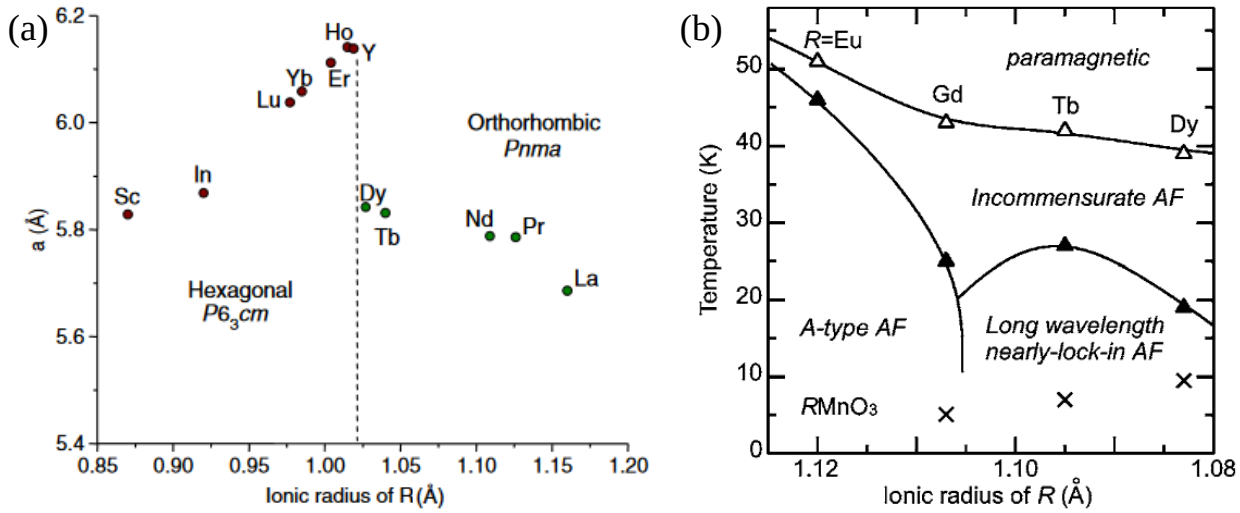

Figure 2.2: (a) Plot of the lattice constant a as a function of A-site ionic radius for selected $R\mathrm{MnO}_3$ systems. (b) Magnetic phase diagram for different rare earth manganites as a function of temperature. Images reproduced from Refs. [38, 39].

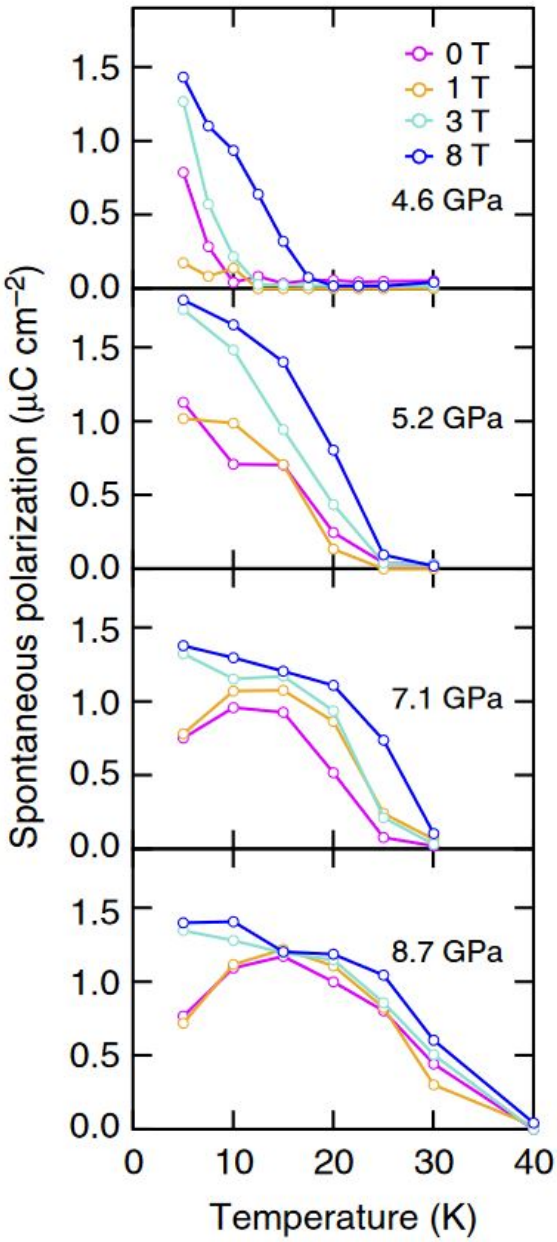

Figure 2.3: The spontaneous polarization of $TbMnO_3$ as a function of temperature at various pressures and magnetic fields shows a distinct enhancement above 5 GPa. Image reproduced from Ref. [9].

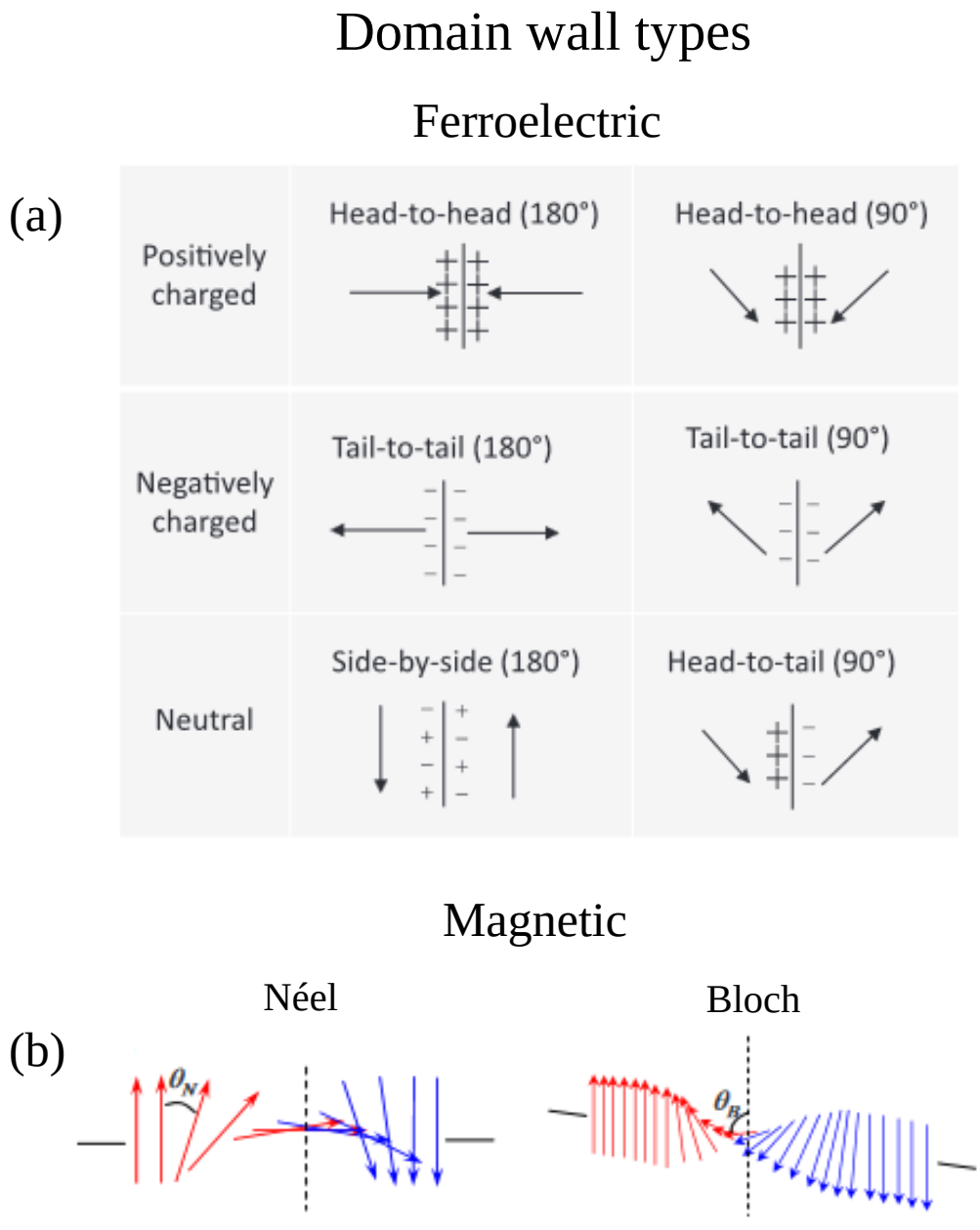

Figure 2.4: The different types of (a) ferroelectric and (b) magnetic domain walls present in materials are given. Image reproduced from Ref. [47, 49].

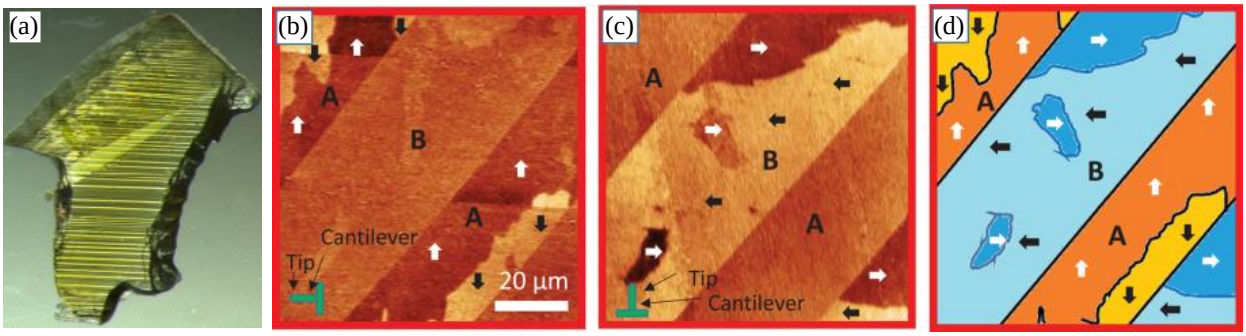

Figure 2.5: The (a) ferroelastic domain walls in $Sr_3Sn_2O_7$ are visualized using polarized transmission optical microscopy. (b,c) Two different orientations of piezo-force microscopy images of ferroelectric walls in $Sr_3Sn_2O_7$ reveal the ferroelectric domains within ferroelastic domains. A (d) composite image of (b,c) shows all combinations of ferroelastic and ferroelectric domains. Images (b-d) reproduced from Ref. [50].

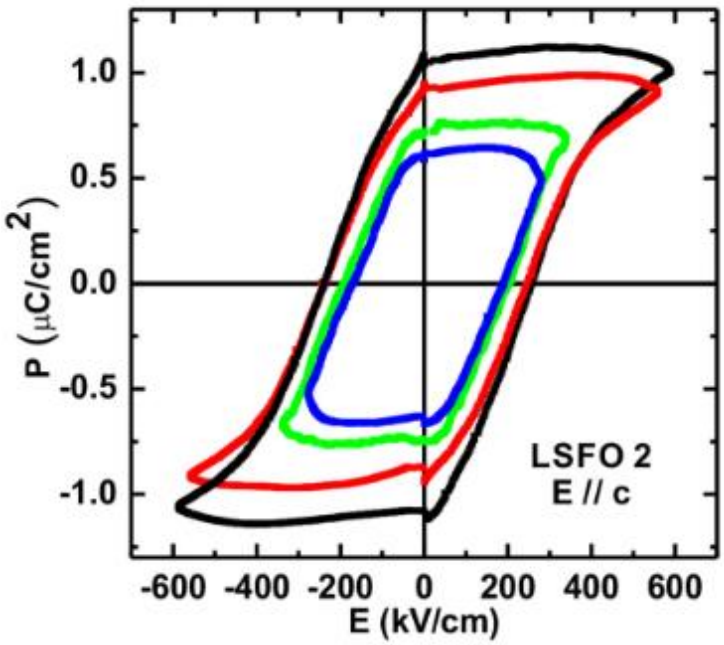

Figure 2.6: The ferroelectric hysteresis loop characterizes the switchability and magnitude of the polarization in h-$Lu_{0.6}Sc_{0.4}FeO_3$. Image reproduced from Ref. [52].

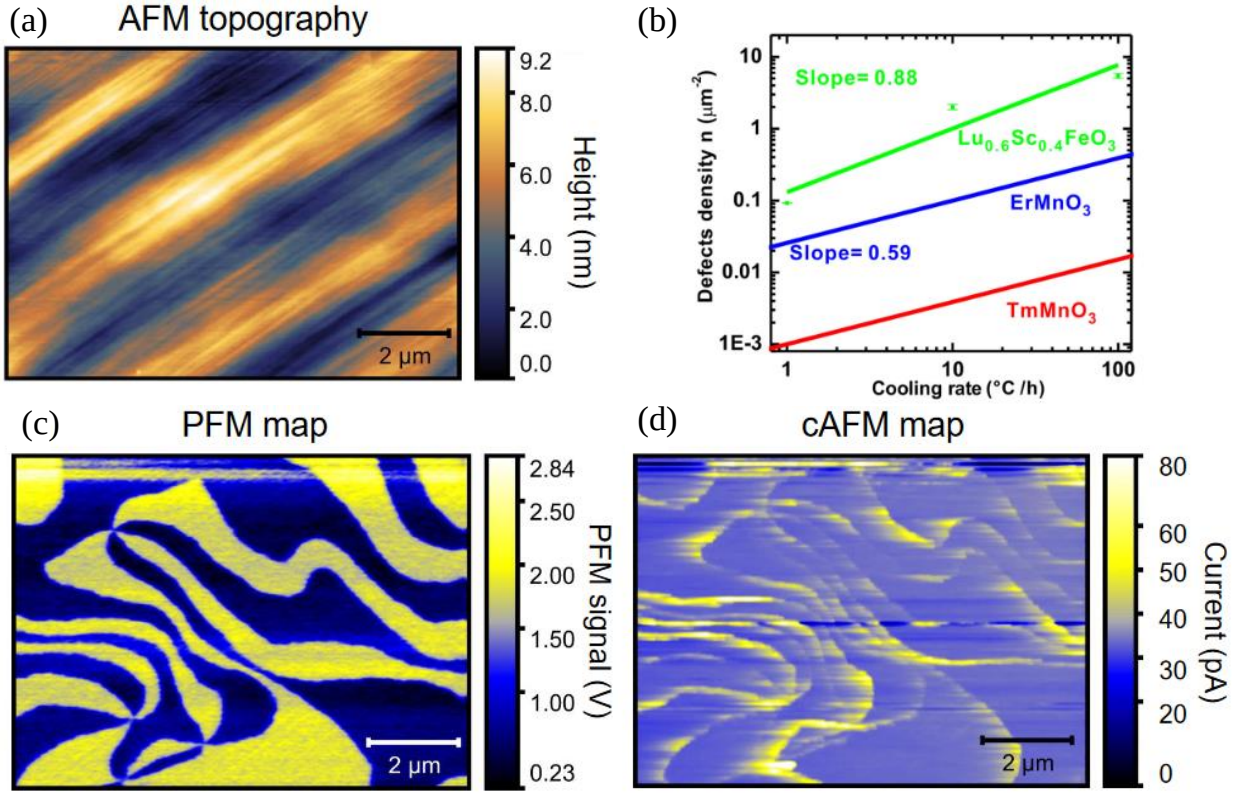

Figure 2.7: (a) AFM topography of h-$Lu_{0.6}Sc_{0.4}FeO_3$ reveals a flat spot suitable for PFM (c) and cAFM (d). (b) Provides the topological defect density as a function of cooling for a few different ferroelectrics. Piezo-force mapping reveals ferroelectric domains with strong contrast. The cAFM map reveals ferroelectric domain walls with significant widths that are more conducting than their surroundings. Image (b) reproduced from Ref. [52].

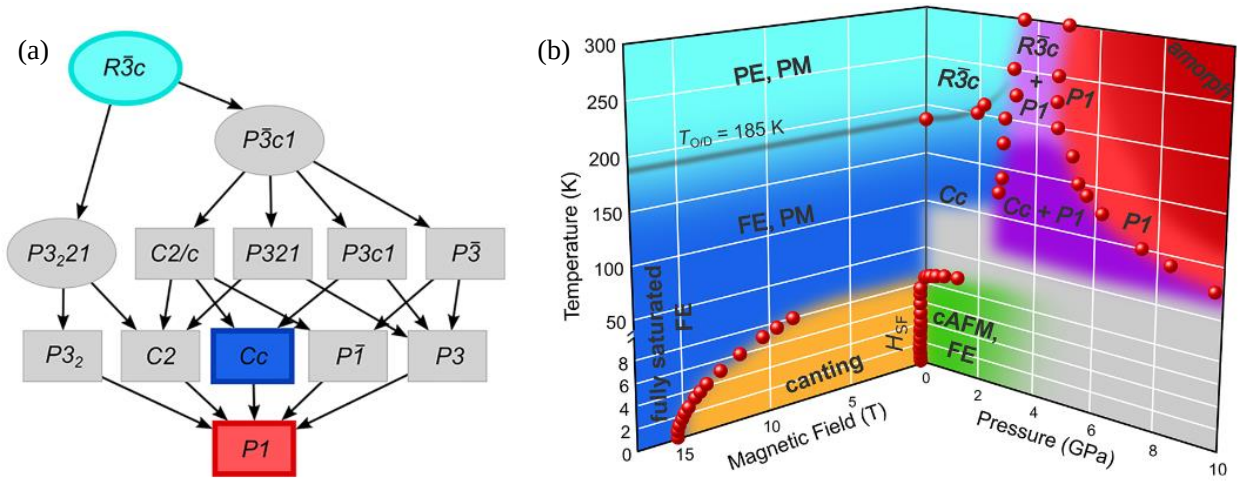

Figure 2.8: (a) Subgroup relations are provided for the $R\bar{3}c$ space group with high-pressure polar phases indicated in blue and red corresponding to the (b) phase diagram. Images reproduced from Ref. [10].

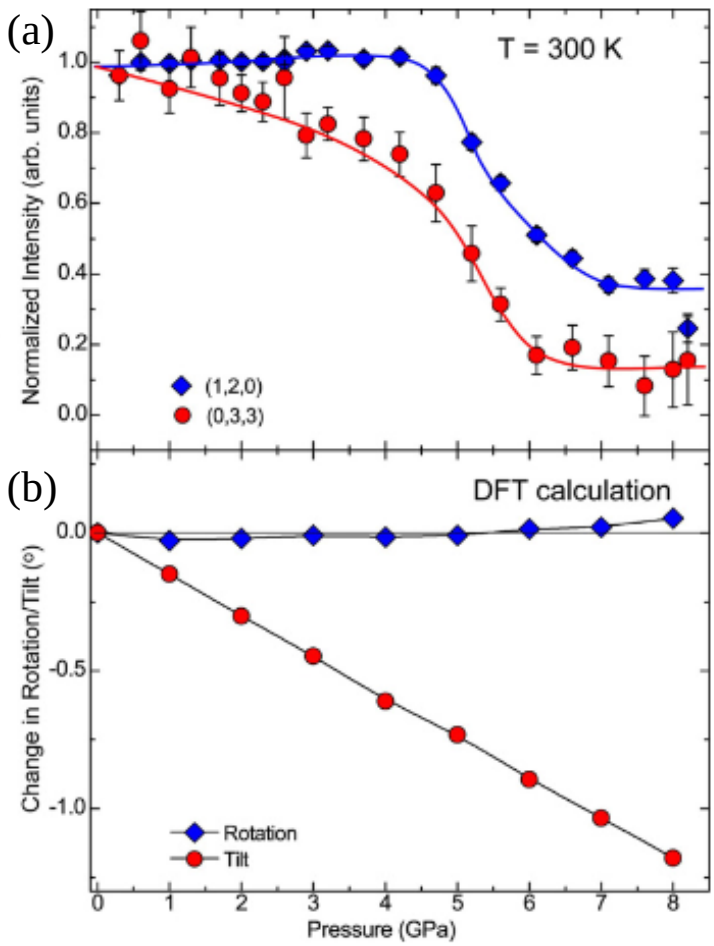

Figure 2.9: (a) Neutron diffraction results of the normalized intensity of the (1,2,0) and (0,3,3) reflections which correspond to the octahedral rotation and tilt distortion for $Ca_3Mn_{1.9}Ti_{0.1}O_7$ reveal a phase transition at 7 GPa. (b) The calculated change in the rotation and tilt angles as a function of pressure is also provided. Image reproduced from Ref. [56].

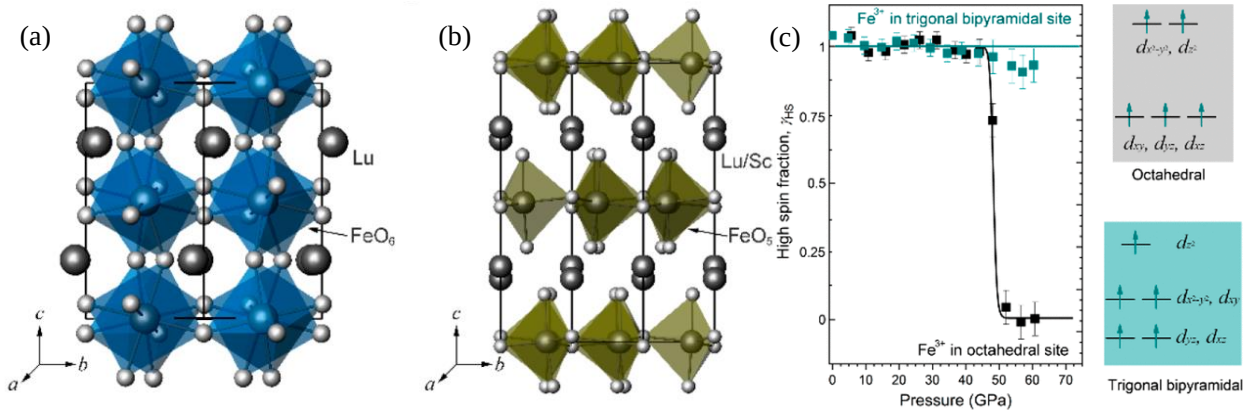

Figure 2.10: The (a) orthorhombic and (b) hexagonal phases of $LuFeO_3$ are provided alongside the (c) pressure dependence of the spin-crossover. Images reproduced from Ref. [57].

Chapter 3

Methods

3.1 Spectroscopic techniques

Spectroscopy is understood as the interaction between light and matter. This description, however, is deceptively simple, as this interplay becomes more complicated when considering how the light or sample of interest can be controlled. In this chapter, we discuss the basics of spectroscopy, its different applications, and more complicated ways in which these powerful techniques are utilized. Two contemporary areas that benefit from the utilization of a synchrotron source, such as near-field and high pressure techniques are discussed in this work.

3.1.1 Beer-Lambert law

To begin the discussion of spectroscopic techniques, we focus on the basics of the Beer-Lambert Law. This formalism allows us to relate absorbance with the ability of a species to attenuate transmitted light. Of course, the relation involves the optical path length and concentration of the material as well, but for practical purposes, these values are either measurable or held constant. The common description of the law is provided in the following equation:

$$A = \epsilon l c, \tag{3.1}$$

where A is the absorbance, ϵ is the molar absorptivity, l is the path length, and c is the concentration. When performing a transmittance experiment, the transmittance (T) is defined as:

$$T = I/I_0, \tag{3.2}$$

where the intensity of the reference beam is I and detected intensity after the sample is I_0. In order to extract the absorptivity coefficient α, we must invoke the following relation:

$$I = I_0 e^{\alpha d}, \tag{3.3}$$

where d is the sample thickness. By combining these previous two equations we relate transmittance directly with α as follows:

$$-\, ln\frac{I}{I_0} = \alpha d. \tag{3.4}$$

We then define $\alpha(\omega)$ as:

$$\alpha(\omega) = -\frac{1}{d} ln(T(\omega)), \tag{3.5}$$

which provides the absorptivity as a function of energy. This quantity has tremendous utility, providing information about optical properties, band gaps and other physical properties. Consequently, $\alpha(\omega)$ is used extensively to explain the behavior of the various materials investigated in this work.

3.1.2 Fourier transform infrared spectroscopy

In order to continue the discussion, we must address the most commonly used type of infrared spectroscopy. Fourier transform infrared (FTIR) spectroscopy provides significant advantages over dispersive techniques. Unlike FTIR, which gives the absorption over a wide frequency window at once, dispersive spectroscopy generates monochromatic light to measure the absorbance at a set frequency. This only captures a portion of a spectra at a given time and requires optical components, such as gratings, to move in order to generate the next wavelength for measurement. This difference is the multiplex advantage of FTIR systems.

Essentially, this allows for the full spectral response to be collected simultaneously. Not only does this save time, but also allows for higher quality data to be generated by taking multiple scans quickly and averaging the results to improve the signal to noise ratio.

The Michelson interferometer is the heart of the FTIR spectrometer and is key for achieving their enhanced performance. A schematic view of the interferometer is provided in Fig. 3.1. Depending on the frequency range of interest, different sources, beam splitters and detectors may be used, but the general operation is the same. The source interacts with the beam splitter which generates two beams. On path 2, the light strikes the fixed mirror and is reflected back to the beam splitter. Simultaneously, the second beam travels on path 1, meets the moving mirror and is also sent back to the beam splitter. The beams then recombine and are sent through the sample to the detector. The computer connected to the instrument then performs the Fourier transform on the raw signal. This signal is generated by the moving mirror which generates either constructive or destructive interference based upon its displacement, x. By carefully maintaining the moving mirror velocity during a given experiment, the following equation provides the relationship between the interferogram function $I(x)$ and the intensity of the source $B(\omega)$ as a function of frequency:

$$I(x) = \frac{1}{2}\int_0^\infty B(\omega) cos 2\pi\omega dx. \tag{3.6}$$

All of the spectral information is encoded into $I(x)$, and it is used to generate the single beam spectrum. By comparing this with a reference spectrum, we generate a typical transmittance spectra by taking a simple ratio of sample to reference. Using the Beer-Lambert Law we then generate $\alpha(\omega)$ which provides information about the low energy excitations in a material.

3.1.3 Raman scattering spectroscopy

Raman spectroscopy is a complimentary technique to infrared spectroscopy that operates over a similar frequency range to probe low energy excitations in a material. Unlike infrared, however, Raman spectroscopy is a scattering technique that uses lasers to excite materials into virtual states that upon relaxation emit photons. The energy of the photons reveals information about the vibrations of the crystal lattice. This emitted energy is on a similar

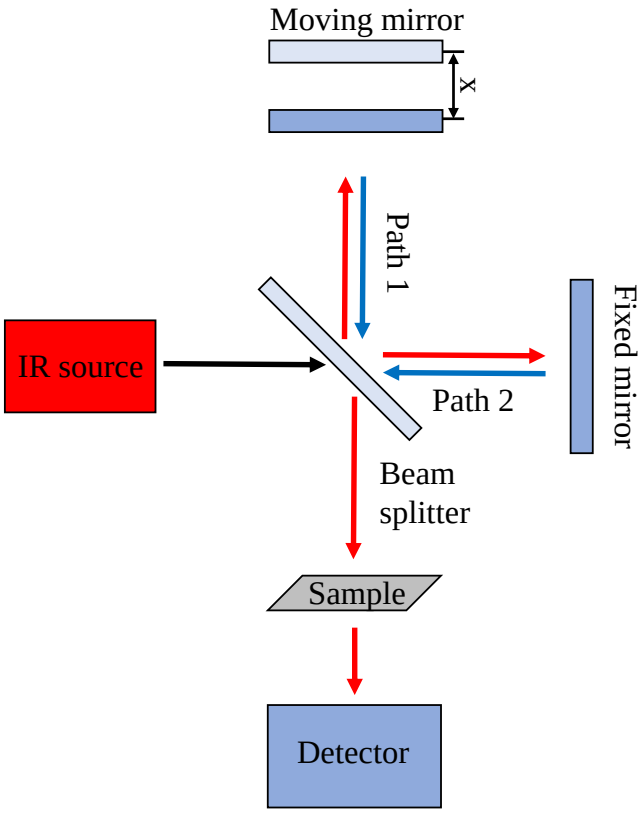

Figure 3.1: Typical schematic view of a Michelson interferometer used in a Fourier transform infrared instrument.

scale as infrared absorption, but instead provides details about symmetric vibrational modes in a system. This is because for a mode to be Raman active, it must experience a change in polarizability. Taken alone, Raman is a useful tool to understand these specific modes, but when combined with infrared techniques, we gain a more complete picture of the excitations present in a given material.

3.1.4 Far and near-field spectroscopy: the diffraction limit & spatial resolution

Because heterogeneity is ubiquitous in solid materials, spatially resolved spectroscopic techniques have been developed in order to probe materials at the micro- and nanoscopic scales. Traditional spectroscopy provides an average response in the area where the beam spot is resolved. Light can be focused into a small area governed by the Abbe diffraction limit provided below:

$$d = \frac{\lambda}{2n\sin\theta} \tag{3.7}$$

with size d, wavelength λ, and numerical aperature $2n\sin\theta$. Because we are using infrared light, the resolved spot size is too large to reveal any changes on the micron scale. Even with a very high numerical aperture of 1.5, 600 cm^{-1} infrared light can only resolve an object of 5.55 μm. While this resolution is appropriate for work at high pressure using a diamond anvil cell, nanoscale objects such as an individual domain wall, remain undetectable apart from an average response. Obviously, using shorter wavelengths increases the spatial resolution. However, at higher energies, we are no longer probing the vibrational properties of the wall, but are instead looking at electronic properties.

One successful method of beating the diffraction limit is to utilize near-field optics. These components operate in the near-field limit, less than one λ away from the sample. One of the simpler ways to perform near-field spectroscopy is to couple an atomic force microscope to a spectrometer. This combination yields a technique known as scattering-type scanning near-field optical spectroscopy. Unfortunately, as the name suggests, these instruments use light in the optical regime and do not typically have enough brightness to operate at lower

frequencies. Despite this limitation, there are options to incorporate lower frequency, high brightness sources in the form of lasers and synchrotron-based light sources.

3.2 Synchrotron-based spectroscopy

Because, specific frequencies of light are needed to perform different spectroscopies, numerous light sources have been developed to cover the entire spectral range. One of the most influential developments in this regard is the synchrotron radiation facility. Building upon prior advances based upon cyclotron physics developed in the 1930s, synchrotrons are large-scale facilities that accelerate electrons in a ring and have them pass through magnetic fields, generating radiation [58]. Specifically, the facility utilizes three rings to achieve its high brightness, broadband light. First, electrons injected into a central ring are collected into bunches and then accelerated to relativistic speeds by a linear accelerator. At this stage, the electrons are brought into the booster ring where they receive even more energy. Finally, the electrons proceed to the storage ring where magnets bend and contain the beam on a set trajectory. Additional magnets called "wigglers" are used to extract the light from the ring. The angle at which this radiation is extracted determines the energy and allows for nearly any frequency of light to be generated at high intensities [59]. This provides substantial gains to many forms of spectroscopy that require high brightness sources at specific energies. Ultraviolet, x-ray, Mössbauer, and infrared techniques benefit greatly from the tunability and brightness provided by synchrotron radiation facilities. Specifically, the infrared light is broadband and extremely high intensity, making it suitable for techniques such as high pressure and near-field infrared techniques that require immense throughput.

3.2.1 High pressure spectroscopy using a diamond anvil cell

The diamond anvil cell is the key component in any high pressure experiment. A general schematic of a diamond anvil cell is provided in Fig. 3.2(a). The primary elements of a diamond anvil cell are the two flawless diamonds mounted with parallel facing culets, a gasket, pressure medium, ruby ball, and sample. Some examples of diamond anvil cells are shown in Fig. 3.2(b) The diamonds used in these cells must be perfect, typically having

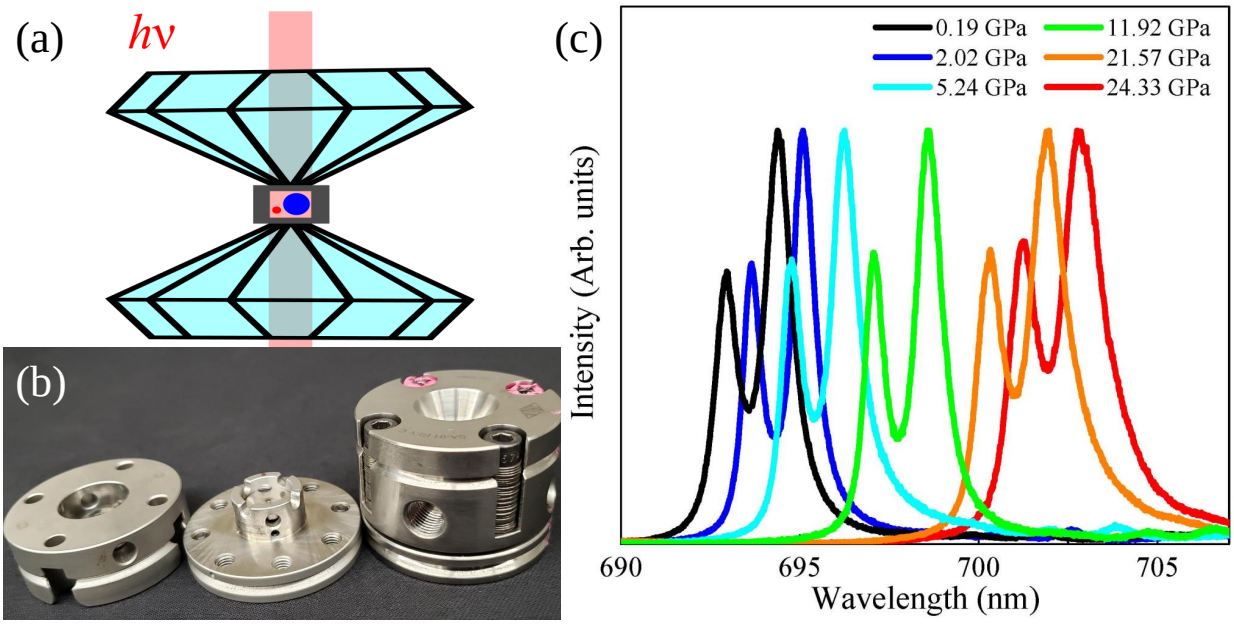

Figure 3.2: (a) Typical schematic view of a diamond anvil cell showing beam passing through the diamonds (red), the ruby for pressure calibration (red circle) and sample (blue oval) loaded into a gasket (grey rectangle) with a pressure transmitting medium. (b) Low profile (left) and standard (right) diamond anvil cells used in this work. (c) Typical ruby fluorescence shows the clear separation of peaks at various pressures.

16 facets for the best dissipation of strain. Additionally, the diamonds are either Type Ia or IIa for Raman and infrared measurements respectively. Type 1a have low fluorescence and throughput in the visible range making them ideal for use in high pressure Raman; whereas, Type IIa are ideal for infrared under pressure as they have higher throughput in the frequency range of interest. Culet size varies depending on the maximum pressure required. Smaller culets (300 μm) generate greater pressures with less control over the step size. When lower pressures with greater control are required, larger culets (500 μm) are used. Selecting an appropriate pressure medium is also important as some do not remain quasi-hydrostatic within selected pressure ranges. The medium (KBr, Argon, Si oil, hydrocarbon grease) is loaded into the gasket. For our measurements, we used stainless steel gaskets with 100-300 μm holes depending on the culet size of the cell. Gaskets are indented to a desired thickness prior to drilling. The thickness of the gasket provides an additional parameter to modulate the pressure. Thin gaskets (30 μm) provide higher maximum pressures, but are more likely to deform and break. Thicker gaskets (80 μm) provide more control at lower pressures, but deform more readily. Pressure is increased by tightening the screws in a step-wise manner on the top of the cell and at higher pressures, the slightest turn generates pressure changes of a few GPa. The selection of pressure media also affects the amount of control and maximum pressure as each have specific pressure ranges where quasi-hydrostaticity is maintained. Additionally, the selection of media must also align with type of measurements being performed. For example, in Raman scattering experiments, it is suitable to use KBr as a pressure transmitting medium; however for the far infrared spectroscopy, hydrocarbon grease is superior. In general, argon provides the greatest flexibility, but it must be cryogenically loaded, which is not always desirable as thermal cycling can unseat the diamonds. Finally, the ruby ball is loaded into the diamond anvil cell in order to monitor the pressure using its well known fluorescence peak position that shifts linearly under compression [60]. A typical ruby fluorescence is shown in Fig. 3.2(c). The clear separation of peaks ensures that the environment in the cell remains quasi-hydrostatic. Careful selection of the various components is of paramount importance to the success of any high pressure experiment.

3.2.2 High pressure infrared spectroscopy

One technique of interest to this work is synchrotron high pressure far infrared spectroscopy. Much like any high pressure experiment, care must be taken in preparing the sample. The synchrotron light source is the key to these measurements. It provides the high brightness far infrared (50-650 cm^{-1}) light required to reach pressures up to 50 GPa. While high pressure Raman spectroscopy is relatively common, high pressure infrared techniques are quite rare due to the high throughput requirement. The high intensity is essential because the diamond culet and gasket hole size must be small (300 μm) in order to achieve large pressures. The sample and hydrocarbon grease (petroleum jelly) or KBr (for far or middle infrared measurements respectively) are loaded into a 100 μm stainless steel gasket of roughly 50 μm thickness. Pressure is monitored by typical ruby fluorescence [60]. By performing this type of measurement, we gain insight into how particular vibrational modes or other excitations respond to pressure. In general, modes harden under compression, but particular modes soften with increasing pressure, indicating the possibility of negative thermal expansion. Complimentary lattice dynamics calculations and symmetry analysis are frequently used to rationalize the changes in modes observed in these high pressure experiments. Thorough analysis of these mode changes is the heart of this technique and reveals aspects of a material's properties that are otherwise inaccessible.

3.2.3 Near-field infrared nanospectroscopy

Near-field infrared nanospectroscopy is a powerful technique to probe materials with infrared light on the sub-micron scale. By combining the high brightness, far infrared light of a synchrotron with the spatial resolution of atomic force microscope assisted near-field scattering techniques, we generate a technique that probes the vibrational response of solids with 20×20 nm^2 spatial resolution. A schematic of setup is provided in Fig. 3.3. Whereas traditional infrared spectroscopy which directly provides $\alpha(\omega)$, near-field techniques generate a signal that is convoluted by interactions with the tip-scattered light. Unlike normal FTIR spectroscopy, the interferogram generated during near-field measurements is asymmetric and requires special processing to obtain the response from the material. The

signal is deconvoluted into amplitude ($A(\omega)$) and phase ($\Phi(\omega)$) components as a function of frequency. These components are related to the real and imaginary components of the complex dielectric function and are most similar to the far-field reflectivity and absorptivity respectively. Samples are selected with flat surfaces with low roughness. This is essential, because the atomic force microscope operates in tapping mode and any large differences in height lead to topographical artifacts and tip crashing in the worst circumstances. Once identified, the sample is mounted to a disk which is held in place by a magnet located in the instrument's stage. The piezoelectric stage offers precise control over the sample position. This control is exceptionally important for work involving the precise positioning of the infrared light onto small regions of interest on crystal surface or nanomaterials. This functionality is precisely how nanoscale objects, such as domain walls, are investigated.

3.3 Project specific details: growth, measurement, and theoretical calculations

3.3.1 Crystal growth

High-quality single crystals of $Ca_3Ti_2O_7$, $Sr_3Sn_2O_7$ and h-$Lu_{0.6}Sc_{0.4}FeO_3$ were grown by Sang-Wook Cheong at Rutgers University. The samples were synthesized by optical floating zone techniques [22, 52, 50]. Each sample was selected due to the presence of domain walls at ambient conditions.

3.3.2 Mapping and locating domain walls

Being able to accurately map and locate objects of interest on a crystal surface is key to any near-field spectroscopic measurement. This process is largely sample dependent. Each sample is unique, and there is variation between samples based upon sample quality. Therefore, it is important to select a high quality single crystal with a large, flat surface for measurements. This ensures that a quality topographical image of the crystal is obtained. Depending on the type of material, different domain patterns are present.

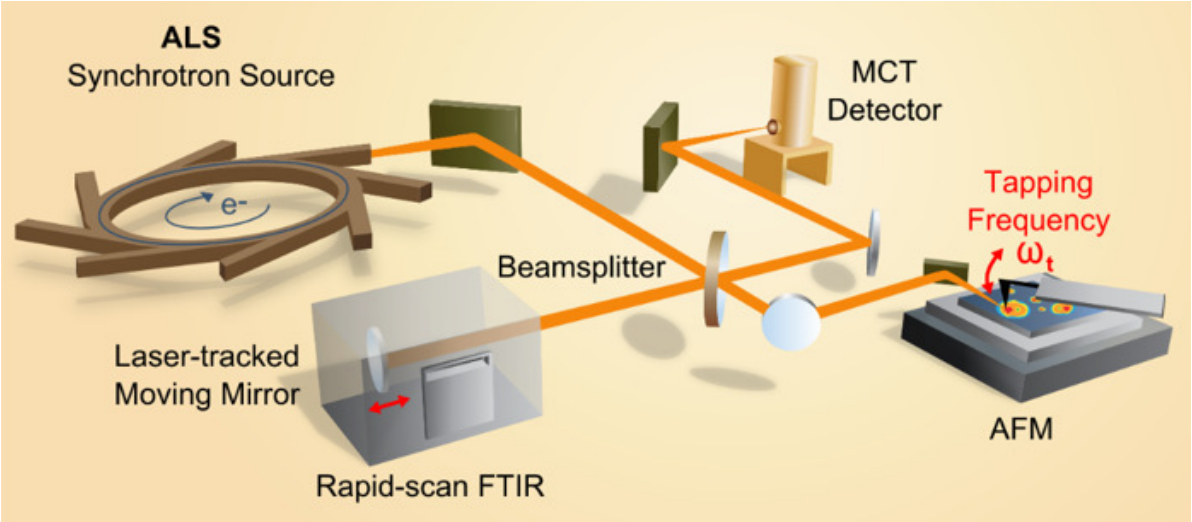

Figure 3.3: A schematic of the near-field infrared nanospectroscopy setup at the Advanced Light Source at Lawrence Berkeley National Lab [24]. The MCT detector is replaced by a far infrared, helium cooled Cu/Ge bolometer detector for low frequency (320-800 cm^{-1}) measurements.

Locating ferroelastic domain walls in $Ca_3Ti_2O_7$

In the case of $Ca_3Ti_2O_7$, ferroelastic walls are easily identifiable by their signature appearance as straight, parallel lines on the crystal surface. These walls are visualized by simple inspection under modest magnification. Additionally, inspection of the crystal under cross-polarizers in transmittance mode reveals the ferroelastic domains that exist between the walls. An example of both images are provided in Fig. 3.4

Locating ferroelectric domain walls in h-$Lu_{0.6}Sc_{0.4}FeO_3$

For h-$Lu_{0.6}Sc_{0.4}FeO_3$, locating the ferroelectric domain walls requires a more in-depth procedure. Unlike the ferroelastic walls in $Ca_3Ti_2O_7$, ferroelectric walls are invisible to the naked eye. Piezo-force microscopy provides the opportunity to image these walls. By applying a voltage through a tip into the sample, this technique reveals domains of opposing polarization directions, creating a map of the ferroelectric domain pattern. Unfortunately, the capability to perform this mapping simultaneously with near-field infrared techniques, has not been realized. As a result, the image of the mapped ferroelectric domains must have a clear signature in order to relocate the same spot. An example of these images is provided in Fig. 3.5. For this sample, residual gold markers are used as way to precisely measure in the same area. Once the area is located and remapped using atomic force microscopy, the ferroelectric domain image is superimposed upon the newly obtained topographical map. By doing so, we can triangulate the exact position of a domain wall of interest for subsequent measurement.

3.3.3 Spectroscopic measurements

Bruker IFS 113v FTIR spectrometer

The Bruker IFS 113v allows for traditional spectroscopic measurements to be performed in the infrared region (21-5000 cm^{-1}). As a Fourier-transform infrared (FTIR) instrument, it provides high sensitivity over a wide frequency range. It features a variety of sources, beamsplitters, and detectors to capture the different energy ranges. A full list of the capabilities of this instrument is summarized in Table 3.1. This instrument operates under

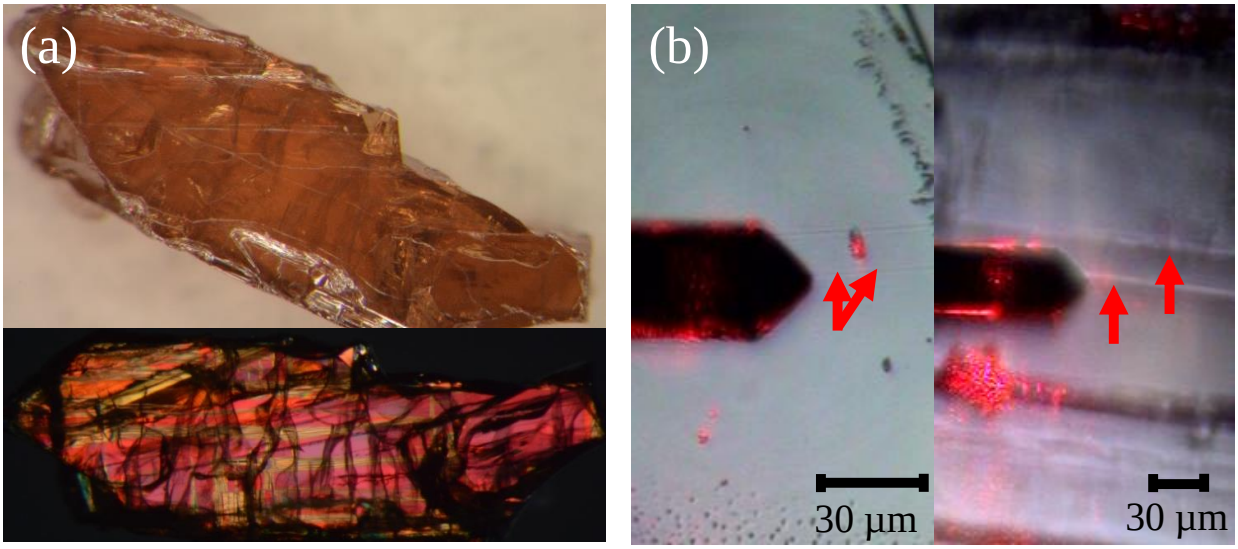

Figure 3.4: (a) Optical (top) and cross-polarized transmittance images of $Ca_3Ti_2O_7$ reveal domain walls a straight, parallel lines. Cross-polarized image clearly shows the different ferroelastic domains in red and gold. (b) Domain walls are imaged using the camera attached to an atomic force microscope prior to measurements.

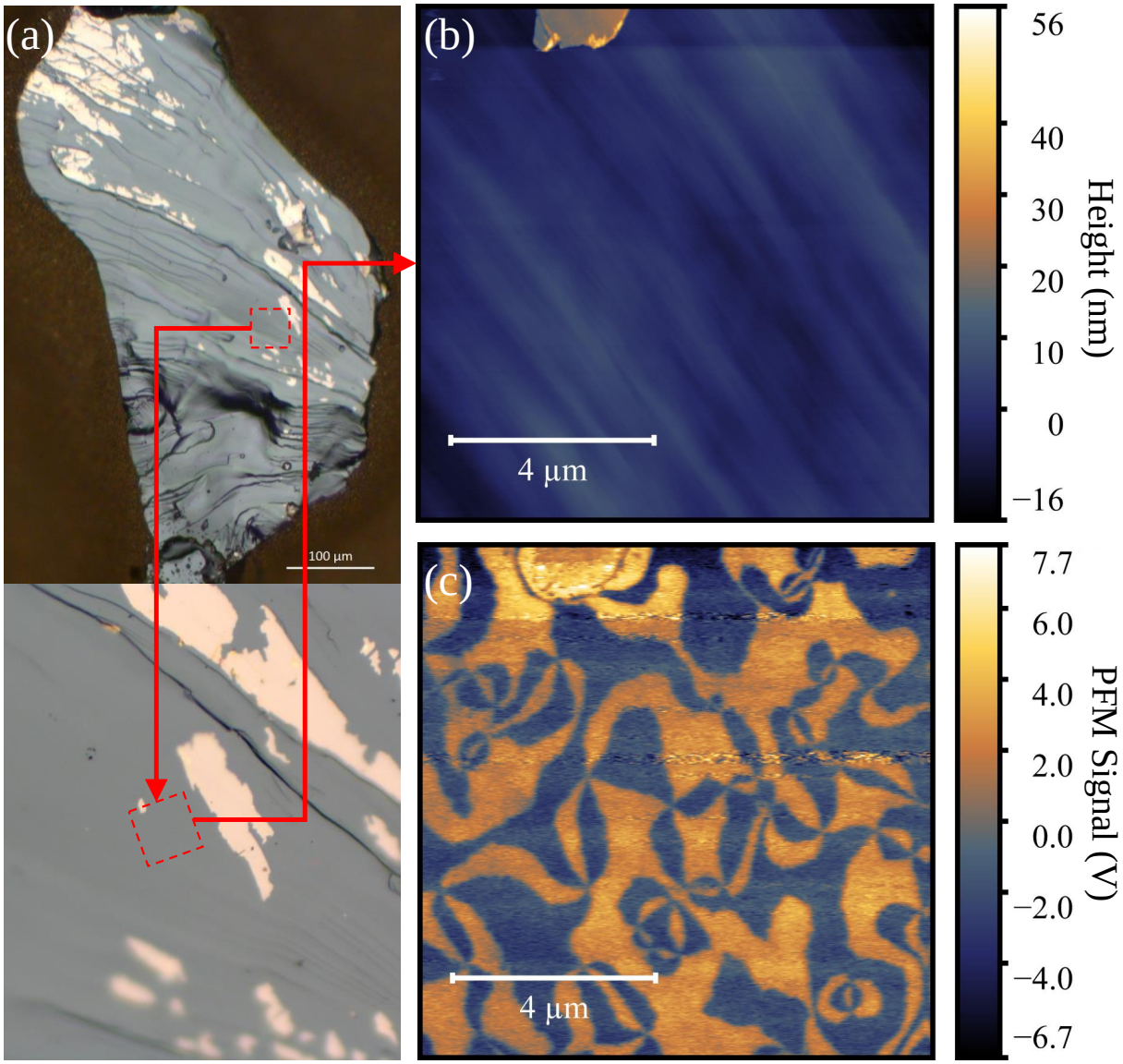

Figure 3.5: (a) Optical images of the crystal surface showing the location of interest. (b) Topographical map of h-$Lu_{0.6}Sc_{0.4}FeO_3$ obtained by atomic force microscopy. (c) Piezo-force microscopy reveals ferroelectric domains in the same region scanned in (b). The same gold marker appears in the top right corner of each image and is used to ensure the proper position is maintained.

vacuum in order to achieve even higher sensitivity by minimizing noise from water vapor. The schematic view of the instrument is provided in Fig. 3.6. The instrument is comprised of four main chambers: the interferometer, source, sample, and detector. The Bruker IFS 113v is capable of working in transmittance and reflectance geometries, allowing us to perform preliminary measurements to prepare for more complex near-field and high pressure studies in similar frequency ranges.

Bruker Equinox 55 FTIR spectrometer with Bruker IR Scope II

This instrument combines a standard infrared spectrometer with the focusing power of a microscope. This yields an instrument that covers a broad spectral range (600-17000 cm^{-1}) that can measure a spot area of 20×20 μm^2 spatial resolution. The optical path of the instrument is given in Fig. 3.7. The broad coverage of this spectrometer is made possible by a combination of various sources, beamsplitters, and detectors summarized in Table 3.2. An additional advantage of this instrument is being able to see exactly where the measurement is taken in real space. This allows for preliminary analysis and mapping of samples that are candidates for near-field spectroscopy.

Raman scattering at National Synchrotron Light Source II

Raman spectroscopy is performed at ambient conditions in a custom instrument with a 532 nm diode-pumped solid state laser and liquid nitrogen charge coupled device detector. The instrument covers the frequency range from 50-4000 cm^{-1}. Power filters are are used to maintain laser power below 1 mW to ensure samples remain unchanged after irradiation. Collection time varies depending on the robustness of the sample. Sensitive samples require extra low laser power which requires longer integration times to produce quality spectra. Multiple accumulations are also taken and averaged to achieve enhanced signal-to-noise ratios. This set-up is optimized for high pressure measurements, but is also functions as a standard Raman instrument with a microscope attachment for microscopy. This capability ensures that the same area is easily found and measured with high accuracy, eliminating the possibility of spectral changes due to spot to spot variation.

Table 3.1: Operational parameters for Bruker IFS 113v

Range (cm^{-1})	Source	Beam splitter	Opt. Filter	Polarizer	Detector
10-50	Hg arc	Mylar 50 μ	Black PE	1	Si bolometer, DTGS
30-120	Hg arc	Mylar 23μ	Black PE	1	Si bolometer, DTGS
50-240	Hg arc	Mylar 12μ	Black PE	1	Si bolometer, DTGS
100-600	Hg arc	Mylar 3.5μ	Black PE	1	Si bolometer, DTGS
450-4000	Globar	KBr	open	2	B-doped Si photocell, DTGS

PE = polyethylene. Polarizer 1 = wire grid on oriented PE, Polarizer 2 = wire grid on AgBr

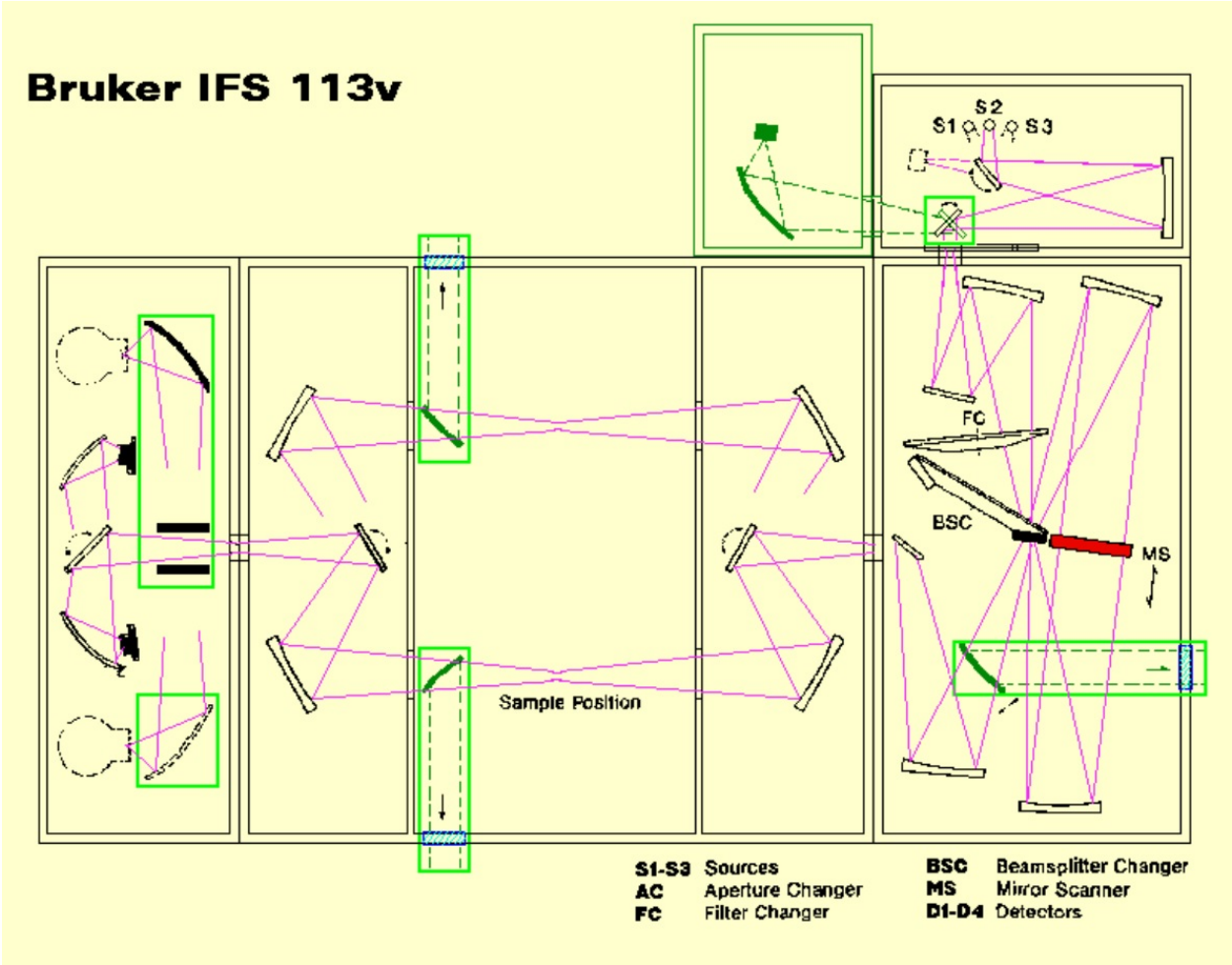

Figure 3.6: Bruker113v IFS spectrometer schematic showing the main components.

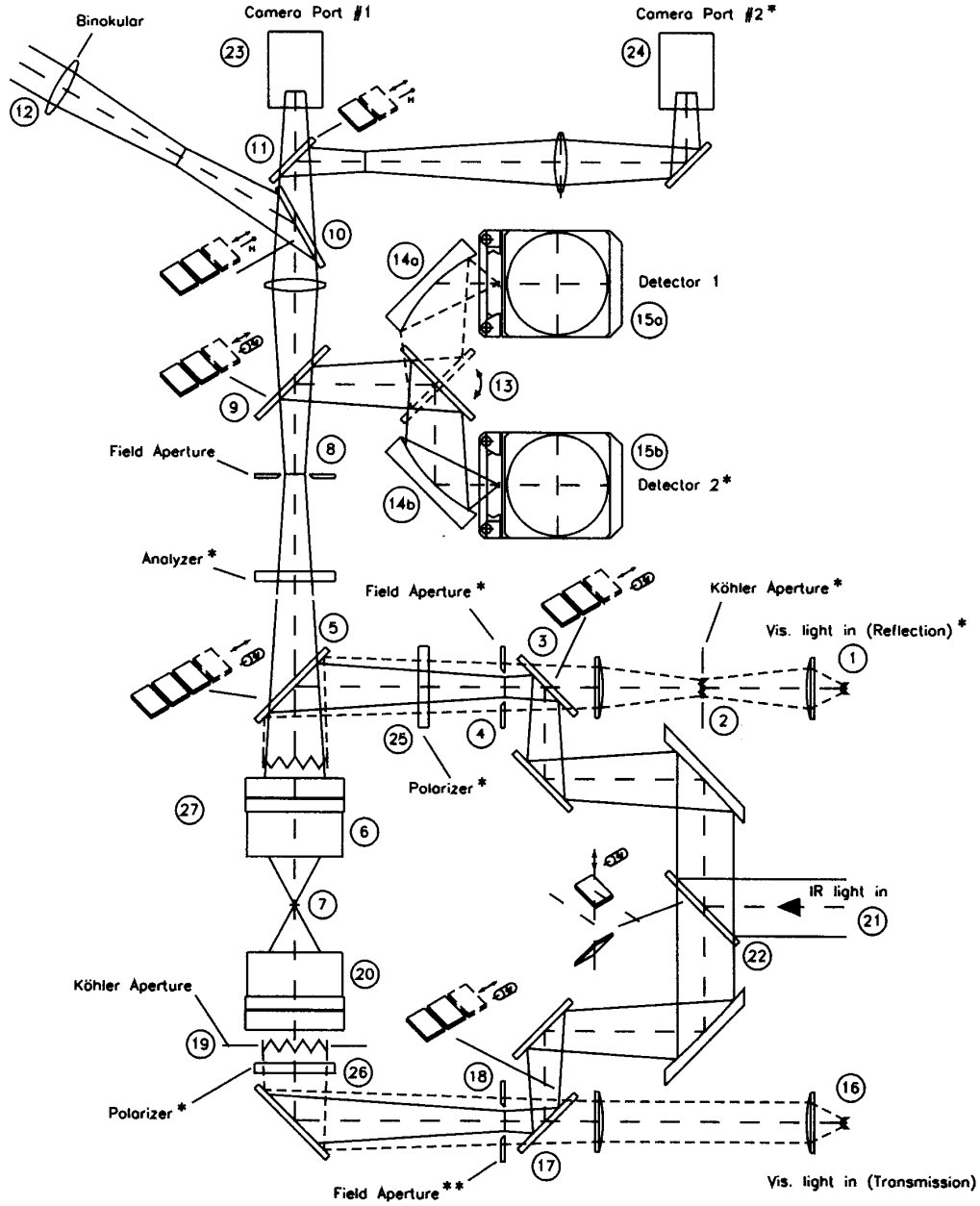

Figure 3.7: Bruker Equinox 55 spectrometer optical path diagram with primary components labeled. 1,16-visible light source; 2,19- visible light aperture; 3,22- motorized switch mirror; 4,18- optional iris or knife edge aperture; 5,9,10,17- beamsplitter changer; 6- Objective lens; 7- Sample; 8- Iris or knife edge aperture which defines the area of sample analyzed; 12- binocular eyepiece; 13- two position detector selection mirror; 14- mirror routing to detector; 15- detector; 20- condenser; 21- IR beam (from spectrometer); 23,24- camera port; 25,26,27- polarizer.

Table 3.2: Operational parameters for infrared microscopy

Range (cm^{-1})	Source	Beamsplitter	Detector
600-7500	Globar	KBr	MCT
4000-12000 (near-infrared polarizer)	Tungsten	Quartz	InSb
9000 -17000 (visible polarizer)	Tungsten	Quartz	Si diode

Synchrotron based near-field infrared spectroscopy

Near-field infrared spectroscopy was performed using the set-ups at beamlines 5.4 and 2.4 at the Advanced Light Source, Lawrence Berkeley National Laboratory. The apparatus is configured as an asymmetric Michelson interferometer, in which one arm consists of an AFM (Bruker Innova or Neaspec neaSNOM) and the other arm is a moving mirror. Synchrotron infrared light is focused and scattered off an AFM tip in close proximity to the sample surface. The scattered light is combined with the reference beam from the moving mirror on a silicon or KRS-5 beamsplitter and detected by a liquid helium-cooled Ge:Cu detector. Scanning the mirror of the reference arm creates an interferogram, which is Fourier-transformed to obtain both amplitude and phase information, which is related to the real and imaginary parts of the optical dielectric function of the material. An example of the instrument used at beamline 5.4 is provided in Fig. 3.8. The incident light is p-polarized with respect to the sample such that the polarization is parallel to the tip axis. This configuration enables the most efficient coupling to the antenna modes of the tip, but there is also a component of polarization in the plane of the sample due to the focusing angle of the off-axis parabolic mirror. However, the strong enhancement of the metal tip localizes and enhances the optical field linearly polarized parallel to the tip axis, such that the technique is most sensitive to phonon and vibrational modes perpendicular to the sample surface. To discriminate the near-field signal from the far-field background signal, the AFM is operated in non-contact (tapping) mode at a typical frequency of 250–300 kHz, and the corresponding detector signal is demodulated at twice the tapping frequency. Measurements were performed with typical free oscillation tip amplitudes in the 80–100-nm range with a setpoint between 70% and 78% of the free-tapping amplitude, such that the engaged tapping amplitude values were in the 55–75 nm range. Routine approach curves with free oscillation tip amplitudes in the 80–100 nm range taken on gold indicate a near-field tip enhancement within <30 nm of the surface with little-to-no second-harmonic signal when the sample is withdrawn further. Different setpoints within the 70–78% range have minimal-to-no effects on the sample amplitude or shape. The setpoint is typically chosen to have the least damping (i.e., closer to 78%) while

still maintaining good AFM feedback and reproducibility between the forward and backward traces. This approach minimizes tip wear as well.

In our work, near-field infrared measurements were carried out at room temperature over a frequency range between 330 and 800 cm^{-1}. The near-field spectra are corrected for the limited transmissivity of the entire set-up by normalizing the power spectrum of the sample to that of a gold reference mirror. Both second- and third-harmonic signals were analyzed. The spatial resolution of this technique is limited by the AFM tip radius, which is typically <25 nm for the tips used (Nanosensor PtSi-NCH). Our line scans employed a step size of 10 or 20 nm for ferroelectric and ferroelastic walls specifically. Multiple line scans across the same domain wall are very similar in character with variances on the order of the noise level. Scans across different domain walls reveal some variations.

High pressure measurements at National Synchrotron Light Source II

Samples were loaded into a symmetric diamond anvil cell along with a pressure medium and an annealed ruby ball. Care was taken to optimize optical density in order to reveal the excitations of interest. KBr or a hydrocarbon-based vacuum grease (petroleum jelly) was used as the pressure medium to assure a quasi-hydrostatic environment for Raman scattering and far infrared experiments, respectively. Diamonds with 300 or 400 μm culet sizes and stainless steel gaskets with 100 μm holes were employed. Ruby fluorescence was used to monitor pressure [60]. Finally, we point out that any high pressure experiment involving a diamond anvil cell is hydrostatic under optimal conditions only to about 6 or 8 GPa. This assumes that there are no problems with the gasket and that a suitable pressure transmitting medium is employed. Above 6 or 8 GPa, there are always non-hydrostatic effects. We therefore take great care loading the cell to avoid sample bridging between diamonds [61]. By monitoring the shape of the ruby fluorescence as well as peak shapes in the sample spectrum (and assuring that line widths do not become too wide), we can confirm that there are no major changes across the pressure range of interest here and the environment remains quasi-hydrostatic.

Synchrotron-based infrared spectroscopy (50-650 cm^{-1}; 4 cm^{-1} resolution; transmittance geometry) and Raman scattering (70 - 3600 cm^{-1}, λ_{excit} = 532 nm; ≈1 mW power; 1200

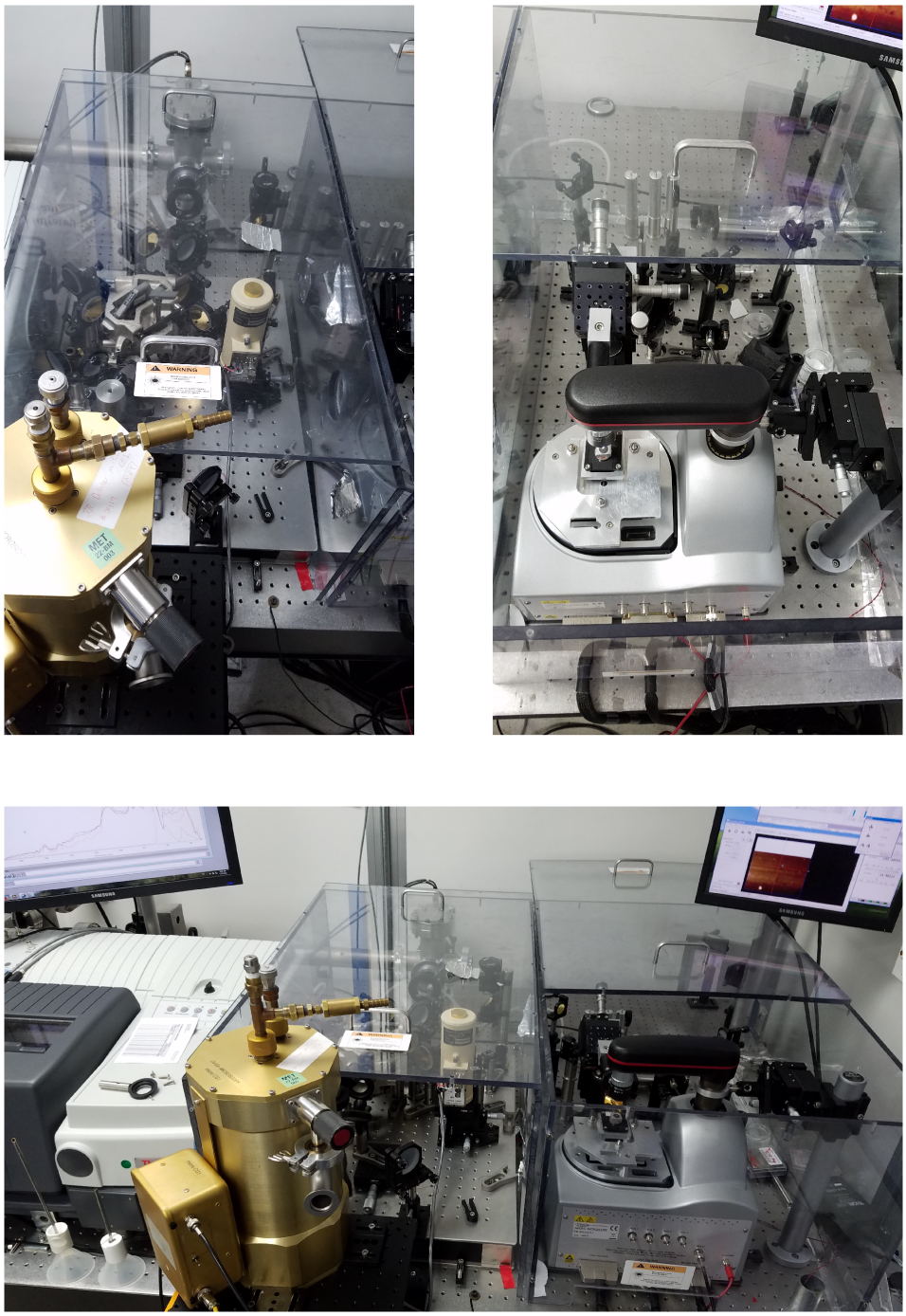

Figure 3.8: Near-field infrared set-up at the Advanced Light Source beamline 5.4.

gr/mm grating, 90 sec integration, averaged two times) were carried out under pressure using the 22-IR-1 beamline at the National Synchrotron Light Source II at Brookhaven National Laboratory. An image of the apparatus used for high pressure infrared measurements is given in Fig. 3.9. All data were collected at room temperature.

3.3.4 Lattice dynamics calculations and group theoretical analysis

Our collaborators performed density functional theory (DFT) [62] calculations using the projector augmented wave (PAW) [63] method as implemented in VASP [64]. We used the PBEsol exchange-correlation functional [65], a 600 eV plane-wave cutoff, and a 2 meV/Å force convergence criterion. The theoretical curves across domain walls in $Ca_3Ti_2O_7$ were obtained by considering a path through the bulk energy surface connecting the two domains and calculating a sequence of bulk structures along that path. This was done using nudged elastic band calculations, allowing the ions to relax at each image along the path—between the $A2_1am$ domain to the midpoint structure $C2mm$ and into the $Bb2_1m$ domain. These calculations allowed us to relate the changes observed experimentally at the domain wall with theoretical models that predict the behavior and energy of the domain wall structure. Additionally, we were able to correlate predicted order parameter trends with collected near-field infrared data across a domain wall.

We performed group theoretic analysis with the aid of ISOTROPY and the Bilbao Crystallographic Server and visualized crystal structures using VESTA [66]. This analysis reveals a number of aspects about a material. We predict the number and activity of the vibrational modes in a given sample. This allows us to assign symmetries to observed modes based upon intensity, activity and clustering patterns. Moreover, when pressure is applied to a system, structural phase transitions occur. New potential phases are predicted by utilizing the group-subgroup relationships between crystallographic space groups. Vibrational modes are calculated for given structures which are then compared to experimental results. This analysis, combined with enthalpy calculations allowed us to assign specific space groups to observed high pressure phases.

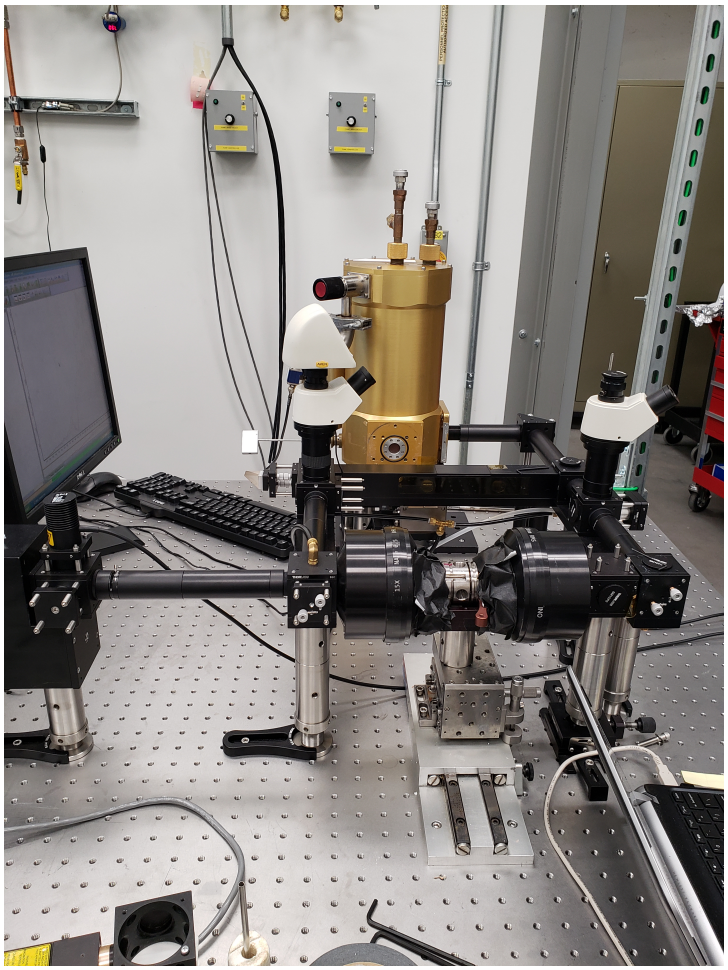

Figure 3.9: High pressure far infrared instrumentation at NSLS-II 22-IR-1 beamline.

Chapter 4

Infrared nano-spectroscopy of ferroelastic domain walls in hybrid improper ferroelectric $Ca_3Ti_2O_7$

Ferroic materials are well known to exhibit heterogeneity in the form of domain walls. Understanding the properties of these boundaries is crucial for controlling functionality with external stimuli and for realizing their potential for ultra-low power memory and logic devices as well as novel computing architectures. In this work, we employ synchrotron-based near-field infrared nano-spectroscopy to reveal the vibrational properties of ferroelastic (90° ferroelectric) domain walls in the hybrid improper ferroelectric $Ca_3Ti_2O_7$. By locally mapping the Ti-O stretching and Ti-O-Ti bending modes, we reveal how structural order parameters rotate across a wall. Thus, we link observed near-field amplitude changes to underlying structural modulations and test ferroelectric switching models against real space measurements of local structure. This initiative opens the door to broadband infrared nano-imaging of heterogeneity in ferroics.

4.1 Structure and order parameters across the domain boundary

The structure of $Ca_3Ti_2O_7$ consists of slabs that contain two layers of $CaTiO_3$ perovskite separated by CaO rocksalt layers.At room temperature, $Ca_3Ti_2O_7$ crystallizes in the orthorhombic polar space group $A2_1am$ [67, 11]. This structure [Fig. 4.1(a)] decomposes into three distinct distortions: an out-of-phase octahedral tilt ($a^-a^-c^0$ in Glazer notation [68]) that transforms like the X_3^- irreducible representation of the high-symmetry prototype structure $I4/mmm$, an in-phase octahedral rotation ($a^0a^0c^+$ in Glazer notation) that transforms as X_2^+, and a polar distortion that transforms like Γ_5^-.

Each distortion is represented by a structural order parameter with amplitude Q and phase ϕ [46]. For the chosen setting of the orthorhombic axes relative to the tetragonal axes the twin domains are labelled by different settings of the space group symbol: $A2_1am$ (twin A) and $Bb2_1m$ (twin B). Figure 4.1(b) shows their structure. In twin A, the X_3^- tilt axis (and polarization direction) lie along [-110], whereas they lie along [110] in twin B. The X_2^+ rotation axis lies along [001] in both twins, but the adjacent perovskite slabs have different rotation senses: in twin A the rotations in the two slabs are in-phase (red arrows) whereas in twin B, they are out of phase. The boundaries connect domains with different spontaneous strain states, so mechanical compatibility conditions determine their orientation [69]. The wall symmetry is obtained by combining the symmetry elements of the two domains and those transforming one domain into the other. To go from twin A to B, all three structural order parameters rotate (change phase ϕ) by 90° [Fig. 4.1(b, c)]. Thus, the X_3^- tilt axis rotates by 90°, whereas the sense of the X_2^+ rotation reverses in every other perovskite slab. At the center of the domain wall, the local structure is $C2mm$ [Fig. 4.1(b)], where the X_3^- tilt axes in slabs 1 and 2 are perpendicular to each other (tilts about [100] and [010] axes in slabs 1 and 2, respectively). The X_2^+ rotation is unchanged in slab 1 and zero in slab 2. Thus, the amplitude of the X_3^- order parameter remains relatively constant across the domain wall, whereas the X_2^+ order parameter amplitude is suppressed in the middle of the path [Fig. 4.1(d, e)]. Whether local $C2mm$ structure is realized at the center depends on wall width. If it is atomically thin, the structural change from one domain to the other will

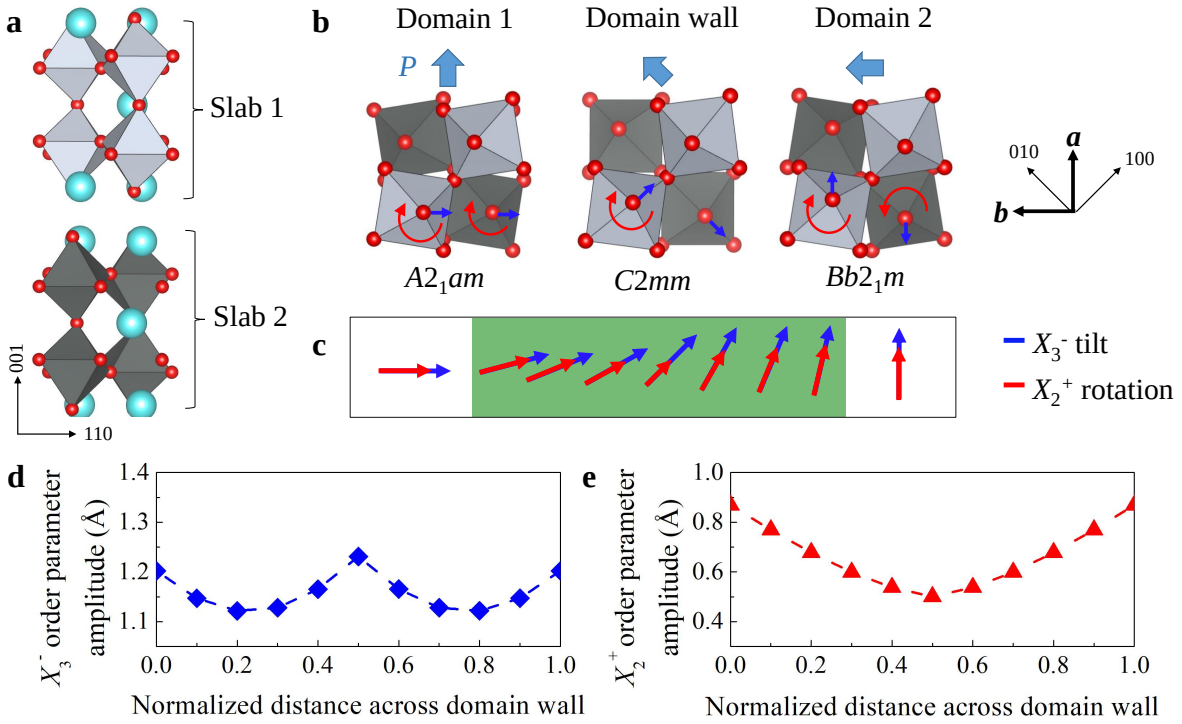

Figure 4.1: Bulk crystal and ferroelastic domain wall structure. (a) Crystal structure of $Ca_3Ti_2O_7$ (space group $A2_1am$). The two $CaTiO_3$ perovskite slabs are shown in light and dark grey, with the Ca cations in light blue. The structure of the two orthorhombic twin domains is shown in (b) real space and (c) order parameter space. The order parameters for the X_3^- octahedral tilt and X_2^+ octahedral rotation are shown with blue and red arrows, respectively, in (c) and the corresponding atomic motions are highlighted using the same colors in (b). The bold black arrows show the setting of the orthorhombic relative to the tetragonal axes. The rotation direction of the Γ_5^- order parameter is indicated by the arrows with a P, indicating polarization direction, above the structures. Upon crossing a ferroelastic domain wall, the octahedral rotation order parameters rotate by 90°; at the midpoint, the local structure is space group $C2mm$. (d, e) The order parameter amplitudes are plotted as a function of the normalized wall width. These amplitudes (reported for a $Z = 2$ cell) were obtained using Density Functional Theory calculations of a trajectory through the bulk energy surface. The units of these structural order parameters are distance (in Å) because they are measuring the amount of distortion - which is calculated by adding up how much all of the atoms in the unit cell are displaced from their high symmetry positions [26].

be abrupt, but if (as observed here) the walls are wide, a macroscopic region with $C2mm$ symmetry may be realized.

4.2 Locating domain walls in different fields of view

Figure 4.2 summarizes the character of the different ferroelastic and ferroelectric domain walls in $Ca_3Ti_2O_7$ at room temperature. The ferroelastic (90° ferroelectric) walls are apparent under cross-polarized light and readily identified by a color change as linear twin boundaries in an optical microscope as illustrated in Fig. 3.5(a). They appear as faint parallel lines in higher magnification images. These features are present in a field of view where we have both atomic force microscopy (AFM) topography and near-field infrared spectroscopy. Nano-spectroscopic line scans (where a spectrum is acquired at each pixel) are set up accordingly to cross ferroelastic walls of interest. The line scans discussed here are indicated with arrows in Fig. 4.2(a, b). We also identified candidate 180° ferroelectric walls for analysis and near-field line scans using a combination of AFM, piezoforce microscopy, and a careful examination of the ridges and topography of the crystal surface as illustrated in Fig. 4.2(c, d). These walls are much more challenging to locate because they meander between twin boundaries.

4.3 Near-field imaging of ferroelastic domain walls

Figure 4.3(a, b) displays the near-field scattering amplitude $A(\omega)$, which encodes the sample dielectric response across two different ferroelastic domain walls in the hybrid improper ferroelectric $Ca_3Ti_2O_7$. Each contour plot shows the line scan distance (the exact position of which is shown in Fig. 4.2(a, b)) vs. frequency, with the color scheme indicative of near-field amplitude. We selected these particular scans to illustrate typical wall variations. The features in $A(\omega)$ are in reasonable agreement with the far field spectra. Differences in the near and far field spectra result from the near-field technique probing a combination of the *ab*-plane and *c*-axis responses whereas the traditional measurement probes the plane perpendicular to the light. Other differences arise at low frequency due to the near-field setup

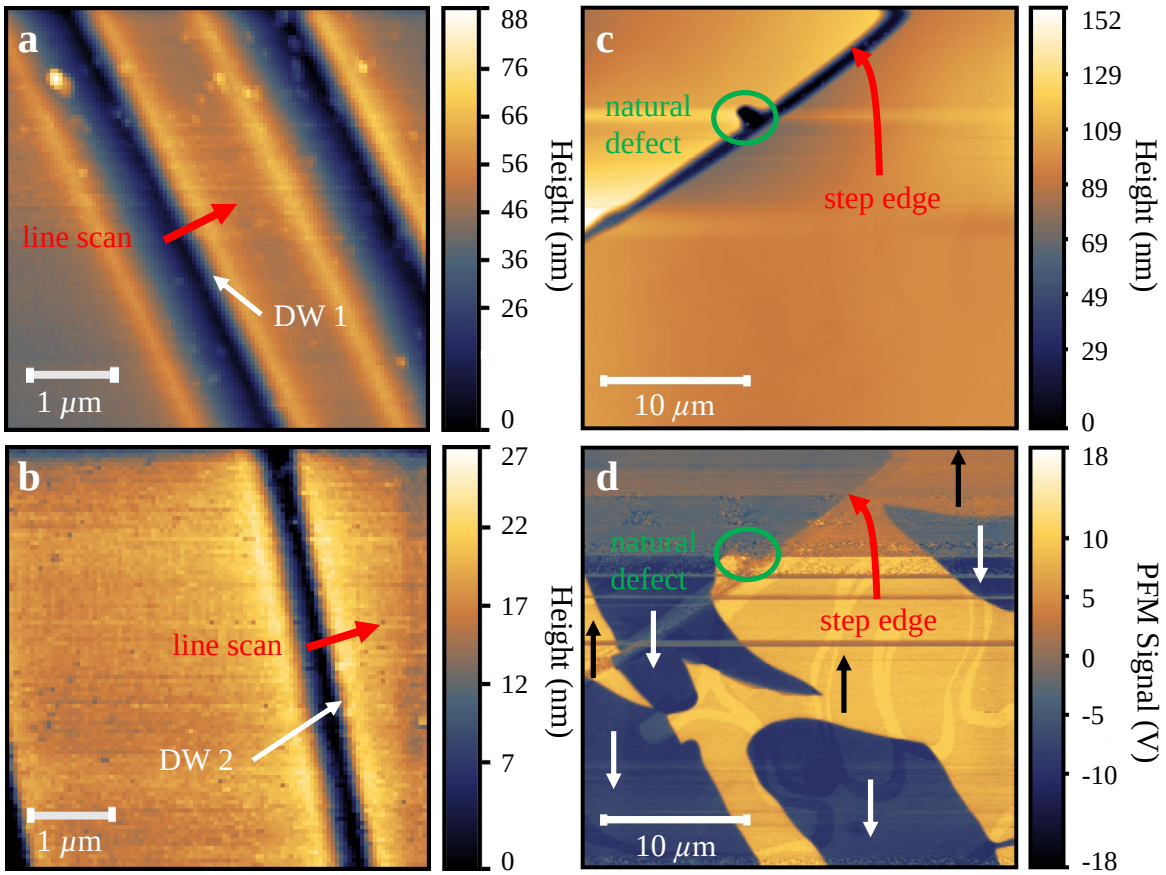

Figure 4.2: Combining microscopy techniques to locate domain walls. (a, b) Atomic force microscopy (AFM) images of the crystal surfaces showing the two ferroelastic domain walls of interest (at the edges of the dark blue stripes). These ferroelastic walls separate domains of different spontaneous strain and are also 90° ferroelectric walls. DW 1 and DW 2 refer to domain walls 1 and 2. Red arrows indicate direction and path of the line scans. The nano-spectroscopic line scans are taken perpendicular to the wall, and the contact angle from one domain to another is 90°. (c) AFM topography of a smooth area near an identified surface defect (indicated by a green circle) and step edge of approximately 100 nm height (indicated with a red arrow) compared with (d) the piezoresponse force microscopy (PFM) image of the same area revealing the placement and orientation of the 180° ferroelectric domains, indicated by yellow(+) or blue(-) regions with black or white arrows to indicate the polarization direction). All of these structures are present at room temperature [26].

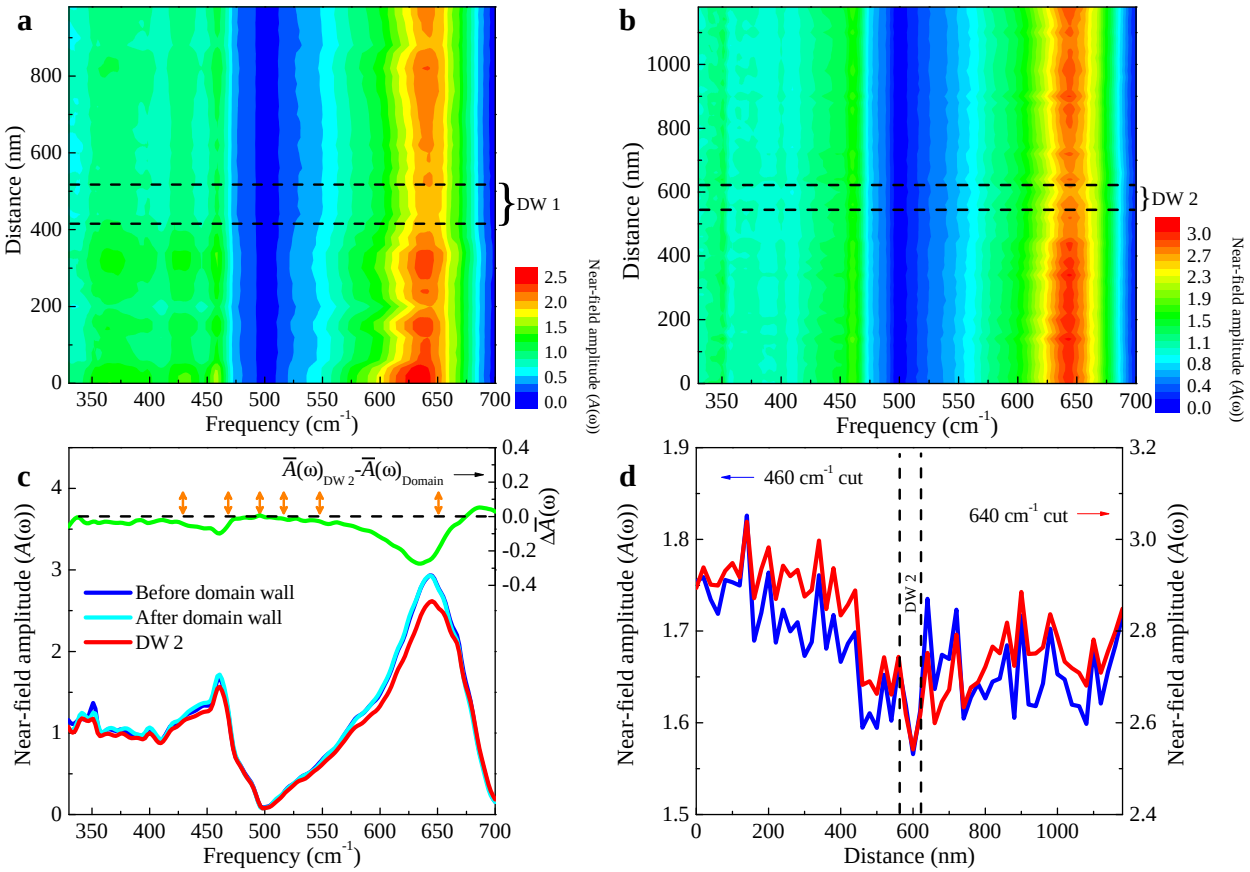

Figure 4.3: Near-field infrared spectroscopy of $Ca_3Ti_2O_7$. (a, b) Contour plots of the near-field amplitude normalized to a gold reference across two different domain walls as indicated in Fig. 4.2(a, b). We label these walls as DW 1 and DW 2. The step size is 20 nm, and the tip resolution is 20 × 20 nm^2. The black dashed lines indicate the domain wall locations, and the brackets denote effective wall widths. (c) Fixed distance cuts of the contour spectra in panel (b) show $A(\omega)$ at the ferroelastic domain wall compared with two different point scans away from the wall. Average changes in the near-field amplitude, calculated as $\Delta\bar{A}(\omega) = \bar{A}(\omega)_{\text{DW 2}}$ - $\bar{A}(\omega)_{\text{Domain}}$, reveal the difference and, at the same time, reduce the noise. Here, the bars denote an average response. This analysis demonstrates that wall phonons have reduced amplitude and a slight blue shift. The 6 A_1 modes within the experimental energy window are indicated by double-sided orange arrows. (d) Fixed frequency cuts of the contour data in panel (b) showing how intensity at 460 and 640 cm^{-1} varies across DW 2. According to the calculation of $\Delta\bar{A}(\omega)$ in panel (c), these frequencies are most sensitive to the presence of the domain wall. They are also very near the calculated A_1 symmetry vibrational modes (shown as orange arrows in panel (c)).

loss of sensitivity when approaching the low frequency cutoff. Regardless, the prominent features of the spectra appear in both the responses.

The ferroelastic (90° ferroelectric) walls are apparent under cross-polarized light and readily identified by a color change as linear twin boundaries in an optical microscope. They appear as faint parallel lines in higher magnification images. These features are present in a field of view where we have both atomic force microscopy (AFM) topography and near-field infrared spectroscopy. Nano-spectroscopic line scans (where a spectrum is acquired at each pixel) are set up accordingly to cross ferroelastic walls of interest. The line scans discussed here are indicated with arrows in Fig. 4.2(a, b). We also identified candidate 180° ferroelectric walls for analysis and near-field line scans using a combination of AFM, piezoforce microscopy, and a careful examination of the ridges and topography of the crystal surface as illustrated in Fig. 4.2(c, d). These walls are much more challenging to locate because they meander between twin boundaries.

A group theoretical analysis shows 72 zone-center phonons that transform as

$$\Gamma = 19A_1 \oplus 17A_2 \oplus 19B_1 \oplus 17B_2. \tag{4.1}$$

The A_1, B_1, and B_2 modes are infrared and Raman active, whereas the A_2 modes are Raman active only. By considering the atomic displacement patterns arising from the phonon eigenvectors, the broad structures with maxima at 645 and 450 cm^{-1} are assigned as Ti-O stretching and Ti-O-Ti bending modes, respectively. In order to associate these localized vibrations with the rotations and tilts that are crucial for the trilinear coupling and ferroelectric switching, we projected out the character of each calculated phonon. This process is described in detail below. We find that the Ti-O stretching mode has a component that transforms as X_2^+, whereas the Ti-O-Ti bending mode transforms primarily as X_3^-. Thus, the symmetry of long-range rotations and tilts are mapped onto the more localized vibrations that are available in our experimental energy window.

Strikingly, the near-field infrared spectrum is sensitive to the ferroelastic (90° ferroelectric) domain walls. Focusing first on Fig. 4.3(a), we see that this line scan crosses a twin boundary. Both spectral amplitude and lineshape are altered across the wall. This is

interesting and important because domain walls in perovskites are traditionally considered to be atomically sharp boundaries [70]. Turning to the second set of data in Fig. 4.3(b), a near-field scan over an independent ferroelastic domain wall again reveals a significant decrease in phonon amplitude and line width. There are also very slight frequency shifts (toward the blue) that are at the limit of our resolution. We therefore see that while the height and width of the wall vary somewhat, the general spectral characteristics are similar.

Point spectra taken from the contour data [Fig. 4.3(c)] unveil a more traditional spectral view of the ferroelastic wall which we can compare to that of the surrounding domain. In order to highlight spectral changes between the wall and the surroundings, we calculated a difference spectrum as $\Delta\bar{A}(\omega) = \bar{A}(\omega)_{\text{DW 2}}$ - $\bar{A}(\omega)_{\text{Domain}}$. This quantity, which reveals average changes (indicated by overbars) in the near-field amplitude is shown in the upper part of Fig. 4.3(c). We find that the wall phonons have reduced amplitude and a slight blue shift. The frequency shift is at the limit of our sensitivity, which unfortunately precludes a more detailed analysis. In any case, the blue shift suggests that there is a spontaneous strain across the wall [69]. The strain across the wall occurs because a ferroelastic wall connects domains with different spontaneous strain states; this strain together with the modulation of order parameter amplitudes determines the local wall structure.

Another property of interest is conductivity. We immediately notice that the twin boundary is semiconducting rather than metallic because there are strong phonons with no hint of a Drude response. Therefore, the ferroelastic walls are not metallic in the conventional sense - although they may be slightly more conducting than their surroundings. To verify this observation, we calculated the band gap for the bulk $C2mm$ structure (the hypothetical structure realized at the midpoint of the domain wall). We find that the computed gap is 0.26 eV less than that of the $A2_1am$ structure - not even close to closing the 3.94 eV gap in this system [71]. This confirms that the ferroelastic walls remain insulating.

Constant frequency cuts in the range of the Ti–O stretching and Ti–O–Ti bending modes uncover another surprising aspect of the walls [Fig. 4.3(d)]. We take these cuts of the contour data at 460 and 640 cm^{-1}, where the change in near-field amplitude between the wall and the surrounding domain as quantified by $\Delta\bar{A}(\omega)$ in Fig. 4.3(c) is strongest. Rather than an atomically sharp boundary, this direct and microscopic probe of the ungerade modes

suggests that there is significant width to the structural distortion. We find widths from 60 to 100 nm for the range of domain walls investigated. This is akin to the length scale of structural relaxations in strained epitaxial thin films. The four different types of ferroelastic domain walls in $Ca_3Ti_2O_7$ (head-to-head, head-to-tail, tail-to-head, and tail-to-tail) [22] along with the prediction from Landau theory that charged walls are thicker than their neutral counterparts [72] provide a natural explanation for this variation.

4.4 Relating near-field amplitude to the order parameters

We now consider how localized phonons map onto the underlying long-range structural order parameters in Fig. 4.1(d, e). We know that the 19 A_1 phonons maintain $A2_1am$ crystal symmetry across the wall, so we can loosely think of the A_1 phonons as excitations of the structural order parameters. Since distortions that transform like the X_3^-, X_2^+, Γ_5^-, and Γ_1^+ irreducible representations of $I4/mmm$ contribute to the $A2_1am$ structure, each A_1 phonon can (in principle) excite a mixture of these four structural order parameters. We therefore performed a change of basis and projected the computed A_1 phonon eigenvectors $\mathbf{e}_{A_1}$ onto a basis of symmetry adapted modes $\mathbf{e}_{i\tau}$ that transform like the irreducible representation $\tau = \{\Gamma_1^+, \Gamma_5^-, X_3^-, X_2^+\}$ of the high-symmetry prototype structure $I4/mmm$. Figure 4.4(a) displays the results of this projection.

Remarkably, certain phonons almost completely overlap with a single symmetry adapted mode–exciting only one structural order parameter. Whereas, others are a mixture. Focusing first on the low-frequency phonons with calculated frequencies 428 and 466 cm^{-1}, we find that they transform primarily as $\mathbf{e}_{X_3^-}$. These phonons are Ti-O-Ti bends although they involve different bond angles [Fig. 4.4(b, c)]. We next consider the phonons calculated to be at 652 and 546 cm^{-1}. They primarily overlap with $\mathbf{e}_{\Gamma_1^+}$ and $\mathbf{e}_{X_2^+}$. The atomic displacement patterns [Fig. 4.4(d, e)] reveal that the 652 cm^{-1} phonon is a *c*-polarized Ti-O stretch, whereas the 546 cm^{-1} mode is an *ab*-polarized Ti-O stretch. This motivates our assignment of the broad

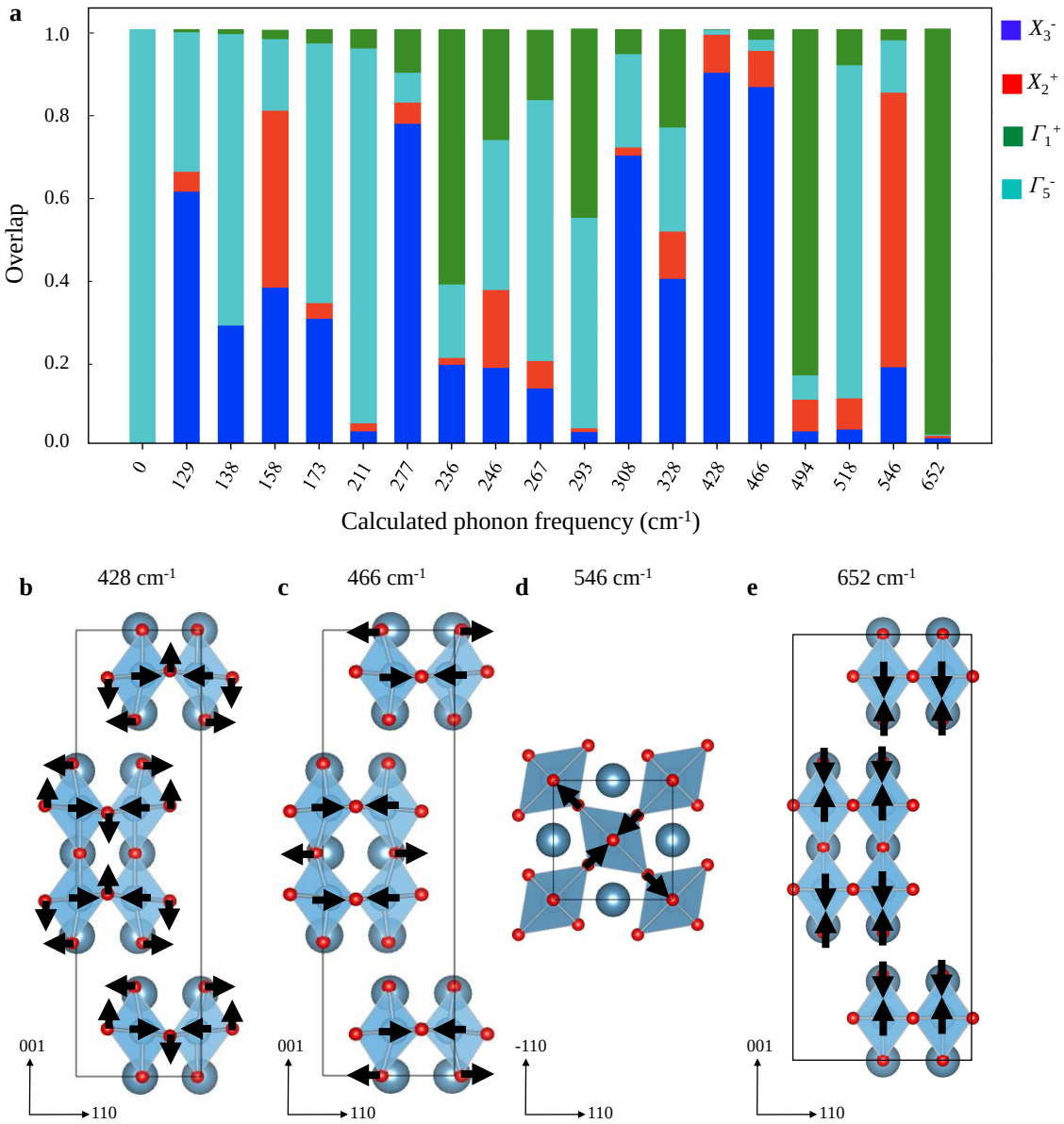

Figure 4.4: Phonon overlaps and calculated displacement patterns. (a) The 19 A_1 symmetry phonon eigenvectors projected onto the $I4/mmm$ symmetry adapted modes. The labels are the calculated phonon frequencies. (b-e) Atomic displacement patterns of four selected phonons from (a). The black arrows display the largest atomic motions within each displacement pattern. The 428 cm^{-1} and 466 cm^{-1} phonons largely consist of Ti-O-Ti bond angle bends. The 546 cm^{-1} and 652 cm^{-1} phonons are bond-stretching modes in the ab plane and along the c-axis, respectively [26].

experimental structure centered at 645 cm^{-1} as bond stretching. The width of the spectral peak suggests that the *ab*-plane and *c*-directed Ti-O stretching modes overlap.

There are three distinct types of oxygen centers in the layered Ruddlesden-Popper structure. These include the equatorial oxygens O_{eq}, as well as two different types of apical oxygens: those that border the rocksalt layer O_{RS}, and those that lie in the middle of the perovskite slab, O_P. We find that the 466 cm^{-1} phonon is primarily a Ti-O_P-Ti bend, whereas the 428 cm^{-1} mode involves both Ti-O_{RS}-Ti and Ti-O_{eq}-Ti bending motion. From this analysis, we conclude that the broad experimental peak centered near 645 cm^{-1} contains excitations that transform like X_2^+ and Γ_1^+, whereas the wide experimental feature centered near 450 cm^{-1} in the near-field spectrum transforms primarily as the X_3^- irreducible representation.

4.5 Order parameter trends vs. near-field response of ferroelastic domain walls

In order to test the correspondence between these symmetry objects, we plotted the near-field amplitude of the 460 and 640 cm^{-1} phonons as a function of distance across the ferroelastic domain wall and overlaid predictions for how the order parameters change across the wall. Importantly, these two frequencies are most sensitive to the presence of the domain wall, and they are very near the calculated A_1 mode positions [Fig. 4.3(c)]. The agreement, while not perfect, has several striking aspects. Our model predicts that the X_3^- amplitude is relatively constant across the wall whereas the amplitude of the X_2^+ rotation changes significantly and is suppressed in the center. Domain wall 1 (DW 1) exhibits reasonable overall agreement with these predictions [Fig. 4.5(a, b)]. The 460 cm^{-1} feature remains relatively constant across the wall, although the anticipated minimum in the fixed frequency scan at 640 cm^{-1} is not well pronounced.

Domain wall 2 (DW 2) is different [Fig. 4.5(c, d)], illustrating what we have found to be typical variations. The fixed frequency near-field scan at 460 cm^{-1} is relatively flat across the the wall - in agreement with the predictions of the X_3^- order parameter. At the same

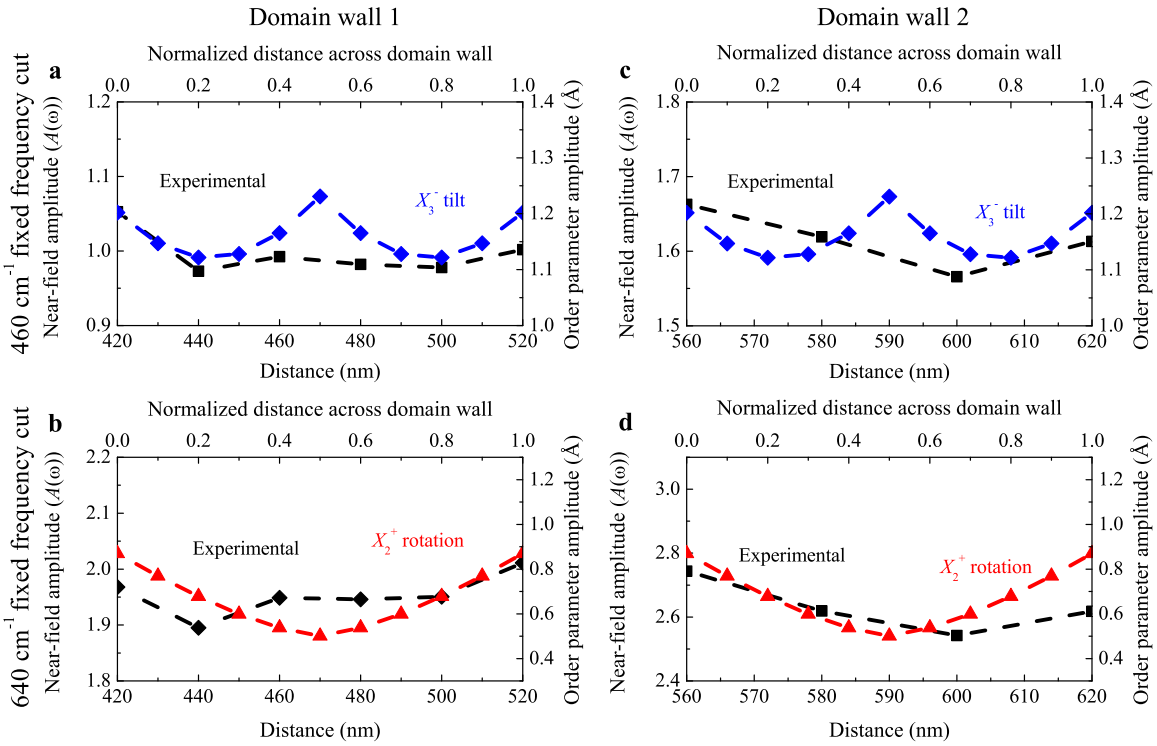

Figure 4.5: Order parameter trends across the structural domain wall. (a-d) Comparison of predicted X_3^- (tilt, blue diamonds) and X_2^+ (rotation, red triangles) order parameters with the measured near-field amplitude at 460 and 640 cm^{-1} across the two walls of interest from Fig. 3(a, b). Both the normalized distance across each wall (treated here as a scalable parameter) as well as the actual line scan positions (determined from the near-field response) are shown. The microscopic distortions across the wall relax more slowly than topography would suggest [26].

time, the 640 cm^{-1} feature is suppressed at the center of the wall, as anticipated. Overall, both X_3^- and X_2^+ track the behavior of the walls fairly well albeit with some deviation. Therefore, we can loosely but not completely think of the long-range rotations and tilts as mapping onto the more localized vibrations that are available in our experimental energy window. Mixing effects [Fig. 4.4(a)] and signal-to-noise issues are the primary reasons that the agreement is not better.

This order parameter framework provides appealing insight into the spatial extent of the ferroelastic domain walls in $Ca_3Ti_2O_7$. Twin boundaries are traditionally considered to be quite narrow [70, 73], although recent work suggests they may be wider than previously supposed [74]. In systems with octahedral rotations, the width and energy of a ferroelastic wall depends on the orientation of the octahedral rotation axes with respect to the domain wall plane [75, 70]. In particular, symmetry constraints that require the octahedral rotation amplitude to go to zero at the center of the wall can increase the wall's width. In $Ca_3Ti_2O_7$, as the X_2^+ order parameter rotates by 90° across the ferroelastic wall, symmetry dictates that the $a^0a^0c^+$ rotation turns off in every other perovskite slab [Fig. 4.1(c)]. The spatial extent of the ferroelastic walls - ranging from from 60 to 100 nm in our measurements - may therefore originate from frustration of the X_2^+ rotation. In addition to the octahedral rotation order parameters discussed here, the spontaneous strain also changes across the ferroelastic wall. This means that the elastic properties also play a role in determining the domain wall width and energy [69, 76]. Based on experimentally reported room temperature lattice parameters [11], $Ca_3Ti_2O_7$ has a small orthorhombic distortion with spontaneous strain $\eta = (b-a)/(b+a) = 8 \times 10^{-4}$. The elastic energy per area of a ferroelastic wall can be estimated as $\eta^2 Cd$, where C is the elastic stiffness coefficient and d is the domain wall width. Taking C from DFT calculations [77] and estimated wall widths from our experiments, we find the elastic energy per area to be roughly 10 mJ/m^2. This relatively small elastic energy contribution may make wide walls a favorable situation.

Chapter 5

Revealing pressure-driven structural transitions in hybrid improper ferroelectric $Sr_3Sn_2O_7$

We combine diamond anvil cell techniques and synchrotron-based infrared spectroscopy with a detailed symmetry analysis and lattice dynamics calculations to uncover a series of pressure-induced structural phase transitions in the hybrid improper ferroelectric $Sr_3Sn_2O_7$. The microscopic character of each high pressure phase is determined by comparing the measured spectrum with the predicted vibrational patterns of several related but distinct candidate space groups. Our analysis reveals a sequence of compression-induced transitions from $A2_1am \leftrightarrow Pnab \leftrightarrow Acaa \leftrightarrow I4/mmm$ at room temperature. Remarkably, this space group progression matches the sequence of temperature-dependent structural transitions observed in $Sr_3Sn_2O_7$ between 77 and 1000 K. Other hybrid improper ferroelectrics display a similar set of transitions, suggesting that pressure and probably strain will be very effective tuning parameters for this entire class of materials.

5.1 Infrared properties of $Sr_3Sn_2O_7$

Figure 5.1(a) summarizes the infrared response of $Sr_3Sn_2O_7$ and our vibrational mode assignments. Both traditional infrared absorption and spectra taken using a diamond anvil

cell are shown. A group theoretical analysis of the $A2_1am$ structure reveals 72 zone-center phonons (24 atoms in the primitive cell) which transform as

$$\Gamma = \underbrace{A_1 \oplus B_1 \oplus B_2}_{\text{Acoustic}} \oplus \underbrace{17A_2 \oplus \underbrace{18A_1 \oplus 16B_1 \oplus 18B_2}_{IR}}_{\text{Raman}}. \tag{5.1}$$

We assign the spectral features of $Sr_3Sn_2O_7$ as indicated in Fig. 5.1(a) using our first principles lattice dynamics calculations. In making these assignments, we prioritize the frequency pattern, intensity, and clustering trends from the calculations. This approach is consistent with the type of analyses that already appears in the literature [10, 78, 79, 80]. In several cases, mode symmetries are grouped to indicate collective contributions to a particular peak. A complete table of mode assignments is given in Table 5.1.

Figure 5.1(b, d) displays the infrared spectra of $Sr_3Sn_2O_7$ as a function of pressure. There are a number of peaks that appear, disappear, shift, and split. Examples are labeled α - γ. These features provide a basis for determining critical pressures. For instance, the appearance of the 225 cm^{-1} feature (β) and the reduction of the 110 cm^{-1} structure above approximately 2 GPa indicates the development of a high pressure phase, which we label HP1. To determine the symmetry of HP1, we analyze several different candidate space groups and calculations of their phonons, comparing these predictions with the experimental spectrum. This process is detailed in the next section. The 225 cm^{-1} feature disappears again near 15 GPa, indicative of a second structural phase transition. The 280 cm^{-1} mode (γ) behaves similarly. It develops a shoulder around 270 cm^{-1} at 2 GPa which disappears after 15 GPa, providing further evidence for a distinct structural phase, henceforth called HP2. At the same time, the 150 cm^{-1} mode (α) hardens in HP1 before softening slightly in HP2. Moreover, the feature near 330 cm^{-1} blue shifts under compression, splits weakly in HP1, comes back together in HP2, and softens and diminishes in the final phase (HP3). The signature of HP3 is subtle. It includes (i) a number of peaks converging near 320 cm^{-1} which causes an apparent "narrowing" of this structure (Fig. 5.1(b)), and (ii) several vibrational modes (especially at 165 and 178 cm^{-1}) shifting across the transition regime (Fig. 5.1(c)).

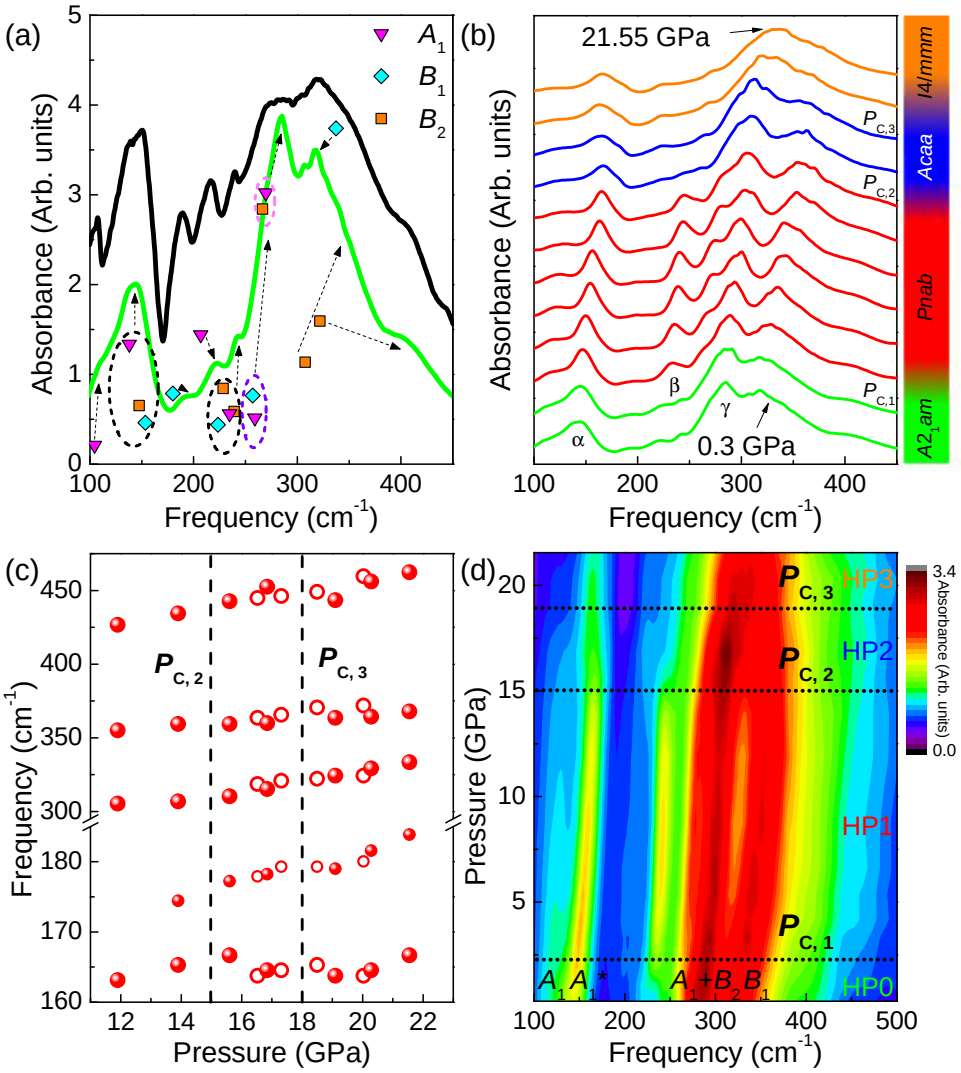

Figure 5.1: (a) Infrared response of $Sr_3Sn_2O_7$ measured using traditional spectroscopic techniques at 300 K (black) and inside the diamond anvil cell at ambient pressure (green). Colored symbols indicate predicted mode positions, symmetries, and intensities. (b) Infrared response of $Sr_3Sn_2O_7$ under pressure at room temperature. The curves are offset for clarity only. The color scheme denotes the four structural phases. The labels α, β, and γ indicate the 150, 225 and 280 cm^{-1} features, respectively, as mentioned in the text. (c) Frequency vs. pressure plot of selected modes that show the critical pressures $P_{C,2}$ and $P_{C,3}$. The filled and open circles denote separate runs. Error bars are on the order of the symbol size. (d) Contour plot of the data in panel (b). The vibrational features of the ambient pressure phase and the critical pressures are labeled [27].

Table 5.1: Calculated Γ-point phonon frequencies (in cm^{-1}) of the $Sr_3Sn_2O_7$ $A2_1am$ phase.

Mode	Freq.		Mode	Freq.		Mode	Freq.		Mode	Freq.
$A_1(1)$	84.61		$A_2(1)$	83.96		$B_1(1)$	80.37		$B_2(1)$	98.90
$A_1(2)$	104.46		$A_2(2)$	95.19		$B_1(2)$	122.52		$B_2(2)$	104.66
$A_1(3)$	114.85		$A_2(3)$	118.40		$B_1(3)$	134.52		$B_2(3)$	120.42
$A_1(4)$	137.89		$A_2(4)$	144.02		$B_1(4)$	144.97		$B_2(4)$	147.14
$A_1(5)$	159.77		$A_2(5)$	150.37		$B_1(5)$	153.43		$B_2(5)$	147.55
$A_1(6)$	169.19		$A_2(6)$	168.20		$B_1(6)$	179.91		$B_2(6)$	172.68
$A_1(7)$	179.92		$A_2(7)$	185.44		$B_1(7)$	223.39		$B_2(7)$	214.70
$A_1(8)$	206.85		$A_2(8)$	225.18		$B_1(8)$	234.81		$B_2(8)$	228.61
$A_1(9)$	219.29		$A_2(9)$	270.37		$B_1(9)$	256.96		$B_2(9)$	239.23
$A_1(10)$	234.75		$A_2(10)$	280.54		$B_1(10)$	284.23		$B_2(10)$	266.57
$A_1(11)$	259.13		$A_2(11)$	313.62		$B_1(11)$	337.33		$B_2(11)$	307.75
$A_1(12)$	269.77		$A_2(12)$	324.13		$B_1(12)$	355.54		$B_2(12)$	321.82
$A_1(13)$	333.70		$A_2(13)$	389.94		$B_1(13)$	500.14		$B_2(13)$	335.16
$A_1(14)$	379.59		$A_2(14)$	481.30		$B_1(14)$	553.35		$B_2(14)$	352.03
$A_1(15)$	422.45		$A_2(15)$	565.73		$B_1(15)$	609.99		$B_2(15)$	404.28
$A_1(16)$	502.81		$A_2(16)$	618.79		$B_1(16)$	658.07		$B_2(16)$	511.66
$A_1(17)$	573.71		$A_2(17)$	716.09					$B_2(17)$	621.50
$A_1(18)$	609.20								$B_2(18)$	705.50

The color scheme in Fig. 5.1(b) captures these four distinct structural phases. We label the critical pressure as $P_{\mathrm{C},1}$, $P_{\mathrm{C},2}$, and $P_{\mathrm{C},3}$.

Figure 5.1(d) summarizes these findings in the form of a contour plot. Mode symmetries are also indicated according to our assignments for the $A2_1am$ phase (Fig. 5.1(a)). Based upon the appearance, disappearance, and frequency shifts of various vibrational modes under compression, the critical pressures of $Sr_3Sn_2O_7$ are 2, 15, and 18 GPa. As we shall see below, the trends across $P_{\mathrm{C},1}$ are not those of a simple group-subgroup relationship, although those at $P_{\mathrm{C},2}$ and $P_{\mathrm{C},3}$ do follow group-subgroup relations. The transition at $P_{\mathrm{C},3}$ corresponds to a restoration of the aristotype $I4/mmm$ symmetry.

5.2 Understanding the symmetry of the high pressure phases

In order to identify the symmetries of these high pressure states, we combine group theoretic methods and first principles lattice dynamics calculations to explore a range of possible structural phases of $Sr_3Sn_2O_7$. We select candidate phases by noting that formally, the X_3^-, X_2^+, and X_1^- octahedral rotation distortions shown in Fig. 5.2 are described by two-dimensional order parameters [46]. We thus consider all space groups generated by distinct directions of these order parameters, as well as their combinations. The entire set of symmetries that we consider is shown in Fig. 5.3

We then perform structural relaxations of $Sr_3Sn_2O_7$ with the symmetry constrained to each of the space groups shown in Fig. 5.3. As expected, we find the $A2_1am$ structure has the lowest energy. We find that the lowest energy structures above $A2_1am$ have symmetries $Pnam$, $Pnab$, and $C2/c$. The $Pnam$ structure exhibits an $a^-a^-c^+$ rotation pattern as found in $A2_1am$, except that the "sense" of the in-phase rotation is reversed across the rocksalt layer. This phase is known to occur locally as "stacking" domain walls [46] in the $A2_1am$ phase. Both $Pnab$ and $C2/c$ host an $a^-a^-c^-$ rotation pattern (with the difference between them being the rotation "sense" across the rocksalt layer). As noted above, $Pnab$ has been observed above 410 K in the x-ray diffraction of $Sr_3Zr_2O_7$ and $Sr_3Sn_2O_7$ [81, 82]. To

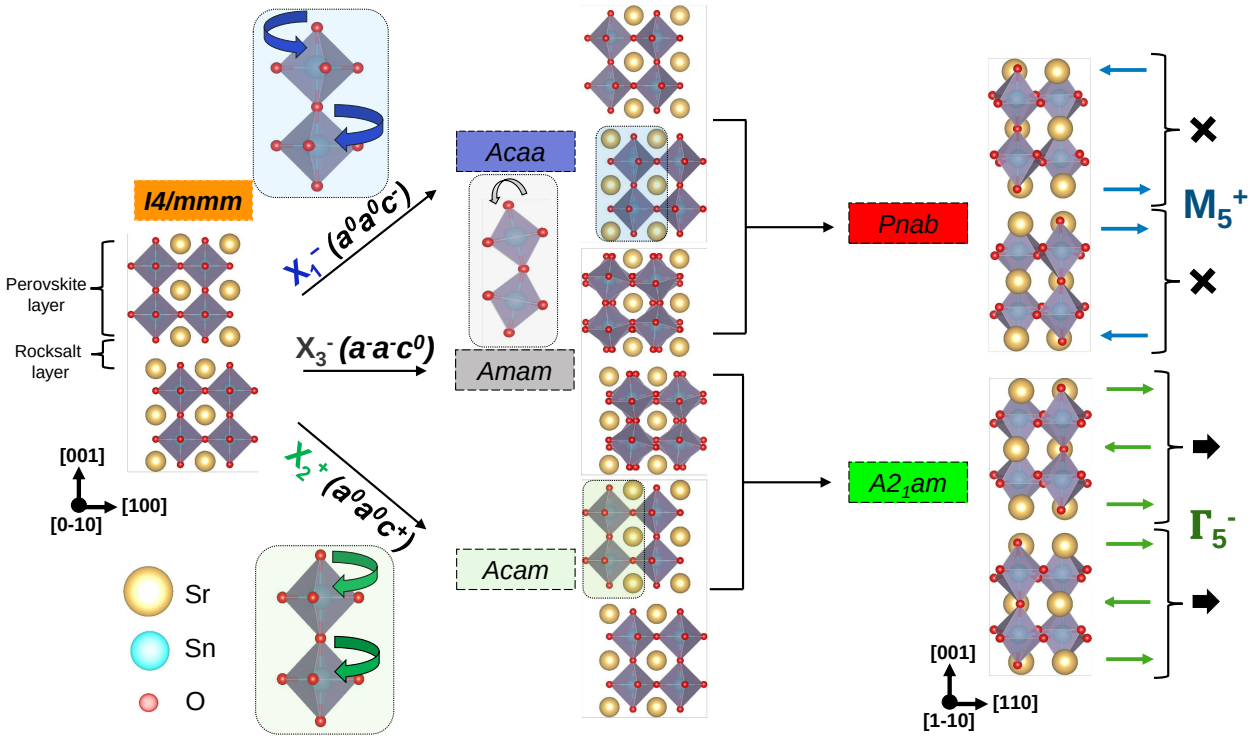

Figure 5.2: Structural phases of $Sr_3Sn_2O_7$ that are accessible via temperature [81] and pressure. Starting with the high-symmetry parent structure $I4/mmm$, the condensation of $a^0a^0c^-$, $a^-a^-c^0$, and $a^0a^0c^+$ octahedral rotation patterns leads to structures with $Acaa$, $Amam$, and $Acam$ symmetries, respectively. The symmetries of these octahedral rotations are given by irreducible representations of $I4/mmm$ as indicated. Combining the $a^-a^-c^0$ and $a^0a^0c^+$ rotations leads to the polar $A2_1am$ structure, whereas combining $a^-a^-c^0$ and $a^0a^0c^-$ rotations leads to the $Pnab$ structure. In each of these structures, a third distortion, primarily consisting of Sr displacements, is induced by a coupling to the octahedral rotations. In $A2_1am$, there is a net Sr displacement in each perovskite layer (green arrows), leading to a polarization, whereas in $Pnab$ the displacements in each layer cancel (blue arrows) [27].

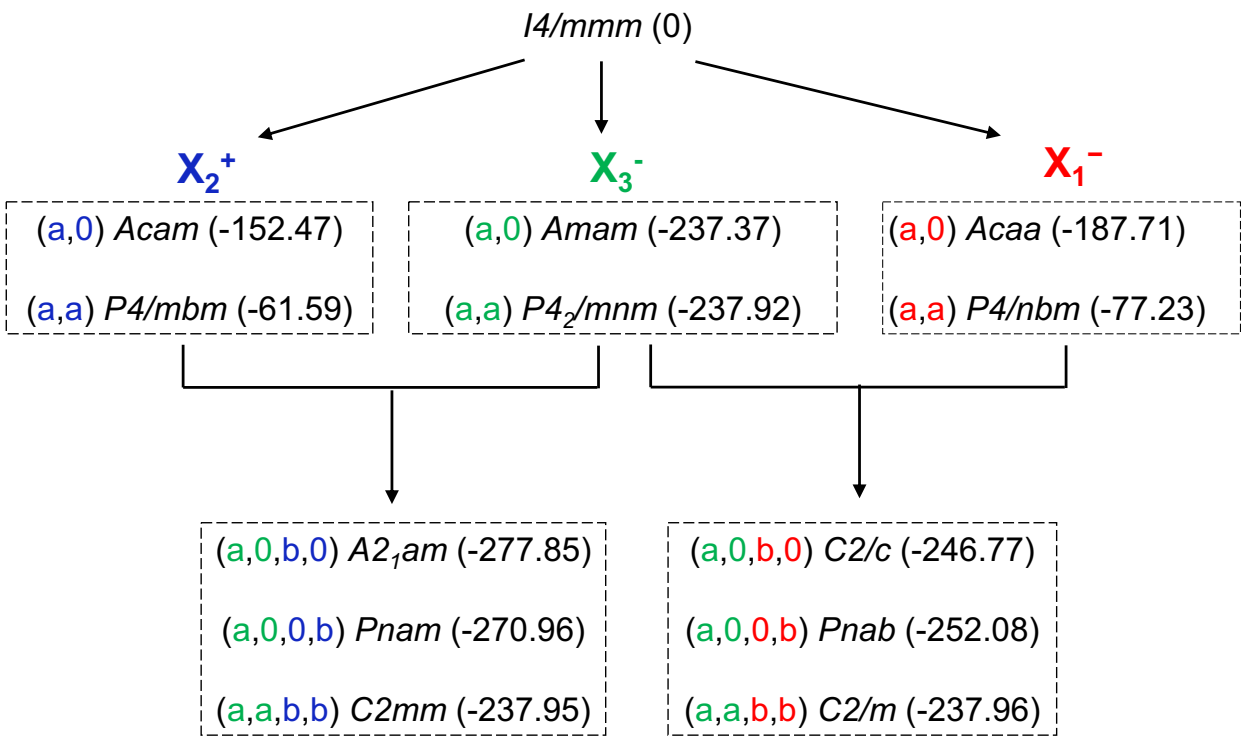

Figure 5.3: Structural phases of $Sr_3Sn_2O_7$ considered in this work. The X_2^+, X_3^-, and X_1^- irreducible representations of $I4/mmm$ generate the space groups shown in the top row, while their combinations generate the space groups in the bottom row. The order parameter directions that define each space group are to the left of the space group symbol (color coded with the relevant irreducible representation). The total energies obtained from DFT structural relaxations of $Sr_3Sn_2O_7$ with symmetry constrained to each of these space groups are given in meV per formula unit with respect to the $I4/mmm$ energy [27].

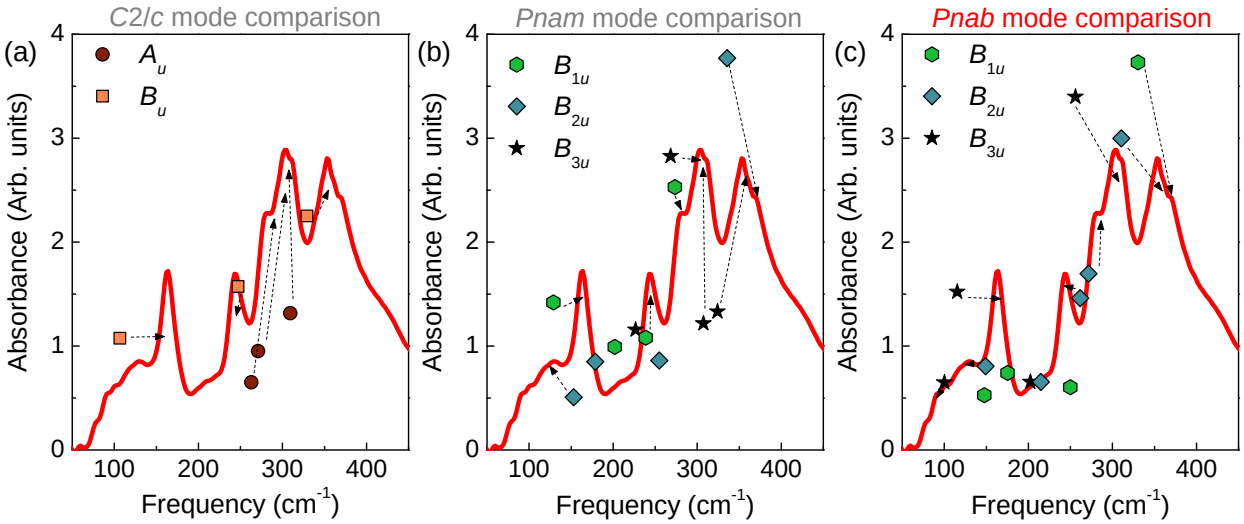

Figure 5.4: Infrared spectrum of $Sr_3Sn_2O_7$ in the HP1 high pressure phase at 11.9 GPa compared with computed mode positions, symmetries, and intensities for three candidate space groups. The space groups considered are: (a) $C2/c$, (b) $Pnam$, and (c) $Pnab$. $Pnab$ provides the superior match in terms of most prominent features and overall pattern - as indicated by the heading in red [27].

check the effect of pressure on the energetics of these low-energy phases, we then perform calculations as a function of increasing pressure for each structural phase. At each pressure, we calculate the difference in enthalpy between each of these phases and $A2_1am$ ($\Delta H = \Delta E + P\Delta V$) [83, 84, 85, 86]. We find that the enthalpy difference between our identified low-energy structures ($Pnam$, $Pnab$ and $C2/c$) and $A2_1am$ decreases slightly (but remains positive) as a function of increasing pressure. Thus, in contrast with our experimental results, we do not see a transition from $A2_1am$ to a different symmetry phase under pressure in DFT. This could be because the octahedral rotation amplitudes calculated with these methods are larger than those in the experimental structure (see Table 5.2), or because our calculations are at 0 K while the experiments are performed at room temperature. Nevertheless, these calculations still provides a useful set of candidate space groups against which we can test our spectra.

For each of these low-energy phases we then calculate the phonons and infrared intensities in order to identify the symmetry of HP1. We assign spectral features by comparing our theoretically predicted mode positions, patterns, and intensities with the experimental spectrum. As an example of this procedure, we overlaid the infrared spectrum of $Sr_3Sn_2O_7$ at 11.9 GPa with the calculated mode positions and intensities of the different candidate space groups for the HP1 phase (Fig. 5.4). While $C2/c$ and $Pnam$ are in reasonable agreement with the measured spectrum, the calculated mode pattern for $Pnab$ symmetry provides superior agreement in terms of mode intensities and clustering patterns, particularly the presence of low frequency B_{3u} mode and a clearer correspondence of infrared mode intensities around 200 cm^{-1}. We therefore assign the symmetry of the HP1 phase of $Sr_3Sn_2O_7$ to be $Pnab$. In addition to providing a superior match in terms of the most prominent features and overall pattern under pressure, this non-polar space group is consistent with variable temperature infrared reflectance (Fig. 5.5) and Raman scattering [87, 88]. One important aspect of the $A2_1am \leftrightarrow Pnab$ transition is that these space groups do not have a group-subgroup relationship, as can be seen from the symmetry group tree in Fig. 5.3. This behavior is indicative of a first-order phase transition. The same discontinuous transition has been observed with increasing temperature in $Sr_3Sn_2O_7$ and $Sr_3Zr_2O_7$ [81, 82].

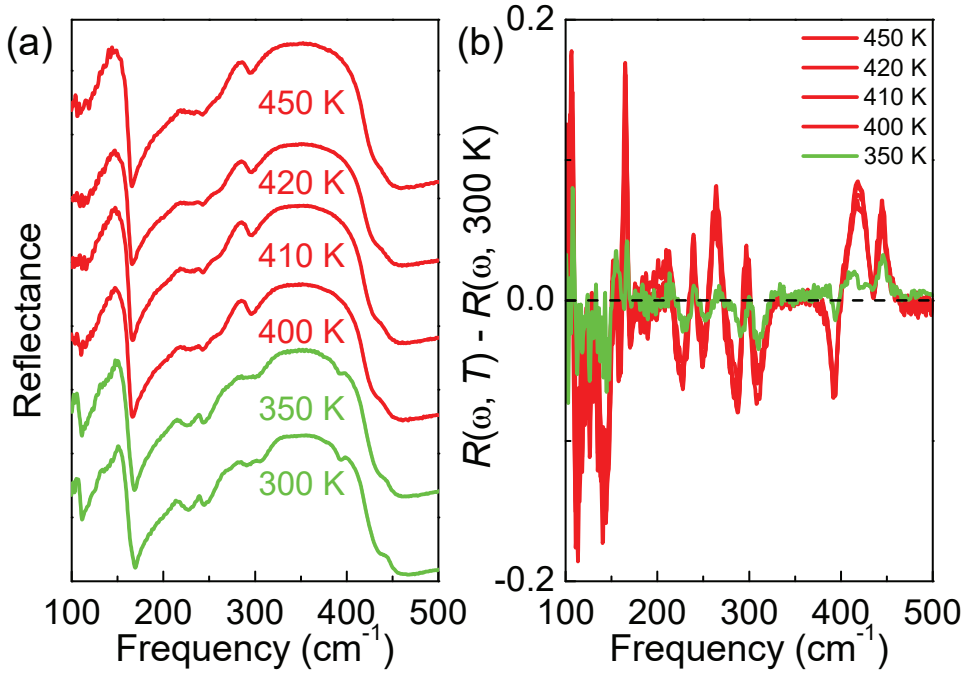

Figure 5.5: (a) Infrared reflectance of $Sr_3Sn_2O_7$ as a function of temperature across $T_{C,1}$. The curves are shifted for clarity. (b) Reflectance differences highlighting the temperature-induced spectral changes across $T_{C,1}$. The green and red curves correspond to the $A2_1am$ and $Pbna$ phases, respectively [27].

To further search for signatures of this phase transition, we also use our first principles lattice dynamics calculations to check the pressure evolution of low frequency phonons in the $A2_1am$ phase. Our approach is motivated by the soft mode theory of structural phase transitions [89, 90, 91]. This theory has been most widely applied to understanding displacive ferroelectric transitions, where a phonon softens to zero frequency at the transition point. However, soft modes also can be present in discontinuous transitions albeit with a finite frequency at the transition point [91]. Our calculations on $Sr_3Sn_2O_7$ reveal one low frequency phonon (80.37 cm^{-1}) with B_1 symmetry that softens slightly under increasing pressure (Fig. 5.6(b)). Visualizing the displacement pattern of this phonon (Fig. 5.6(a)), we find that it consists primarily of Sr displacements and an out-of phase $a^0a^0c^-$ octahedral rotation which are very similar to the M_5^+ and X_1^- distortions in $Pnab$, respectively. This observation further supports our assignment of $Pnab$ symmetry to the HP1 phase, although this particular mode is not observed in the experimental spectra due to the limitations of our technique. We note that a similar finite frequency phonon softening was observed at a pressure induced phase transition in $GdVO_4$ [92].

We take a similar approach to identify the symmetry of the HP2 and HP3 phases. From the space groups shown in Fig. 5.3 we choose to consider structures where one or both of the octahedral rotations in $Pnab$ is removed: $Amam$ ($a^-a^-c^0$), $Acaa$ ($a^0a^0c^-$), and $I4/mmm$ (no rotations). We also consider $P4_2/mnm$, which consists of $a^-b^0b^0$ and $b^0a^-b^0$ octahedral rotations in alternating perovskite slabs and is known to be stabilized in other n = 2 Ruddlesden-Popper materials by chemical substitution [93]. Like $Amam$, the $P4_2/mnm$ structure is established by the X_3^- irrep, except the order parameter is in a symmetry-distinct direction [46]. Our calculations show that of these phases, $Amam$ has the lowest enthalpy at low pressures, whereas at higher pressures $Acaa$ has lower enthalpy, and in fact the enthalpy difference $H_{Acaa} - H_{A2_1am}$ becomes negative above ≈20 GPa. We then compared the phonon frequencies and infrared intensities calculated for each of these candidate space groups with the measured spectrum at 16.85 GPa (Fig. 5.7).We notice that while $I4/mmm$ provides a poor match, $P4_2/mnm$, $Amam$ and $Acaa$ are good candidates. Focusing on the finer details and the low frequency peaks, we find that theory and experiment agree slightly better for $Acaa$ than $Amam$ and $P4_2/mnm$. This, together with our calculations indicating a negative

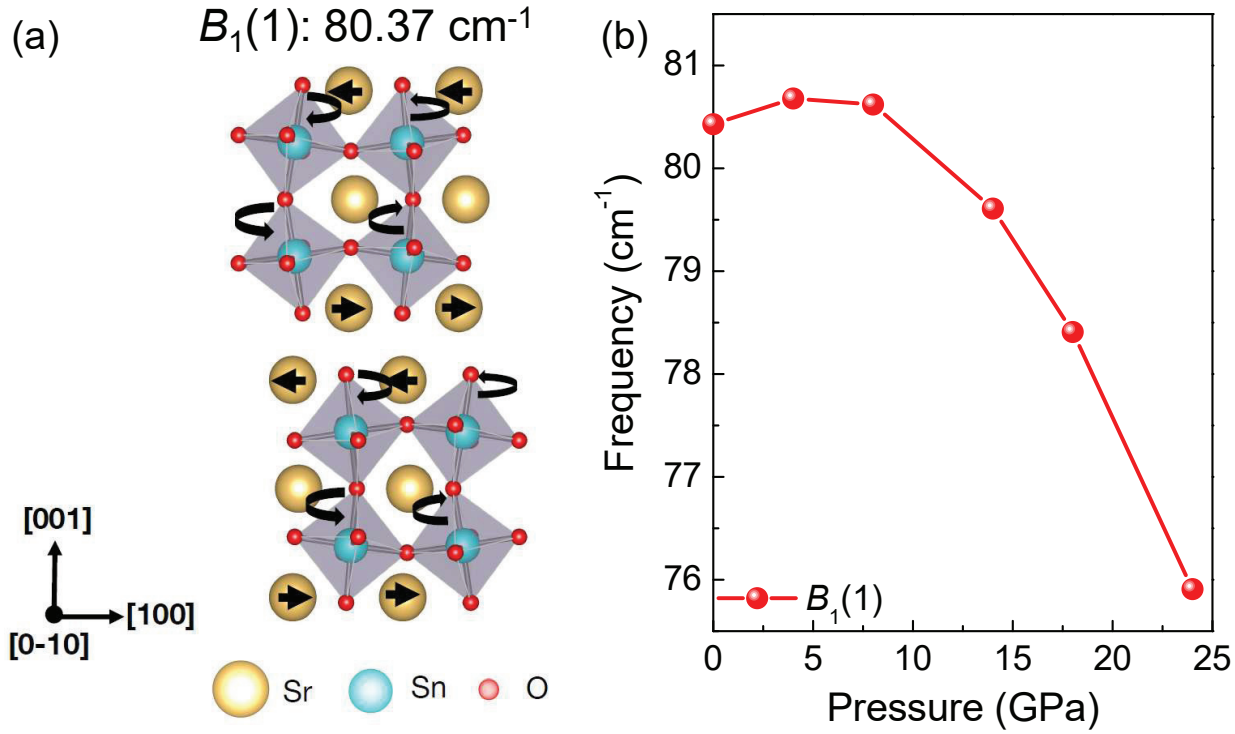

Figure 5.6: (a) Main atomic motions that contribute to the $B_1(1)$ phonon of $Sr_3Sn_2O_7$ in the $A2_1am$ structure. (b) Predicted evolution of the frequency of the $B_1(1)$ phonon with pressure [27].

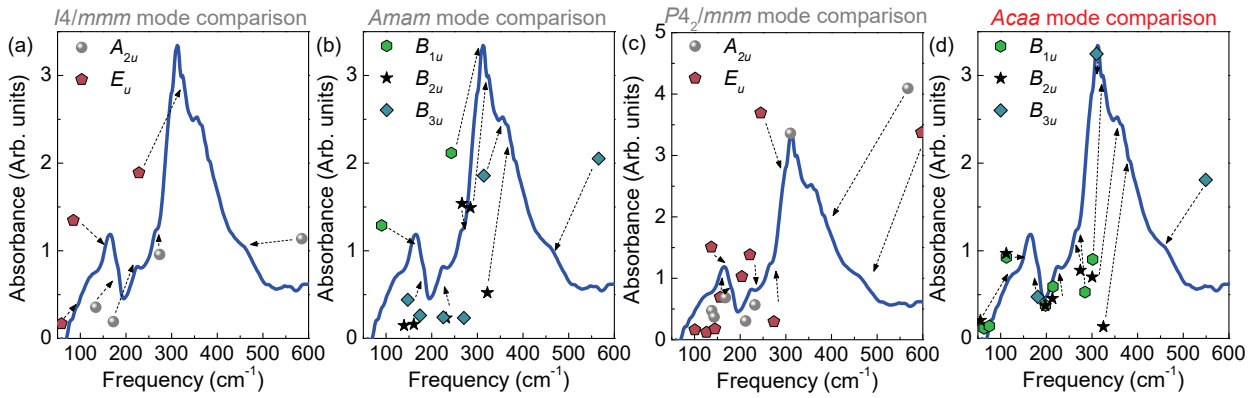

Figure 5.7: Infrared spectrum of $Sr_3Sn_2O_7$ at 16.85 GPa (blue curve) taken in the diamond anvil cell compared with calculated mode positions and intensities for four candidate space groups. Calculated vibrational modes and intensities for $I4/mmm$, $Amam$, $P4_2/mnm$, and $Acaa$ space groups as compared with the measured spectrum. Symmetries of theoretically predicted modes are given by colored markers. (a, c) For $I4/mmm$ and $P4_2/mnm$, the A_{2u} and E_u modes are indicated by grey spheres and maroon pentagons respectively. (b, d) For $Amam$ and $Acaa$, the B_{1u}, B_{2u}, and B_{3u} modes are indicated by green hexagons, black stars, and teal diamonds, respectively. The $Acaa$ space group provides superior overall agreement as indicated by the red label [27].

enthalpy difference $H_{Acaa} - H_{A2_1am}$ at a slightly higher pressure, leads us to assign $Acaa$ symmetry to the HP2 phase.

Finally, to find the symmetry of HP3, we again compare the $I4/mmm$, $Amam$, and $Acaa$ theoretical intensities with the experimental spectrum obtained at 21.55 GPa as shown in Fig. 5.8 Our analysis suggests a close agreement with $I4/mmm$. We expect the transitions to HP2 and HP3 to be second-order because they follow a group-subgroup relationship and occur over a range. The overall sequence of transitions in $Sr_3Sn_2O_7$ under pressure is therefore $A2_1am \leftrightarrow Pnab \leftrightarrow Acaa \leftrightarrow I4/mmm$. This is exactly the same sequence of phases observed with increasing temperature in $Sr_3Sn_2O_7$ [81].

5.3 Structure-property relations in $n = 2$ Ruddlesden Popper hybrid improper ferroelectrics

In the previous sections, we identify the critical pressures and corresponding phase transitions in $Sr_3Sn_2O_7$ using a combination of high pressure infrared spectroscopy, group theoretic analysis, and lattice dynamics calculations. Here, we more broadly examine the pattern of structural distortions and phase transitions under external stimuli in a larger class of $n = 2$ Ruddlesden-Popper compounds.

We begin by comparing the pressure dependence of $Sr_3Sn_2O_7$ with other members of the $n = 2$ Ruddlesden-Popper series. Subtle differences related to the evolution of the structural order parameters impact how each system departs from $A2_1am$ symmetry [94]. In $Ca_3Ti_2O_7$, inelastic neutron scattering reveals that the X_2^+ octahedral rotation is significantly more sensitive to pressure than the X_3^- rotation [56]. Interestingly, the opposite is true in the Mn counterpart; the $a^-a^-c^0$ rotation is more responsive to compression than the $a^0a^0c^+$ rotation [95]. $Ca_3Ti_2O_7$ is also overall stiffer than $Ca_3Mn_2O_7$ as evidenced by the phonon behavior across the critical pressure [96]. In both cases, the polar $A2_1am$ ground state is lost between 5 and 8 GPa with the transition range in the Mn analog being somewhat narrower (between 5 and 6 GPa). Therefore, $Ca_3Ti_2O_7$ and $Ca_3Mn_2O_7$ only have a single critical

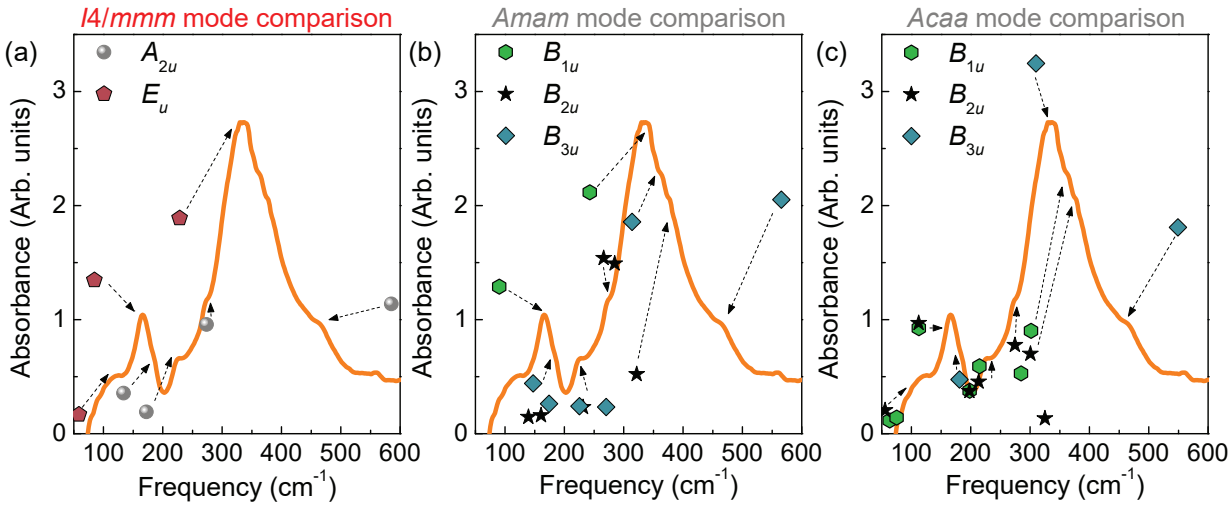

Figure 5.8: Infrared spectrum of $Sr_3Sn_2O_7$ at 21.55 GPa (orange curve) taken in the diamond anvil cell compared with calculated mode positions and intensities for three candidate space groups. Calculated vibrational modes and intensities for $I4/mmm$, $Amam$, and $Acaa$ space groups as compared with the measured spectrum. Symmetries of theoretically predicted modes are given by colored markers. (a) For $I4/mmm$, the E_u and B_u modes are indicated by maroon pentagons and grey spheres respectively. (b-c) For $Amam$ and $Acaa$, the B_{1u}, B_{2u}, and B_{3u} modes are indicated by green hexagons, black stars, and teal diamonds, respectively. The $I4/mmm$ space group provides superior agreement as indicated in red [27].

pressure within the range investigated thus far [96], although additional transitions are anticipated and negative thermal expansion is predicted [97] at significantly higher pressures.

As discussed above, $Sr_3Sn_2O_7$ negotiates the same sequence of phases under both compression and temperature. Given this analogy, we next examine the temperature-dependent structural phase transitions for various materials across the $n = 2$ Ruddlesden-Popper series. We begin by noting that the sequence of temperature-dependent phase transitions in $Sr_3Zr_2O_7$ is remarkably similar to the temperature (and pressure) transitions in $Sr_3Sn_2O_7$ [81, 82]. A combination of x-ray diffraction, second harmonic generation, and theoretical analysis reveals that $Sr_3Zr_2O_7$ undergoes the same first-order $A2_1am \leftrightarrow Pnab$ transition as $Sr_3Sn_2O_7$, although the transition temperature is higher (approximately 700 K compared to 400 K in $Sr_3Sn_2O_7$). With increasing temperature, one of the rotations turns off, although the two materials differ in the following respect: in $Sr_3Sn_2O_7$ there is a transition to $Acaa$ ($a^0a^0c^-$ rotations) at 700 K, whereas in $Sr_3Zr_2O_7$ there is a transition to $Amam$ ($a^-a^-c^0$ rotations) at 900 K. Finally, both materials go into the high-symmetry $I4/mmm$ phase above 1000 K. These higher temperature transitions are second-order [81, 82].

Expanding the comparison to a broader set of $n = 2$ Ruddlesden-Popper materials reveals that the number and symmetries of the high-temperature phases varies with composition [82]. That said, the tolerance factor τ, defined as $\tau = \frac{r_{A-\mathrm{O}}}{\sqrt{2}(r_{B-\mathrm{O}})}$, where $r_{A-\mathrm{O}}$ and $r_{B-\mathrm{O}}$ are the B-O and A-O bond lengths respectively, is a useful quantity for formulating trends [98]. In fact, Yoshida *et. al.* identified a relationship between the tolerance factor τ and the Curie temperature T_C which holds across many chemical compositions [82]. One clear take-away is that materials with smaller tolerance factors have a higher T_C. From a structural viewpoint, this makes sense because materials with smaller tolerance factors have larger octahedral rotation amplitudes (Table 5.2). Since the phase transitions in these $n = 2$ Ruddlesden-Popper materials all involve changes to the octahedral rotations, it takes more energy (higher temperature) to drive the transition in the low tolerance factor compounds.

Inspired by these results, we decided to investigate whether the tolerance factor can serve as a similar descriptor for pressure-driven transitions in this family of materials. Unfortunately, the situation is not so simple. From our discussion above, we note that of the systems for which there is available data, $Sr_3Sn_2O_7$ has the lowest critical pressure

Table 5.2: Tolerance factor (τ) and amplitudes of the X_3^- and X_2^+ octahedral rotations for selected n=2 members of the Ruddlesden-Popper series. The octahedral rotation amplitudes are obtained by decomposing ambient pressure $A2_1am$ structures with respect to the high-symmetry $I4/mmm$ structure, and are reported for a 24 atom cell in units of Å. The tolerance factors were calculated using A-O and B-O bond lengths obtained from the bond valence model [100, 101, 102], assuming 12- and 6-fold coordination for the A and B cations, respectively. The experimental values–except the P_C for $Sr_3Sn_2O_7$ reported in this work–were obtained from literature [103, 104, 105, 106, 81, 82].

Material	τ	X_3^- (DFT)	X_2^+ (DFT)	X_3^- (Expt)	X_2^+ (Expt)	P_C (GPa)	T_C (K)
$Sr_3Zr_2O_7$	0.942	1.27	0.86	1.07	0.78	–	700
$Ca_3Ti_2O_7$	0.946	1.20	0.87	1.01	0.83	5-8	1100
$Sr_3Sn_2O_7$	0.957	1.18	0.76	0.89	0.67	2	400
$Ca_3Mn_2O_7$	0.977	0.87	0.79	0.66	0.73	5-6	270-320

($P_{C,1}$). The critical pressures of $Ca_3Mn_2O_7$ and $Ca_3Ti_2O_7$ are somewhat higher. Consulting Table 5.2, we see that $Ca_3Ti_2O_7$ has a smaller tolerance factor (and correspondingly larger octahedral rotation amplitudes) than $Sr_3Sn_2O_7$, thus this pair of materials suggests a critical pressure - tolerance factor trend similar to the temperature-dependent result discussed above. However, $Ca_3Mn_2O_7$, with the largest tolerance factor, is out of line with this trend. We hypothesize that the different B-site chemistry of $Ca_3Mn_2O_7$ (partially filled d-shells), may play a role in this difference. We note that studies of ABO_3 perovskites demonstrate that B-site chemistry (in particular partially-filled d-shells) influences the pressure response [99].

Another way to organize the data is to analyze trends based upon both the A and B site chemistry. The limited number of experimental results on polar $\leftrightarrow$ non-polar transitions in hybrid improper ferroelectrics under pressure makes it challenging to reach firm conclusions. Here we explore some potentially important factors based on the presently available data, which may be refined as more experimental results become available in the future. The similar evolution of phases with temperature in $Sr_3Sn_2O_7$ and $Sr_3Zr_2O_7$ suggests grouping materials based on their A-site cation, which is consistent with the role of the A-site in determining size effects, bonding preferences [107], and compressibility [108]. Based on this similarity, it is plausible that $Sr_3Zr_2O_7$ may show a similar sequence of phase transitions under pressure as those observed in $Sr_3Sn_2O_7$. If so, synchrotron-based infrared work in a diamond anvil cell would allow structure-property comparisons with $Sr_3Sn_2O_7$ to be developed. Turning to the two Ca-containing materials, we note that P_C of $Ca_3Ti_2O_7$ is higher than that of $Ca_3Mn_2O_7$ (Table 5.2), suggesting a possible P_C - tolerance factor relation within a subset of materials with the same A-cation, although lacking data on additional compounds we cannot make a definitive statement on this trend.

We next explore the possibility of trends based on the B-site cation. The four materials in Table 5.2 all have different B-site cations, of which one is a p-block element (Sn), one has a partially filled d-shell (Mn), and two have formally empty d orbitals (Ti, Zr). Considering the octahedral rotation amplitudes in Table 5.2, we note that the amplitude of the X_3^- rotation increases monotonically with decreasing tolerance factor, whereas the X_2^+ rotation amplitude in $Sr_3Sn_2O_7$ is anomalously small given its tolerance factor. This could be connected to Sn being a p-block element and its relatively low P_C. $Sr_3Zr_2O_7$ and $Ca_3Ti_2O_7$ both have

larger X_2^+ and X_3^- order parameter amplitudes. This is largely due to their lower tolerance factors [81], although their similar B-site chemistry also could play a role. This B-site relationship may lead to similar evolution of structural order parameters with pressure, although clearly one needs to measure to much higher levels of compression for $Ca_3Ti_2O_7$. In contrast, with its partially filled d-shell $Ca_3Mn_2O_7$ is likely to undergo a different sequence of structural distortions with the suppression of the X_3^- rotation being more important [95].

We therefore propose three significant factors that together determine the pressure response for a particular $n = 2$ Ruddlesden-Popper material: (i) the tolerance factor, with smaller tolerance factor compounds having higher critical pressures, (ii) the A-site occupation which appears to be primarily a size effect, and (iii) the B-site chemistry. The tolerance factor seems to determine the phase transition range and critical temperature/pressure within the same set of A-site compounds, whereas B-site chemistry governs the development of structural order parameters and in turn the progression of phase transitions according group-subgroup relationships. Further pressure-dependent studies on a broader suite of $n = 2$ Ruddlesden-Popper materials would allow further refinement of these relationships. The overall lower critical pressures of $Sr_3Sn_2O_7$ compared to the other materials, makes it more amenable to physical tuning and appealing for applications.

5.4 Developing the schematic temperature-pressure phase diagram of $Sr_3Sn_2O_7$

To further explore connections between the temperature- and pressure-induced phase transitions in $Sr_3Sn_2O_7$, we construct a schematic temperature-pressure (T - P) phase diagram in Fig. 5.9. The transition temperatures are taken from previous structural studies [88, 81], and the pressure-driven transitions are from the present work. We draw the phases boundaries between these points using a typical asymptotic dependence near the critical values. They are blurred to indicate uncertainty. The intermediate temperature - pressure regime is also blurred - again to indicate uncertainty.

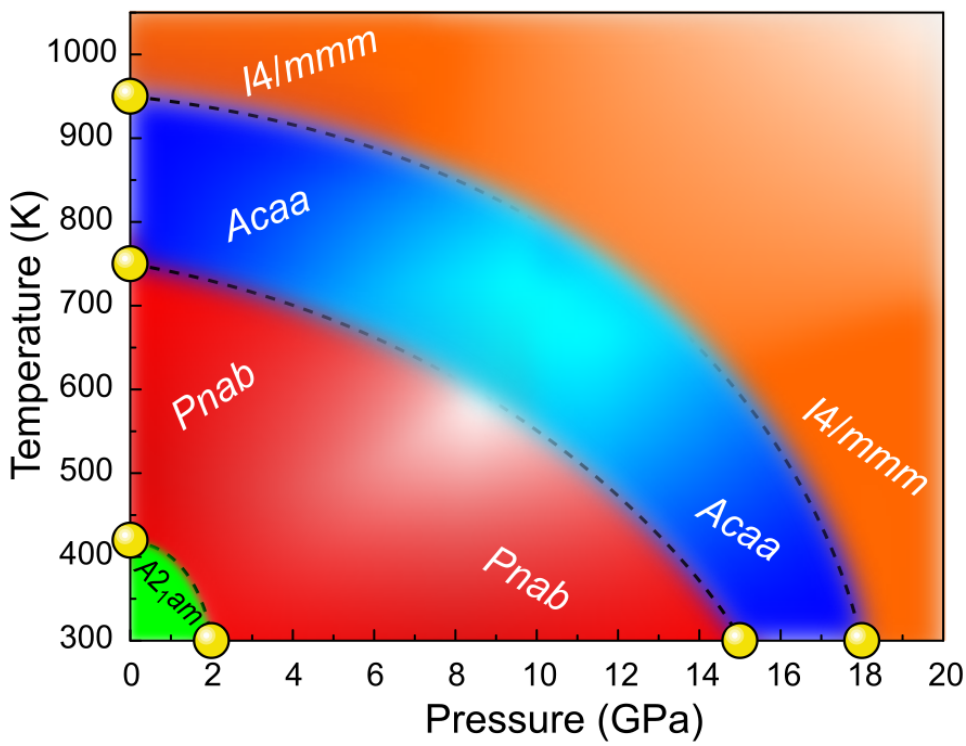

Figure 5.9: Schematic temperature - pressure (T - P) phase diagram of $Sr_3Sn_2O_7$ developed from the critical pressures identified in this work as well as the critical temperatures from literature [82]. These values are indicated by yellow spheres. Error bars are on the order of symbol size. Blurring indicates uncertainly in the position and shape of the phase boundaries - especially in the intermediate temperature and pressure regime [27].

Figure 5.9 highlights how both temperature and pressure instigate the same $A2_1am \leftrightarrow Pnab \leftrightarrow Acaa \leftrightarrow I4/mmm$ sequence of transitions. There is thus an unexpected compatibility and commutability of tuning parameters even though (i) we do not know the details of how the phase boundary lines evolve at intermediate temperatures and pressures and (ii) there is no simple energy equivalence between these two quantities. The crucial difference is that pressure (and very likely strain) access these phases and their functionalities at room temperature - an essential characteristic of viable applications. A similar temperature/pressure correspondence may be present in other hybrid improper ferroelectrics.

We note that the equivalence between the sequence of phases accessed with pressure and temperature in $Sr_3Sn_2O_7$ is unusual; typically temperature and pressure have opposite effects because increasing temperature results in thermal expansion and increasing pressure induces volume contraction. A similar temperature/pressure phase transition equivalence has been observed in perovskite $LaAlO_3$ [109, 110] despite its positive thermal expansion [111], which can be attributed to the BO_6 octahedra being more compressible than the AO_{12} polyhedra [112, 113]. In particular, perovskites with more compressible BO_6 octahedra generally exhibit a negatively sloped phase boundary in the P-T phase diagram and opposite sign changes of entropy and volume ($\Delta S > 0$, $\Delta V < 0$) [112]. Fig. 5.9 displays such a negative phase boundary, and we hypothesize that a similar mechanism may underlie the pressure/temperature behavior of $Sr_3Sn_2O_7$.

Chapter 6

Pressure-induced phase transition and phonon softening in h-$Lu_{0.6}Sc_{0.4}FeO_3$

6.1 Infrared response of $Lu_{0.6}Sc_{0.4}FeO_3$ under pressure

Figure 6.1 summarizes the vibrational response of $Lu_{0.6}Sc_{0.4}FeO_3$ under pressure. We begin by comparing the infrared absorption measured in the diamond anvil cell with that taken using traditional techniques. They are in good overall agreement. We assign the vibrational modes using our lattice dynamics calculations of the two end members $LuFeO_3$ and $ScFeO_3$. The frequencies, overall pattern, and relative intensities of the predicted modes are an excellent match with the measured spectrum [Fig. 6.1(a)]. Note that a number of features are grouped, which is expected for a system like $Lu_{0.6}Sc_{0.4}FeO_3$ which has a complex mode pattern and certain aspects of a solid solution with both Lu and Sc substitution on the A site. A complete list of mode assignments is provided in Table 6.1. From Fig. 6.1(a) it is clear that the computed $LuFeO_3$ and $ScFeO_3$ modes are clustered together for the two materials (both in terms of frequency and intensity). There are only a few outliers such as those around 300 cm^{-1} and 570 cm^{-1} in $ScFeO_3$ with no corresponding modes for $LuFeO_3$. Therefore, for the subsequent analysis in the rest of this work, we consider only the $LuFeO_3$ phonon frequencies/intensities for comparison with the experimental spectra.

Figure 6.1(b) shows how the infrared spectrum of $Lu_{0.6}Sc_{0.4}FeO_3$ evolves with increasing pressure. There are two striking trends: the divergence of A_1 and E_1 modes that are part

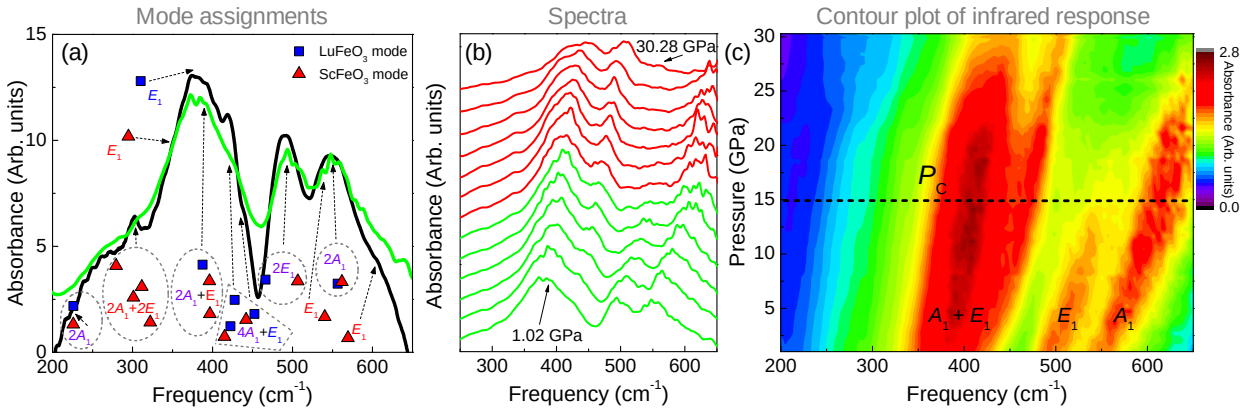

Figure 6.1: (a) Traditional (black) and diamond anvil cell (green) infrared spectrum of $Lu_{0.6}Sc_{0.4}FeO_3$ at ambient conditions. Theoretical mode positions and intensities of the end member compounds $LuFeO_3$ and $ScFeO_3$ in the $P6_3cm$ space group are shown with blue squares and red triangles, respectively. The modes are grouped together to show how we assign various predicted excitations to the observed experimental features. Table 6.1 summarizes these assignments in tabular rather than graphical form. (b) Infrared response of $Lu_{0.6}Sc_{0.4}FeO_3$ as a function of pressure. The spectra are off-set for clarity, and the color (green vs. red) indicates the phase. (c) Contour plot of the same data as in panel (b). The critical pressure (P_C) is indicated with a dashed line at 15 GPa [28].

Table 6.1: Summary of mode assignments for h-$Lu_{0.6}Sc_{0.4}FeO_3$ at ambient conditions in the $P6_3cm$ space group. For assignments containing both Lu and Sc, we list the frequency of the Lu mode first. Table is reproduced from [28].

Experimental peak frequency (cm^{-1})	Lu/Sc mode	Assigned theoretical mode frequencies (cm^{-1})	
		A_1	E_1
225	Both	226.1, 225.8	–
302	Sc	301.1, 311.6	294.9, 322.1
350	Sc	–	294.9
375	Lu	–	310.3
385	Both	387.5, 396.2	396.8
420	Both	427.7, 422.4	415.1
440	Both	452.4, 442.0	–
490	Both	–	466.4, 506.7
540	Sc	–	540.3
550	Both	556.5, 561.8	–
602	Sc	–	569.4

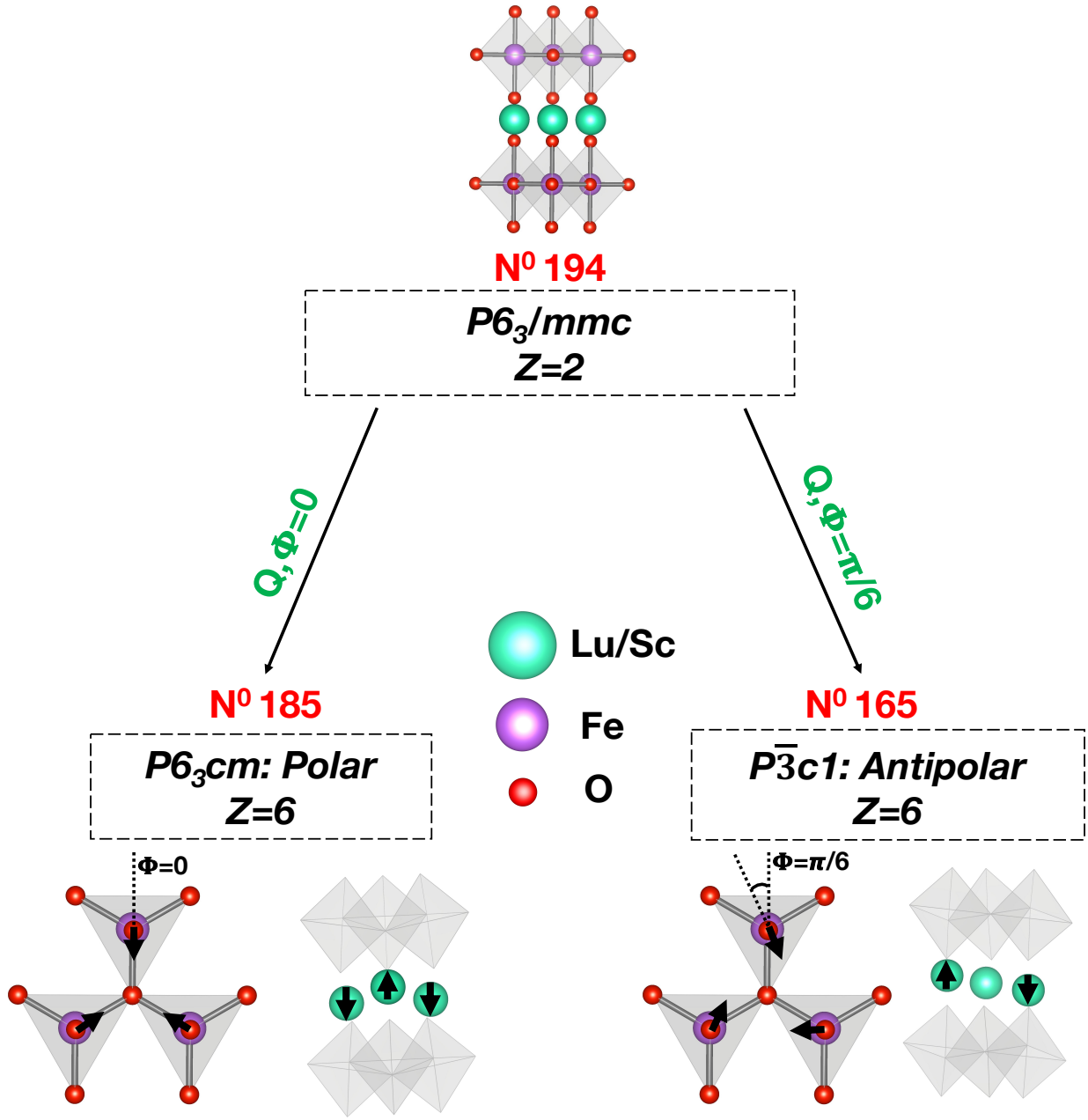

Figure 6.2: Group-subgroup relationship along with the corresponding distortion modes between high-symmetry $P6_3/mmc$ and low-symmetry $P6_3cm$ (polar)/$P\bar{3}c1$ (antipolar) structures of hexagonal (Lu/Sc)FeO_3. The K_3 mode distortions are given in terms of a two-component order parameter (Q, Φ) similar to the hexagonal manganites [114] [28].

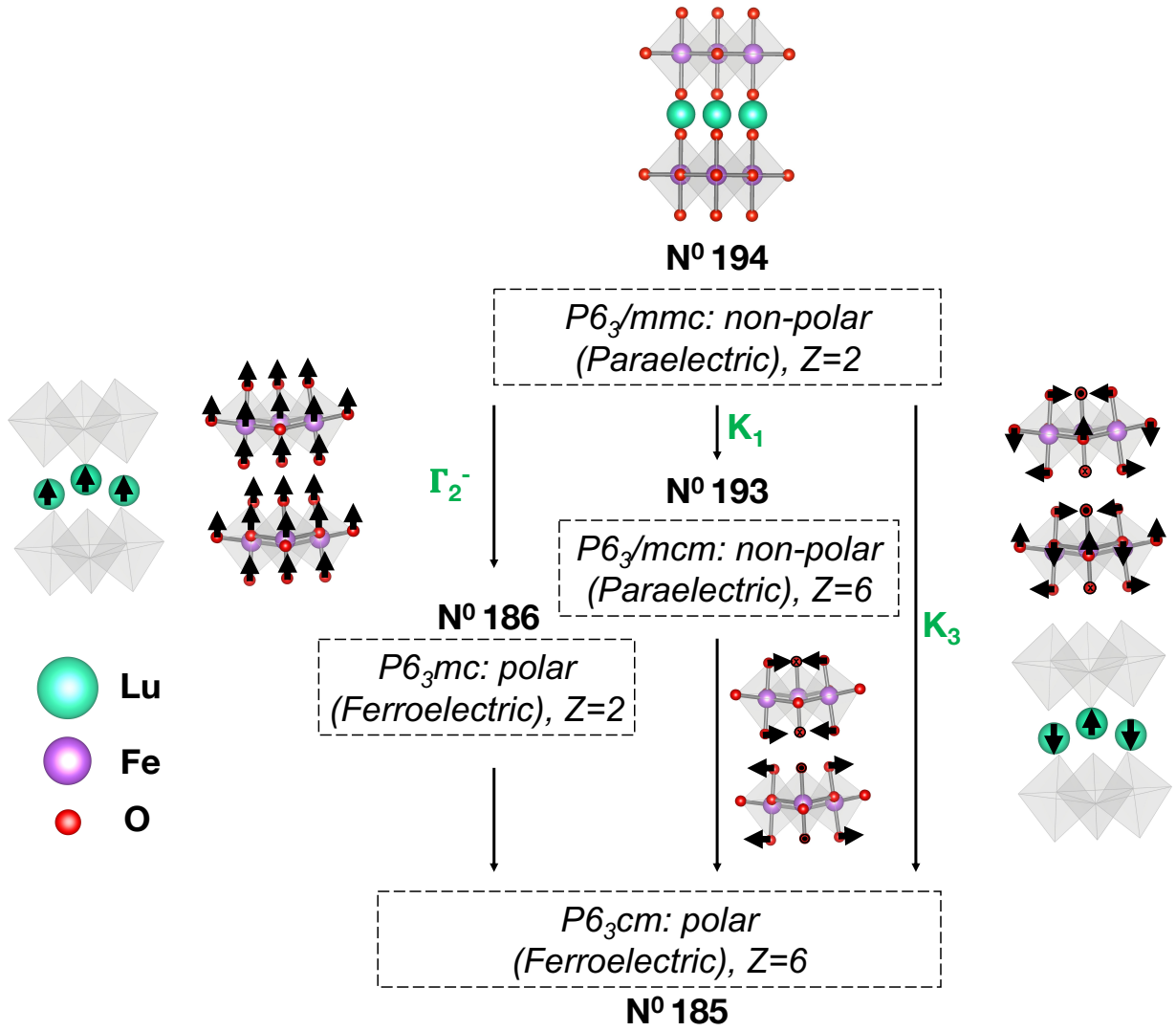

Figure 6.3: Group-subgroup relationship along with the corresponding distortion modes between the high-symmetry $P6_3/mmc$ (non-polar) and the low-symmetry $P6_3cm$ (polar)/$P6_3mc$ (polar)/$P6_3/mcm$ (non-polar) structures of $LuFeO_3$ [28].

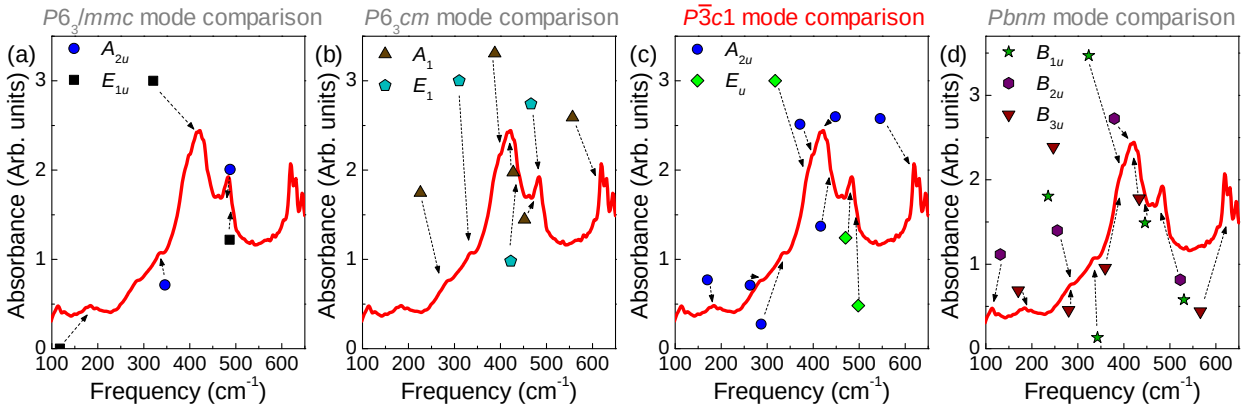

Figure 6.4: Infrared spectrum of $Lu_{0.6}Sc_{0.4}FeO_3$ in the high pressure phase (at 20 GPa) compared with calculated mode positions, symmetries, and intensities for four candidate high-pressure space groups: (a) $P6_3/mmc$, (b) $P6_3cm$, (c) $P\bar{3}c1$, and (d) $Pbnm$. The calculations are performed for the end-member compound $LuFeO_3$. The match between experiment and theory for the space group $P\bar{3}c1$ is superior and indicated in red [28].

of the broad feature centered near 380 cm^{-1} and the progressive disappearance of the E_1 mode near 500 cm^{-1}. Based upon these trends, we identify a critical pressure P_C at 15 GPa. Figure 6.1(c) displays the same progression in the form of a contour plot. The intensity changes at P_C are clearly evident.

Group theory predicts several possible structural transition pathways that can occur under pressure. One possibility is that the system transitions from $P6_3cm$ to the high-symmetry $P6_3/mmc$ structure. Figure 6.3 summarizes three possible routes for this: (1) $P6_3cm \rightarrow P6_3mc \rightarrow P6_3/mmc$; (2) $P6_3cm \rightarrow P6_3/mcm \rightarrow P6_3/mmc$; and (3) $P6_3cm \rightarrow P6_3/mmc$. The first two are two-step pathways, whereas the third has a single-step pathway. Examining the experimental data, we observe only one distinct transition as a function of pressure (P_C = 15 GPa). This suggests that the structural phase transition in $Lu_{0.6}Sc_{0.4}FeO_3$ occurs in a single step, ruling out the possibility of the two-step processes like those shown in Fig. 6.3. In addition, the high-symmetry $P6_3/mmc$ structure is stable with respect to Γ_2^- and K_1 phonons that establish the intermediate structures $P6_3mc$ and $P6_3/mcm$, respectively. This leaves the possibility of a direct transition to the $P6_3/mmc$ space group. Other options include the K_3 order parameter rotating under pressure to establish a structure with symmetry $P\bar{3}c1$ [Fig. 6.2], or the system staying in $P6_3cm$ with no symmetry change under pressure. A final possibility is a transition to the orthorhombic $Pbnm$ structure under pressure. As noted above, a pressure-induced hexagonal-orthorhombic transition has been reported in the manganites [115, 116, 117, 118] and indites [119].

In order to determine the space group of the high pressure phase of $Lu_{0.6}Sc_{0.4}FeO_3$, we compare the predicted mode frequencies and intensities of $P6_3/mmc$, $P6_3cm$, $P\bar{3}c1$, and $Pbnm$ to the measured infrared spectrum at 20 GPa. Figure 6.4 summarizes the results of this comparison. It is immediately apparent that the $P6_3/mmc$ fit is too sparse and largely inferior, guiding our assignment of the high pressure phase toward the other candidates. $Pbnm$ has two high intensity modes near 250 cm^{-1} that are unassigned. This is problematic, especially since there are no high intensity spectral features in the vicinity. This leaves polar $P6_3cm$ and antipolar $P\bar{3}c1$ as the remaining candidates [Fig. 6.4(b,c)]. A comparison of the predicted and measured mode patterns below 300 cm^{-1} provides a key test. Examination reveals that $P6_3cm$ offers no assignment for the 200 cm^{-1} peak in the measured spectrum,

and while it provides two high intensity modes near 275 and 320 cm^{-1}, they are not nearly so strong in the experimental response. In contrast, $P\bar{3}c1$ offers three low frequency features with modest intensities that are in reasonable agreement with the measured response. We therefore find the $P\bar{3}c1$ space group to be the best match [Fig. 6.4(c)] and assign it as the symmetry of the high pressure phase.

6.2 Raman scattering response under pressure

To complement our infrared work, we performed Raman scattering measurements on $Lu_{0.6}Sc_{0.4}FeO_3$ under pressure up to 30 GPa [Fig. 6.5]. Unlike the infrared response, the Raman spectrum has only a few distinct well-isolated peaks and peak clusters. This makes mode assignment straightforward. The majority of the Raman-active modes harden with pressure, a typical trend. These features also display linewidth narrowing and very slight slope changes in the vicinity of $P_C = 15$ GPa [Fig. 6.5(c-e)]. There is no evidence for a symmetry modification within our sensitivity. There is, however, a low frequency cluster containing peaks at 88 and 111 cm^{-1} that softens with increasing pressure [Fig. 6.5(a)]. Remarkably, the onset of this mode softening coincides with the 15 GPa critical pressure observed in the infrared. These findings provide additional evidence for a structural phase transition at this pressure.

By combining theoretically predicted mode frequencies and intensities with our experimental data, we assign and track various features as a function of pressure. According to our calculations, the low frequency peak at 111 cm^{-1} is comprised of two modes with an additional lower frequency mode at 83 cm^{-1}. Frequency vs. pressure plots for these three modes, $E_2(1)$, $E_2(2)$, and $E_1(1)$, are shown in Fig. 6.5(b). Given the approximations in our calculations, the theoretical and experimental phonon frequencies can differ from each other. For the purpose of comparison, we apply a rigid shift to the predicted phonon frequencies for each of the modes to match our experimental observation; qualitatively, the predicted behavior matches well with the observed trends.

Figure 6.6 displays the displacement patterns of the three modes that soften under pressure, obtained from calculations for $LuFeO_3$ and $ScFeO_3$ at zero pressure. All three

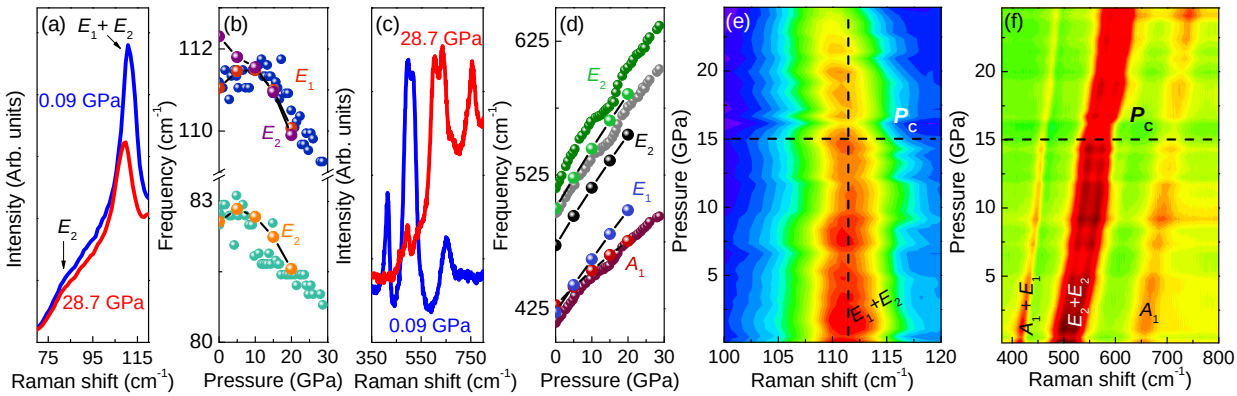

Figure 6.5: (a) Close-up view of the low frequency Raman response of $Lu_{0.6}Sc_{0.4}FeO_3$ in the low and high pressure phases. Mode assignments (E_2 and $E_1 + E_2$) are indicated. (b) Frequency vs. pressure for the modes in (a) showing how they soften under pressure, consistent with our calculations. The theoretical data (red, purple and orange spheres connected by black lines) has been rigidly shifted by a few wavenumbers to overlap with the experimental results (blue and teal spheres). (c) Close-up view of the high-frequency Raman response of $Lu_{0.6}Sc_{0.4}FeO_3$ in the low and high pressure phases. (d) Frequency vs. pressure results for the measurements in (c) along with complementary calculations. Theoretical modes are indicated by green, black, blue, and burgundy spheres connected with black lines with mode symmetries indicated in matching colors. Experimental points are given by green, grey and maroon spheres. (e, f) Contour plots summarize the pressure dependence of the low and high frequency Raman scattering response. Intensity is consistent across both plots and is represented by colors ranging from purple to red corresponding to low and high intensity, respectively. Mode assignments are indicated along the bottom, and the critical pressure is indicated by a horizontal dashed line. The vertical dashed line in (e) is a guide to the eye and highlights the mode softening [28].

modes are characterized by sliding motions of adjacent layers of the crystal structure against each other. The apical oxygens sitting above and below the iron oxide layer sit at crystallographically distinct sites, labelled as O1 and O2 in Fig. 6.6, respectively. Thus in the $E_2(1)$ mode [Fig. 6.6a] slabs of the crystal structure slide against each other with a shearing motion occurring between the iron oxide layer and O2. In contrast, in the $E_2(2)$ mode [Fig. 6.6b] there is the same sliding of slabs but the shearing is between the iron oxide layer and O1. Finally, in the $E_1(1)$ mode [Fig. 6.6c], the iron-oxide and Lu/Sc layers slide against each other, where all Fe atoms and equatorial oxygens displace to the right, and all Lu atoms and apical oxygens displace to the left. The relative amplitudes of the Lu/Sc, Fe, apical oxygen and equatorial oxygen displacements shown in Fig. 6.6 are different for $LuFeO_3$ and $ScFeO_3$, due to the mass difference between Lu and Sc.

The presence of low-frequency Raman-active vibrational modes that soften under pressure suggests the possibility of negative thermal expansion. We therefore calculated mode Grüneisen parameters (γ_i) in order to quantify how the frequency shifts affect the unit cell volume as:

$$\gamma_i = \frac{B}{\omega_i}\frac{\partial \omega_i}{\partial P}. \tag{6.1}$$

Here, B is the bulk modulus, ω_i is the frequency of a given mode, and $\partial\omega_i/\partial P$ is obtained by extracting the slope from frequency vs. pressure plots in the high pressure regime above P_{C}. We employ the bulk modulus of $LuFeO_3$ in this calculation (220 GPa) [120]. The relation of the coefficient of thermal expansion to the Grüneisen parameter is provided below

$$\alpha = \frac{\gamma_{av} c_v}{3B} \tag{6.2}$$

where c_v is the molar heat capacity at constant volume [121, 122]. The main term of interest is γ_{av} which is the mean of the individual mode Grüneisen parameters. This term (along with the molar heat capacity at constant volume and the bulk modulus) goes into the calculation of the coefficient of thermal expansion, α. Looking at the individual γ_i's, we note that the average takes a positive value, guaranteeing that α will also take a positive value. This rules out the existence of negative thermal expansion in $Lu_{0.6}Sc_{0.4}FeO_3$.

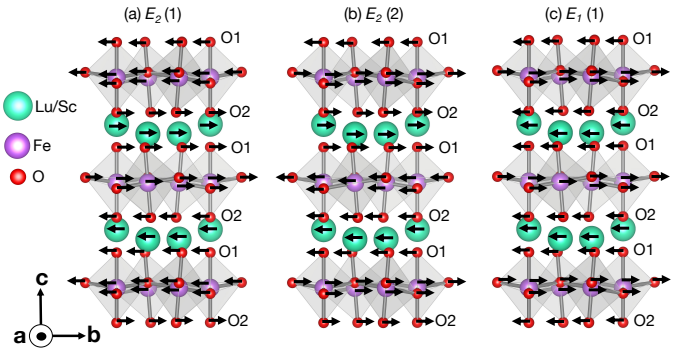

Figure 6.6: Atomic displacements that contribute to the Raman active $E_2(1)$, $E_2(2)$, and $E_1(1)$ modes computed at zero pressure for the ground state $P6_3cm$ structure of $LuFeO_3$ and $ScFeO_3$. The atomic displacement patterns of $Lu_{0.6}Sc_{0.4}FeO_3$ are qualitatively similar, as the primary effect of the mixed Lu/Sc composition is a change in mass [28].

6.3 Structure-property relationships and comparison with the rare earth manganites and other materials

In order to place our findings in context with other hexagonal oxides, we next compare our results with trends in related materials. Previous studies on other isostructural systems have generally reported a transition to the orthrhombic *Pbnm* phase under pressure. For example, work on h-$YMnO_3$ has shown that it stays in space group $P6_3cm$ up to 20 GPa and then converts to an orthorhombic *Pbnm* structure [115, 116]. Work on $ErMnO_3$ [117] and $TmMnO_3$ [118] found a hexagonal-orthorhombic crossover at somewhat lower pressures (17 and 10 GPa, respectively). Finally, high pressure work on h-$YInO_3$ found a coexistence of the orthorhombic and hexagonal phases between 15-30 GPa [119].

In contrast with the hexagonal manganites and indites, we do not observe a transition to an orthorhombic space group in $Lu_{0.6}Sc_{0.4}FeO_3$. To rationalize this finding, we focus on a recent high pressure x-ray emission study of hexagonal ferrites in which the pressure dependence of orthorhombic $LuFeO_3$ is compared with h-$Lu_{0.5}Sc_{0.5}FeO_3$ [57]. The measurements uncover that the orthorhombic system undergoes a pressure-driven spin-crossover from a high to low ($S = 5/2 \rightarrow S = 1/2$) spin state at 50 GPa [57]. Conversely, the same type of transition is completely absent for h-$Lu_{0.5}Sc_{0.5}FeO_3$ demonstrating that the Fe remains in a trigonal bipyramidal environment up to at least 60 GPa (and very likely more according to theory) [57]. This study suggests that our search for symmetry in the high pressure phase in $Lu_{0.6}Sc_{0.4}FeO_3$ should exclude orthorhombic space groups. Work on compressively strained h-$LuFeO_3$ films allows us to further bolster our selection of the high pressure space group. Beyond revealing how pressure increases the K_3 order parameter amplitude, this study describes how the polarization of the hexagonal films is proportional to the amplitude of the K_3 order parameter [123]. Given that the $P6_3/mmc$ space group is centrosymmetric and that the K_3 mode is highly unstable within this structure, we can exclude it as a possible symmetry for the high pressure phase. Taken together, these studies strengthen our claim of a $P6_3cm \leftrightarrow P\bar{3}c1$ pressure-induced structural phase transition at 15 GPa in $Lu_{0.6}Sc_{0.4}FeO_3$.

To further explore mechanisms that stabilize the high-pressure phase of $Lu_{0.6}Sc_{0.4}FeO_3$, we make use of our first-principles calculations to compute the enthalpy difference between various structural phases as a function of pressure for the $LuFeO_3$ and $ScFeO_3$ end-member compounds. We find that for both materials, increasing pressure strongly stabilizes $Pbnm$, that is, the enthalpy difference between $Pbnm$ and $P6_3cm$ becomes more negative with increasing pressure. In contrast, the enthalpy difference between $P\bar{3}c1$ and $P6_3cm$ is positive and becomes slightly more positive as pressure increases.

This result clearly contrasts with our analysis of Fig. 6.4, where we find that $P\bar{3}c1$ shows the superior match between experimental and theoretical spectra in the high-pressure phase. We hypothesize that mixed Lu/Sc cations on the A-site in $Lu_{0.6}Sc_{0.4}FeO_3$ may play a key role in stabilizing the hexagonal structure up to high pressures. Our reasons for this conjecture are as follows. First, we note that the hexagonal structure is a metastable phase for the ferrites, and the mixed Lu/Sc cations on the A-site are known to enable synthesis of the hexagonal phase at ambient pressure [52]. We expect that this stabilizing influence of the mixed Lu/Sc on the hexagonal structure would persist under pressure.

Second, we note that the orthorhombic $Pbnm$ structure, which has been reported as the high pressure phase for manganites and indites with single A-site cations, has one crystallographically distinct A-site. In contrast, the hexagonal $P6_3cm$ and $P\bar{3}c1$ structures have two crystallographically distinct A-sites. Due to this idiosyncrasy, we expect that the hexagonal structures may more easily accommodate a mixture of A-site cations of different sizes. Analysis of A-O polyhedra in our DFT-relaxed $LuFeO_3$ structures reveals that the two distinct A-sites in $P6_3cm$ are fairly similar (in terms of polyhedral volume and bond lengths), whereas there is a bigger difference between the two A-sites in $P\bar{3}c1$. In particular, there is a distinction between the sites where the A-cation displaces up/down toward the adjacent iron oxide layer, and the sites where the A cation does not displace (see Fig. 6.2). The result is that in the first A-site there is a short (2.32 Å) bond between the A-cation and the planar oxygen it displaces towards, and a long (3.48 Å) bond between the A-cation and the layer it moves away from. In the second type of A-site, the bonds with the planar oxygens in the upper/lower layers are the same (2.90 Å). These different bonding environments may allow $P\bar{3}c1$ to more readily accommodate a mixture of A-site cations of different sizes. Based

on this discussion, we speculate that if the end-member hexagonal compounds $LuFeO_3$ and $ScFeO_3$ could be synthesized, then they would display a distinct pressure response compared to $Lu_{0.6}Sc_{0.4}FeO_3$: they would transition to $Pbnm$ in analogy with the manganites and indites.

Finally, comparison to temperature-dependent structural transitions in other hexagonal materials can provide additional insight, since temperature and pressure may access similar phases. Combined neutron scattering and theory work on $YMnO_3$ has shown that with increasing temperature it transitions from $P6_3cm$ to a phase where the phase Φ of the K_3 order parameter can take take on any value, and this value varies locally within the structure [114]. As another example, electron microscopy work on $InMnO_3$ has shown that it transitions from $P6_3cm$ to $P\bar{3}c1$ upon heating (which arises from a change in Φ by $\pi/6$), with a mesoscale coexistence of these two phases in an intermediate temperature regime [124]. Thus the impact of temperature appears to be modulate Φ, which controls the axis about which the bipyramids tilt, which suggests that this may also be tunable by other external parameters such as pressure.

Chapter 7

Real space infrared spectroscopy of ferroelectric domain walls in multiferroic h-(Lu,Sc)FeO_3

A-site substitution and compositional variation in the spectroscopic response

As a prelude to our near-field measurements of domain walls in h-$Lu_{0.6}Sc_{0.4}FeO_3$, we studied A-site substitution effects, the statistics of Lu and Sc occupation (best visualized as "red and blue balls" on 14 sites), and the impact of compositional heterogeneity on the spectroscopic response. By combining multiple techniques, we are able to place size constraints on the different compositional regions observed in h-$Lu_{0.6}Sc_{0.4}FeO_3$. This heterogeneity is a consequence of the local structure and depends on the relative abundance of Lu and Sc (henceforth, the Lu:Sc ratio). What we find is that the global and local Lu:Sc ratios are different. The crystal structure of h-$Lu_{0.6}Sc_{0.4}FeO_3$ is shown in Figure 7.1a. It consists of a layer of corner-sharing FeO_5 bipyramids between the hexagonal slabs containing the Lu and Sc centers. We initially performed traditional infrared microscopy in order to understand the size of these compositional regions. Even using a 20×20 μm^2 aperture - close to the resolution limit for this method due to the diffraction limit of light - these measurements reveal no obvious differences. We therefore conclude that composition varies across much

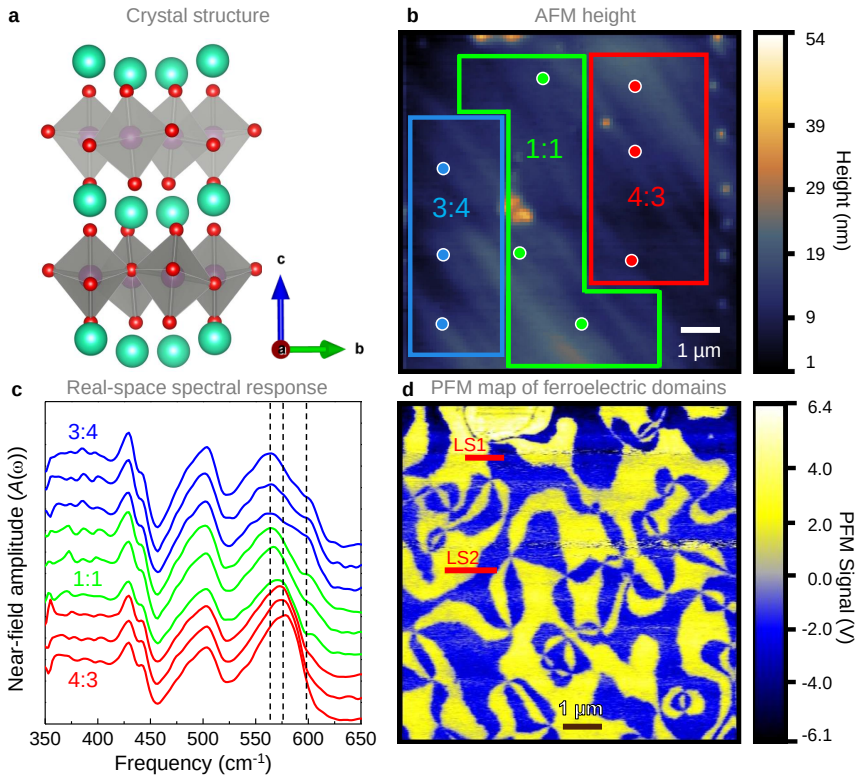

Figure 7.1: Overview of chemical and physical heterogeneity in h-$Lu_{0.6}Sc_{0.4}FeO_3$. (a) Crystal structure of the unit cell of h-$Lu_{0.6}Sc_{0.4}FeO_3$. The space group is $P6_3cm$. [52] Teal, purple and red spheres represent Lu/Sc sites, Fe atoms, and O atoms respectively. (b) Atomic force microscopy showing the topography of an area of interest with marks indicating the location of point spectra. (c) Point spectra corresponding to the locations indicated in (b). Curves are labeled and colored to match the different types of spectra observed in the various local composition areas. (d) Piezo-force microscopy of the ferroelectric vortex domains over the same area scanned in (b). Red lines show the positions of line scan 1 (LS1) and line scan 2 (LS2) taken in the 1:1 and 3:4 compositional regions, respectively.

smaller length scales. Subsequently, we clearly observe different spectral responses using near-field techniques. Here, the spatial resolution is many orders of magnitude smaller (20 nm) due to the tip-enhanced nature of the method. [125] By sampling different areas on the surface, we are also able to identify different compositional regions which are significantly larger than the tip (Figure 7.1b). We therefore conclude that the compositional domains in h-$Lu_{0.6}Sc_{0.4}FeO_3$ are smaller than what can be measured with a far field technique but also larger than the spatial resolution of a near-field point scan. Moreover, each region hosts a slightly different spectroscopic response (Figure 7.1c). This mapping process allows topography and position be correlated with composition. At the same time, we can estimate the size of these different areas. We find compositional variations over a 1 - 2 micron scale (Figure 7.1b).

As established above, the spectral differences observed on the micron scale are due to the natural compositional variation in the sample. Because h-$Lu_{0.6}Sc_{0.4}FeO_3$ is stabilized in the hexagonal phase (as confirmed by x-ray diffraction), we know that the Lu:Sc ratio has to be between 4:3 and 3:4. [52] This implies that there are three principle compositional variants: 4:3, 1:1, and 3:4. On its surface, this is a standard case of understanding how A-site substitution and chemical inhomogeneity appear in and stabilize h-$Lu_{0.6}Sc_{0.4}FeO_3$. The distinguishing aspect of our work is how we combine this analysis with infrared imaging of the ferroelectric domain walls, linking both chemical and physical heterogeneity.

Due to the Lu vs. Sc mass difference, the Sc-rich rich areas display features at slightly higher frequencies. This general expectation explains the variations in Figure 7.1b,c and is justified by a detailed comparison of mode frequencies in $LuFeO_3$ vs. $ScFeO_3$. As a result, we can assign Lu:Sc ratios based upon spectral shapes. Recall that there are three choices for crystals in the hexagonal phase: 4:3, 1:1, and 3:4. The spectra collected from the blue region in Figure 7.1b and plotted in Figure 7.1c displays the most prominent high frequency features. Specifically, the prominence of the peak at 600 cm^{-1}, which is primarily associated with oxygen displacements calculated for $ScFeO_3$, is the key signature of this region, and we attribute it to the highest local Sc concentration and a Lu:Sc ratio of 3:4. Likewise, the region in green has prominent features at higher frequency when compared to the red area, so we assign the local Lu:Sc ratios in these regions as 1:1 and 4:3, respectively. We

can therefore identify the local Lu:Sc ratio by subtle differences in the shape of the local near-field infrared response.

Vibrational mode assignments and lattice dynamics calculations

Figure 7.2 displays the absorption of h-$Lu_{0.6}Sc_{0.4}FeO_3$ measured by far field techniques, the synchrotron-based near-field infrared spectrum (both amplitude and phase), and the results of our complementary lattice dynamics calculations. We confine our attention to the region between 350 and 650 cm^{-1} where we have prominent features. Figure 7.2(c) shows representative phonon displacement patterns that occur near these frequencies. By inspecting displacement patterns, we find that phonons near 430 cm^{-1} have fairly complex patterns that combine bond stretching and bending. The mode at 428 cm^{-1} consists of primarily equatorial oxygen displacements, where within each bipyramid two oxygens displace down and the third displaces up by twice the amount (or two up, one down). This is somewhat reminiscent of the up-up-down A-site cation displacements found in these materials. The displacement patterns of phonons with frequencies near 510 cm^{-1} involve primarily bending of the Fe-O bonds, arising mainly from apical oxygen displacements. Finally, the phonons near 560 cm^{-1} consist mainly of Fe-O bond stretches. The vibrational modes that directly contain Lu and Sc motion as part of their displacement patterns resonate below 300 cm^{-1} - outside the range of the detector. On the other hand, the A site chemistry does provide indirect or "proximity effects" to the FeO_5-related stretching and bending modes as we discuss below. With the mode assignments of h-$Lu_{0.6}Sc_{0.4}FeO_3$ on a firm foundation, we are ready to image the ferroelectric domain walls.

Near-field infrared imaging of ferroelectric domain walls

Beyond spectral changes due to compositional heterogeneity, h-$Lu_{0.6}Sc_{0.4}FeO_3$ hosts polar domains with ferroelectric walls that separate these domains. The walls in this system are unusually fat - probably due to A-site substitution. While having polarization "up" or "down" (Figure 7.1d) does not create spectral contrast in and of itself, there is infrared contrast at the domain wall. This is because symmetry is broken at the wall since polarization

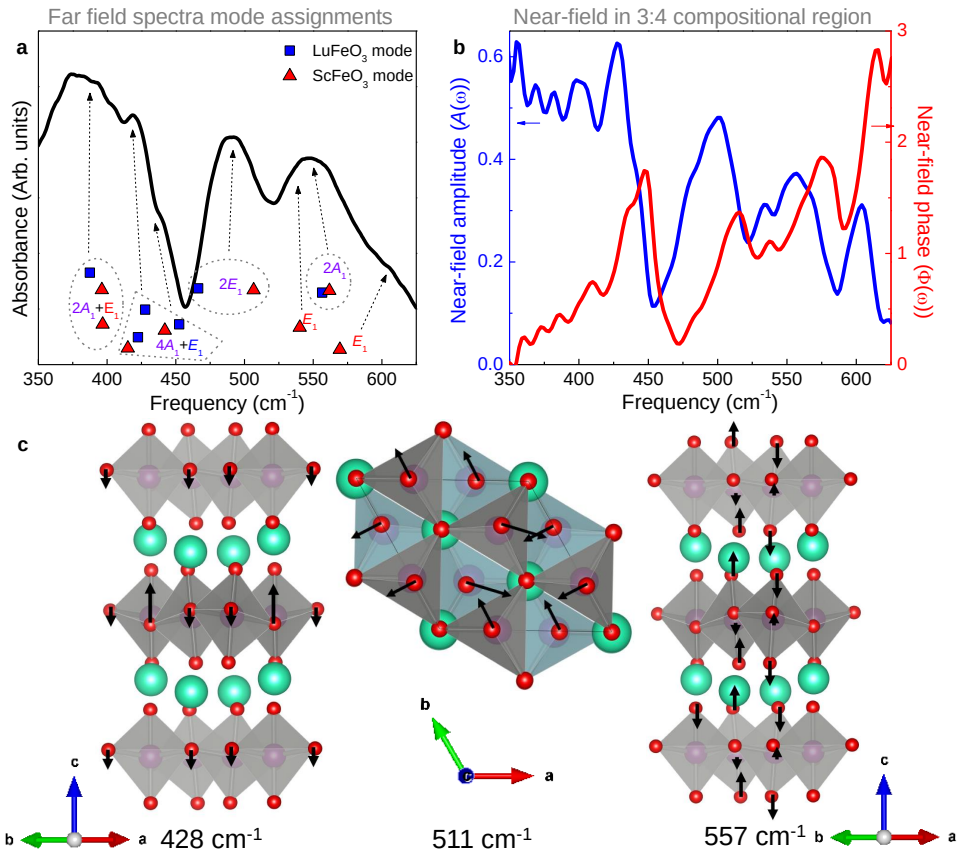

Figure 7.2: Comparison of far and near-field infrared spectra of h-$Lu_{0.6}Sc_{0.4}FeO_3$. (a) The far field infrared spectrum and (b) near-field amplitude and phase are in good agreement. We can assign the features of the near-field spectrum based upon our complementary lattice dynamics calculations. The theoretical modes are given by blue squares or red triangles for Lu- or Sc-containing modes, respectively. This figure focuses on the frequency range of the near-field response. (c) Three selected mode displacement patterns (at 428, 511 and 557 cm^{-1}, computed for $LuFeO_3$). Displacement patterns calculated for $ScFeO_3$ are the same but with slightly higher frequency.

either has to rotate (Néel wall) or turn off and on (Ising wall). Local compositional defects (such as oxygen deficiencies and perhaps the smaller Sc^{3+} ions) also tend to migrate to the walls. [126, 127] In any case, the walls that we seek to image are extremely small, so a far field measurement with a large beam will provide only an average response. [25] Tip-enhanced techniques are needed to (i) beat the diffraction limit and (ii) reveal the properties of individual walls.

We locate ferroelectric domain walls of interest in h-$Lu_{0.6}Sc_{0.4}FeO_3$ with a multi-step procedure. We begin by measuring atomic- and piezo-force microscopy on a flat area of a crystal according to the natural topography present in both fields of view. The results of this process are provided in Figure 7.1b,d. Navigation is made easier by proximity to gold markers. In order to re-position ourselves near specific domain walls at the beamline, we perform additional atomic force microscopy to map the surface in the same field of view as previously mapped with piezo-force microscopy. This assures proper positioning of the tip for a near-field line scan.

Figure 7.3 displays the real space infrared response of a ferroelectric domain wall in the 1:1 Lu:Sc compositional domain of h-$Lu_{0.6}Sc_{0.4}FeO_3$ along with fixed position and fixed frequency cuts of the image. There are three primary findings. First, the phononic signature of the domain wall has lower near-field amplitude when compared to the surrounding area. Second, the extent of the spectral response spans roughly 100 nm, indicating that local structural aspects of the wall as measured by infrared spectroscopy are anomalously wide. [128, 129, 130] Third, the walls are semiconducting rather than metallic as evidenced by the strong phonon response and lack of a Drude signature. This is different than the conducting AFM results in the literature, [131, 132, 133] although several of the more recent studies emphasize that the region of the domain wall is simply more conducting than the surroundings rather than metallic. [134, 135, 51, 136, 137, 138] We verify these findings by examining a ferroelectric domain wall in a different compositional region as described below.

Figure 7.4 summarizes the synchroton-based near-field infrared response of a different ferroelectric domain wall. This one is in the 3:4 Lu:Sc compositional domain, and again it includes the contour plot as well as fixed position and fixed frequency cuts of the image. Certain similarities are immediately apparent, although there are significant differences as

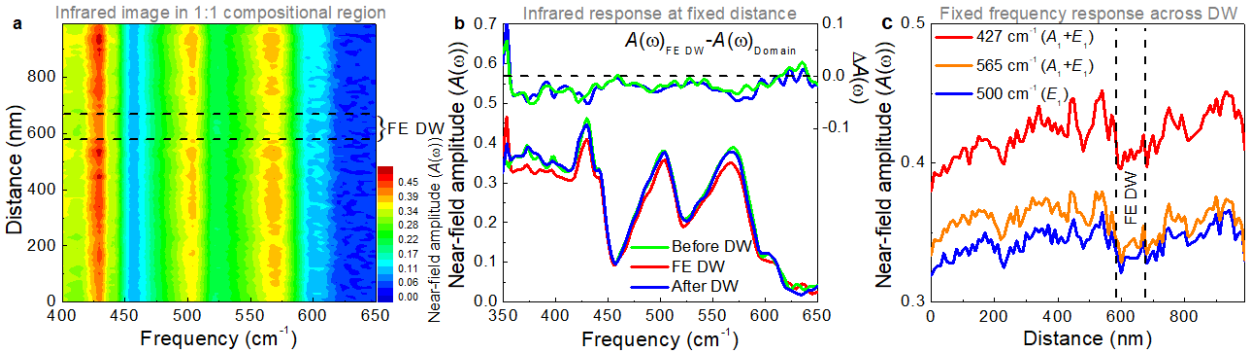

Figure 7.3: Near-field infrared response across a ferroelectric domain wall in h-$Lu_{0.6}Sc_{0.4}FeO_3$. (a) Color contour plot presents the near-field infrared response as a function of distance across a ferroelectric domain wall, indicated by the horizontal dashed lines, in the 1:1 Lu:Sc composition region. The image corresponds to line scan 1 in Figure 1d. The spatial resolution is 20×20 nm^2, and the spectrum is sampled every 10 nm along the line scan. The color indicates near-field amplitude as shown by the scale bar. (b) Constant distance curves, extracted from the real space infrared image in panel (a). Cuts are taken before, after, and at the ferroelectric domain wall. Difference spectra ($A(\omega)$ at the wall - $A(\omega)$ away from the wall) are shown at the top of this panel. (c) Fixed frequency cuts of the image in panel (a). These data reveal how the near-field amplitude evolves as a function of distance at the indicated frequencies which correspond to particular vibrational modes. The frequencies are selected to provide contrast at the ferroelectric domain wall in the 1:1 Lu:Sc compositional regime.

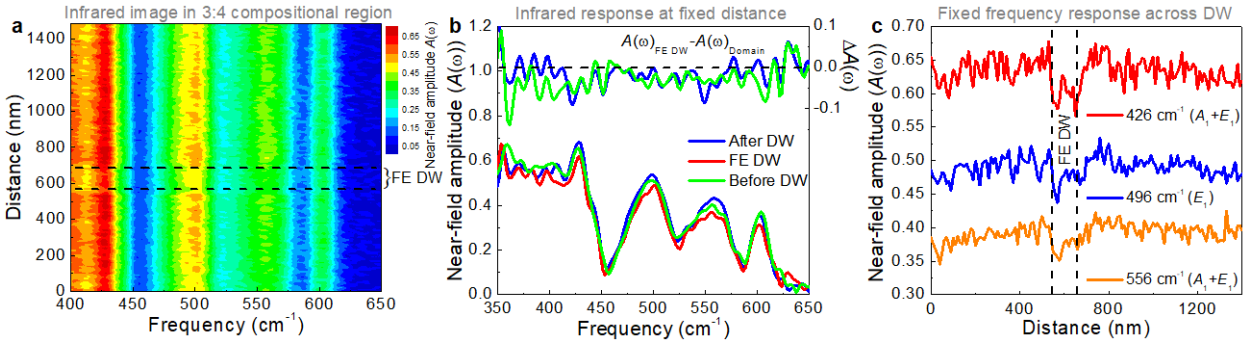

Figure 7.4: Near-field infrared response across a ferroelectric domain wall in h-$Lu_{0.6}Sc_{0.4}FeO_3$. (a) Color contour plot presents the near-field infrared response as a function of distance across a ferreoelectric domain wall, indicated by the horizontal dashed lines, in the 3:4 Lu:Sc composition region. The image corresponds to line scan 2 in Fig. 1(d). The spatial resolution is 20×20 nm^2, and the spectrum is sampled every 10 nm along the line scan. The color indicates near-field amplitude as shown by the scale bar. (b) Constant distance curves, extracted from the real space infrared image in panel (a). Cuts are taken before, after, and at the ferroelectric domain wall. Difference spectra ($A(\omega)$ at the wall - $A(\omega)$ away from the wall) are shown at the top of this panel. (c) Fixed frequency cuts of the image in panel (a). These data reveal how the near-field amplitude evolves as a function of distance at the indicated frequencies which correspond to particular vibrational modes. The frequencies are selected to provide contrast at the ferroelectric domain wall in the 3:4 Lu:Sc compositional region.

well. For instance, a line scan across the wall reveals clear phonons the entire time - an indication that the wall is insulating. The width of the wall in line scan 2 is slightly wider (120 nm) than in line scan 1, and again, we see diminished near-field amplitude at the wall. Because domain walls dissipate strain between domains, energy is minimized if the system is allowed to relax over a wider range. [69, 72] We attribute the width of the response to this relaxation. [26] This is different from the atomically thin walls reported previously. [128, 129, 130] We hypothesize that that Sc^{3+} (the small A site ion) and oxygen may be migrating to the defect, [139] thus creating larger distortions and broader structural relaxations.

Frequency shifts at the ferroelectric domain walls

In addition to amplitude and width changes, near-field infrared spectroscopy reveals that there are subtle frequency shifts of the phonon modes at the walls. While predicted in the past, [140, 141] experimental evidence has been lacking - even though we have been searching for these signatures for some time. Resolving these changes is quite challenging because the expected frequency shifts are small, and the resolution that we employ in the near-field line scans (8 cm^{-1}) is traditionally not very high. As a result, the frequency shifts that we find in h-$Lu_{0.6}Sc_{0.4}FeO_3$ are at the limit of our sensitivity. Even so, frequency shifts are observed in nearly all of the phonons - both bending and stretching modes. Figure 7.5 summarizes our findings.

Focusing first on the bending modes of h-$Lu_{0.6}Sc_{0.4}FeO_3$, we see that wall phonons are nearly identical to those in the nearby ferroelectric domains. For instance, none of the O–Fe–O bending modes shift at the wall in the 1:1 or 3:4 Lu:Sc composition regimes. The Fe–O stretching modes are more interesting. The response of the wall in the 3:4 Lu:Sc region is the most significant with frequency shifts on the order of -2.6, +3.2, and +0.9 cm^{-1} for the stretching modes near 498, 559, and 602 cm^{-1}, respectively. These are significant frequency shifts suggesting the possibility that the ferroelectric domain walls in the 3:4 Lu:Sc compositional region of h-$Lu_{0.6}Sc_{0.4}FeO_3$ may have a different internal structure than the surroundings - akin to the higher energy structure proposed by Kumagai and Spaldin in Ref. [142]. While these frequency shifts are not precise enough to tease out the intermediate

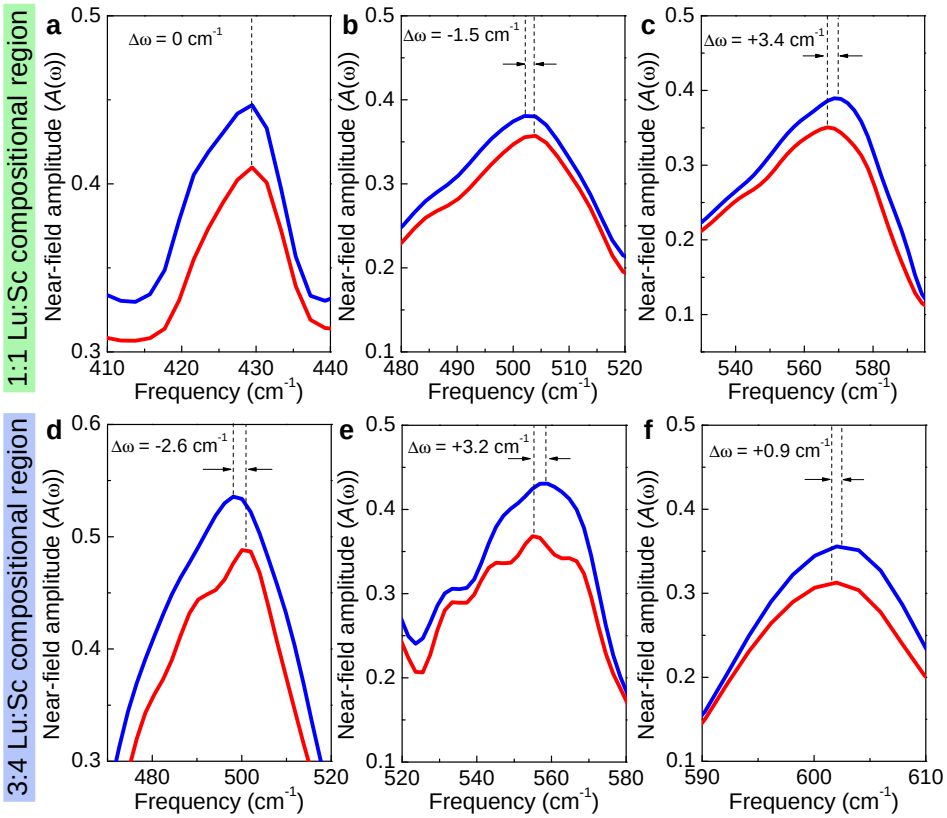

Figure 7.5: Close-up view of the frequency shifts at the ferroelectric domain walls. (a-c) Data are taken within the 1:1 Lu:Sc compositional region and (d-f) are taken from the 3:4 Lu:Sc compositional region. Data are taken at (red curves) and away from (blue curves) the domain wall to emphasize the frequency shifts associated with the wall.

space group inside the domain wall as we have done with h-$Lu_{0.6}Sc_{0.4}FeO_3$ under pressure, [28] they are consistent with the overall picture of using a structural modification to minimize strain across a relatively wide wall. Frequency shifts of the 504 and 568 cm^{-1} Fe–O stretching modes at the wall in the 1:1 Lu:Sc composition region are also significant at -1.5 and +3.4 cm^{-1}, respectively. If these frequency shifts could be augmented by near-field data at lower frequencies, it might be possible to compare calculations of the hexagonal, $P\bar{3}c1$, and $P6_3/mmc$ structures to see if predicted frequency shifts across the wall are consistent with our measurements. Such a comparison could, in principle, reveal the nature of an intermediate phase that might allow a wide domain wall to host a non-polar interior. Finally, we point out that based upon these frequency shifts, the force constants change by 1 or 2% at the wall. Both softening and hardening is observed.

Chapter 8

Summary and outlook

Work in this dissertation focuses on the properties of new types of ferroelectrics using synchrotron-based spectroscopy. These exotic ferroelectrics display unique properties as a result of competing phases, making them highly tunable components ideal for device application. Spatially resolved near-field infrared spectroscopy is an excellent tool to reveal the fundamental properties of domain walls present in these materials. The understanding enables new technologies that incorporate domain walls as functional elements. High pressure infrared spectroscopy is a powerful technique to investigate the mechanisms responsible for structural phase transitions in complex oxides. These efforts are key to understanding how the ferroelectric order parameters respond under pressure and develop structure-property relationships to broadly establish common symmetry progressions under pressure for modern ferroelectric materials.

My earliest works focuses on the nano-scale properties of domain walls in the hybrid improper ferroelectric $Ca_3Ti_2O_7$ utilizing near-field infrared nanospectroscopy combined with theoretical models of ferroelastic domain walls. The commonly held notion about domain walls being purely atomically thin interfaces is rejected, as we observe domain walls with ≈100 nm widths. Moreover, the observation of phonons at the domain wall with a slight blue shift, is another surprising result which indicates that the walls remain insulting. While theoretical calculations reveal a small reduction of the band gap indicating a slightly improved conductivity, the walls are not metallic as previously posited. Understanding the

nanoscale heterogeneity present in ferroics is key to the development of new technologies that incorporate domain walls as functional objects, such as racetrack memory [29].

A subsequent project on a related n=2 member of the Ruddlesden-Popper series, $Sr_3Sn_2O_7$, reveals a series of pressure induced structural phase transitions that mirror those observed at high temperature. This system is unique in that it displays one of the lowest coercive fields among related compounds, indicating that it is easily switchable. As a hybrid improper ferroelectric, the order parameters that drive its ferroelectricity are geometric distortions. It is well known that pressure modifies the crystal structure by modulating bond lengths and angles, and as such, pressure is a perfect tuning parameter to trigger structural phase transitions in this class of materials. By comparing our results with other studies on hybrid improper ferroelectrics, we develop a set of structure-property relations broadly applicable to n=2 members of the Ruddlesden-Popper series. This advancement is crucial for the improvement of strain-driven capabilities in these materials, circumventing the need for ultra-high temperatures to access structural phases of interest.

Continuing with the theme of high pressure phases in oxides, we reveal a pressure-induced polar to antipolar structural phase transition from $P6_3cm \leftrightarrow P\bar{3}c1$ in the hexagonal rare earth ferrite h-$Lu_{0.6}Sc_{0.4}FeO_3$ using synchtrotron-based high pressure infrared spectroscopy. This material is unique in that the hexagonal structure is stabilized by A-site substitution in a single crystal. As such, the modulation of the bipyramidal tilting modes in this improper ferroelectric are responsible for establishing the antipolar state. By comparing our spectral data with theoretically calculated vibrational properties for candidate high pressure phases, we solidify our experimental findings that identify the high pressure antipolar phase and contrast our observations with high pressure studies on the manganites revealing that these two classes of improper ferroelectric prefer different structural phase sequences under compression. The progression of these structural phase transitions is essential for bringing together multiple functional components in a single phase to achieve combined functionality in novel devices.

Extending our work on the fundamental properties of domain walls we probe ferroelectric walls in h-$Lu_{0.6}Sc_{0.4}FeO_3$. Here we reveal how the A-site substitution impacts the local stoichiometry and report characteristic length scales for chemical heterogeneity on the order

of 1-3 μm, a finding essential for developing new substituted systems. Additionally, we observe frequency shifts in phonons present at the domain boundary which suggest that an intermediate phase may be present at the domain wall, in line with previous predictions of domain wall structure [142]. This result marks a significant advancement, as phonons are predicted to display frequency shifts at the wall, but our prior work only revealed a slight shift at the edge of the sensitivity.

Taken together, these findings demonstrate the capabilities of synchrotron-based infrared spectroscopy and its application to understand the fundamental properties of the ferroelectric mechanisms in complex oxides. Understanding the fundamental properties of domain walls is key for the development of ultra-low power devices, highly compact memory, and logic devices. The demonstration of the effects of external stimuli on new types of ferroelectrics is paramount for the development future materials. Furthermore, these studies also motivate future collaborative efforts to probe pressure-induced structural phase transitions using both high pressure x-ray and infrared techniques as both are accessible at a synchrotron facility and provide complimentary results. Demonstrating how the different classes of ferroelectrics evolve under compression advances the capability to engineer new materials utilizing strain as a tuning parameter to stabilize desired structures at room temperature.

Bibliography

[1] D. Meyerhofer, "Transition to the ferroelectric state in barium titanate," *Physical Review*, vol. 112, pp. 413–423, oct 1958. 1

[2] D. B. Litvin, "Ferroelectric space groups," *Acta Crystallographica Section A Foundations of Crystallography*, vol. 42, pp. 44–47, jan 1986. 1

[3] T. Tanaka, "Barium titanate ceramics and their applications," *Bulletin of the Institute for Chemical Research, Kyoto University*, vol. 32, 3 1954. 2

[4] Y. Zhang, H.-Y. Ye, D.-W. Fu, and R.-G. Xiong, "An order-disorder ferroelectric host-guest inclusion compound," *Angewandte Chemie*, vol. 126, pp. 2146–2150, feb 2014. 2

[5] V. G. BHIDE, M. S. HEGDE, and K. G. DESHMUKH, "Ferroelectric properties of lead titanate," *Journal of the American Ceramic Society*, vol. 51, pp. 565–568, oct 1968. ix, 3

[6] R. S. Cudney, J. Fousek, M. Zgonik, P. Günter, M. H. Garrett, and D. Rytz, "Photorefractive and domain gratings in barium titanate," *Applied Physics Letters*, vol. 63, pp. 3399–3401, dec 1993. ix, 3

[7] B. B. Van Aken, T. T. Palstra, A. Filippetti, and N. A. Spaldin, "The origin of ferroelectricity in magnetoelectric $YMnO_3$," *Nature Materials*, vol. 3, pp. 164–170, mar 2004. ix, 3

[8] J. Wang, J. B. Neaton, H. Zheng, V. Nagarajan, S. B. Ogale, B. Liu, D. Viehland, V. Vaithyanathan, D. G. Schlom, U. V. Waghmare, N. A. Spaldin, K. M. Rabe, M. Wuttig, and R. Ramesh, "Epitaxial $BiFeO_3$ multiferroic thin film heterostructures," *Science*, vol. 299, pp. 1719–1722, mar 2003. ix, 3, 24

[9] T. Aoyama, K. Yamauchi, A. Iyama, S. Picozzi, K. Shimizu, and T. Kimura, "Giant spin-driven ferroelectric polarization in $TbMnO_3$ under high pressure," *Nature Communications*, vol. 5, p. 4927, dec 2014. ix, xi, 3, 5, 7, 26, 34

[10] A. Clune, N. Harms, K. R. O'Neal, K. Hughey, K. A. Smith, D. Obeysekera, J. Haddock, N. S. Dalal, J. Yang, Z. Liu, and J. L. Musfeldt, "Developing the pressure–temperature–magnetic field phase diagram of multiferroic $[(CH_3)_2NH_2]Mn(HCOO)_3$," *Inorganic Chemistry*, vol. 59, pp. 10083–10090, jul 2020. ix, xii, 3, 31, 39, 80

[11] M. S. Senn, A. Bombardi, C. A. Murray, C. Vecchini, A. Scherillo, X. Luo, and S. W. Cheong, "Negative thermal expansion in hybrid improper ferroelectric Ruddlesden-Popper perovskites by symmetry trapping," *Physical Review Letters*, vol. 114, p. 035701, jan 2015. ix, 3, 67, 78

[12] Y. Wang, H. Zhao, L. Zhang, Z. Liu, J. Chen, J. Deng, J. Wang, K. Ibrahim, N. I. Ilinykh, and X. Xing, "Well-saturated ferroelectric polarization in $PbTiO_3$ –$SmFeO_3$ thin films," *Inorganic Chemistry Frontiers*, vol. 3, no. 11, pp. 1473–1479, 2016. x, 4

[13] Y. Wang, H. Zhao, L. Zhang, J. Chen, and X. Xing, "$PbTiO_3$ -based perovskite ferroelectric and multiferroic thin films," *Physical Chemistry Chemical Physics*, vol. 19, no. 27, pp. 17493–17515, 2017. x, 4

[14] M. Fiebig, T. Lottermoser, D. Meier, and M. Trassin, "The evolution of multiferroics," *Nature Reviews Materials*, vol. 1, p. 16046, aug 2016. x, 13, 23, 24

[15] A. Malashevich and D. Vanderbilt, "First principles study of improper ferroelectricity in $TbMnO_3$," *Physical Review Letters*, vol. 101, p. 037210, jul 2008. 2, 5

[16] C. J. Fennie and K. M. Rabe, "Ferroelectric transition in $YMnO_3$ from first principles," *Physical Review B*, vol. 72, p. 100103, sep 2005. 5

[17] M. Lilienblum, T. Lottermoser, S. Manz, S. M. Selbach, A. Cano, and M. Fiebig, "Ferroelectricity in the multiferroic hexagonal manganites," *Nature Physics*, vol. 11, pp. 1070–1073, dec 2015. 5

[18] T. Kimura, "Spiral magnets as magnetoelectrics," *Annual Review of Materials Research*, vol. 37, pp. 387–413, aug 2007. x, 5, 15

[19] M. Li, H. Tan, and W. Duan, "Hexagonal rare-earth manganites and ferrites: a review of improper ferroelectricity, magnetoelectric coupling, and unusual domain walls," *Physical Chemistry Chemical Physics*, vol. 22, no. 26, pp. 14415–14432, 2020. x, 14

[20] B. V. Beznosikov and K. S. Aleksandrov, "Perovskite-like crystals of the Ruddlesden-Popper series," *Crystallography Reports*, vol. 45, pp. 792–798, sep 2000. 6

[21] N. A. Benedek and C. J. Fennie, "Hybrid improper ferroelectricity: a mechanism for controllable polarization-magnetization coupling," *Physical Review Letters*, vol. 106, p. 107204, mar 2011. x, 6, 9, 16

[22] Y. S. Oh, X. Luo, F.-T. Huang, Y. Wang, and S.-W. Cheong, "Experimental demonstration of hybrid improper ferroelectricity and the presence of abundant charged walls in $(Ca,Sr)_3Ti_2O_7$ crystals," *Nature Materials*, vol. 14, pp. 407–413, apr 2015. xi, 17, 18, 29, 30, 51, 74

[23] A. G. Gavriliuk, V. V. Struzhkin, I. S. Lyubutin, S. G. Ovchinnikov, M. Y. Hu, and P. Chow, "Another mechanism for the insulator-metal transition observed in Mott insulators," *Physical Review B*, vol. 77, p. 155112, apr 2008. 7, 26

[24] H. A. Bechtel, E. A. Muller, R. L. Olmon, M. C. Martin, and M. B. Raschke, "Ultrabroadband infrared nanospectroscopic imaging," *Proceedings of the National Academy of Sciences*, vol. 111, pp. 7191–7196, may 2014. xi, xiii, 19, 52

[25] Q.-C. Sun, X. Xi, X. Wang, N. Lee, D. Mazumdar, R. J. Smith, G. L. Carr, S.-W. Cheong, and J. L. Musfeldt, "Spectroscopic signatures of domain walls in hexagonal $ErMnO_3$," *Physical Review B*, vol. 90, p. 121303, sep 2014. xi, 8, 20, 28, 119

[26] K. A. Smith, E. A. Nowadnick, S. Fan, O. Khatib, S. J. Lim, B. Gao, N. C. Harms, S. N. Neal, J. K. Kirkland, M. C. Martin, C. J. Won, M. B. Raschke, S.-W. Cheong, C. J. Fennie, G. L. Carr, H. A. Bechtel, and J. L. Musfeldt, "Infrared nanospectroscopy of ferroelastic domain walls in hybrid improper ferroelectric $Ca_3Ti_2O_7$," *Nature Communications*, vol. 10, p. 5235, dec 2019. xiv, xv, xvi, xvii, 10, 11, 12, 68, 70, 75, 77, 122

[27] K. A. Smith, S. P. Ramkumar, N. C. Harms, A. J. Clune, X. Xu, S.-W. Cheong, Z. Liu, E. A. Nowadnick, and J. L. Musfeldt, "Revealing pressure-driven structural transitions in the hybrid improper ferroelectric $Sr_3Sn_2O_7$," *Physical Review B*, vol. 104, p. 064106, aug 2021. xvii, xviii, xix, 10, 12, 81, 84, 85, 86, 88, 90, 91, 93, 98

[28] K. A. Smith, S. P. Ramkumar, N. C. Harms, A. J. Clune, S.-W. Cheong, Z. Liu, E. A. Nowadnick, and J. L. Musfeldt, "Pressure-induced phase transition and phonon softening in h-$Lu_{0.6}Sc_{0.4}FeO_3$," *Physical Review B*, vol. 104, p. 094109, sep 2021. ix, xx, xxi, 11, 12, 101, 102, 103, 104, 105, 108, 110, 124

[29] S. S. P. Parkin, M. Hayashi, and L. Thomas, "Magnetic domain-wall racetrack memory," *Science*, vol. 320, pp. 190–194, apr 2008. 12, 29, 126

[30] K. M. Rabe, M. Dawber, C. Lichtensteiger, C. H. Ahn, and J.-M. Triscone, "Modern physics of ferroelectrics: essential background," in *Physics of Ferroelectrics*, pp. 1–30, Berlin, Heidelberg: Springer Berlin Heidelberg. 22, 27

[31] A. Mante and J. Volger, "The thermal conductivity of batio$_3$ in the neighbourhood of its ferroelectric transition temperatures," *Physics Letters A*, vol. 24, pp. 139–140, 1 1967. 22

[32] A. Sani, M. Hanfland, and D. Levy, "Pressure and temperature dependence of the ferroelectric–paraelectric phase transition in $PbTiO_3$," *Journal of Solid State Chemistry*, vol. 167, pp. 446–452, sep 2002. 22, 23

[33] I. A. Kornev, L. Bellaiche, P. Bouvier, P.-E. Janolin, B. Dkhil, and J. Kreisel, "Ferroelectricity of perovskites under pressure," *Physical Review Letters*, vol. 95, p. 196804, oct 2005. 23

[34] J.-M. Hu and C.-W. Nan, "Opportunities and challenges for magnetoelectric devices," *APL Materials*, vol. 7, p. 080905, aug 2019. 23

[35] D. ASTROV, "Magnetoelectric effect in chromium oxide," *SOVIET PHYSICS JETP*, vol. 13, no. 4, 1961. 23

[36] M. Fiebig, "Revival of the magnetoelectric effect," *Journal of Physics D: Applied Physics*, vol. 38, pp. R123–R152, apr 2005. 23

[37] B. B. Van Aken, J.-P. Rivera, H. Schmid, and M. Fiebig, "Observation of ferrotoroidic domains," *Nature*, vol. 449, pp. 702–705, oct 2007. xi, 25

[38] T. Kimura, G. Lawes, T. Goto, Y. Tokura, and A. P. Ramirez, "Magnetoelectric phase diagrams of orthorhombic RMnO3(R=Gd, Tb, and Dy)," *Physical Review B*, vol. 71, p. 224425, jun 2005. xi, 26, 33

[39] W. Prellier, M. P. Singh, and P. Murugavel, "The single-phase multiferroic oxides: from bulk to thin film," *Journal of Physics: Condensed Matter*, vol. 17, pp. R803–R832, aug 2005. xi, 33

[40] N. A. Hill and K. M. Rabe, "First-principles investigation of ferromagnetism and ferroelectricity in bismuth manganite," *Physical Review B*, vol. 59, pp. 8759–8769, apr 1999. 24

[41] R. Seshadri and N. A. Hill, "Visualizing the role of bi 6s "lone pairs" in the off-center distortion in ferromagnetic $bimno_3$," *Chemistry of Materials*, vol. 13, pp. 2892–2899, 9 2001. 24

[42] D. P. Kozlenko, S. E. Kichanov, S. Lee, J. G. Park, V. P. Glazkov, and B. N. Savenko, "High-pressure effect on the crystal and magnetic structures of the frustrated antiferromagnet $YMnO_3$," *Journal of Experimental and Theoretical Physics Letters*, vol. 82, pp. 193–197, aug 2005. 27

[43] E. Bousquet, M. Dawber, N. Stucki, C. Lichtensteiger, P. Hermet, S. Gariglio, J.-M. Triscone, and P. Ghosez, "Improper ferroelectricity in perovskite oxide artificial superlattices," *Nature*, vol. 452, pp. 732–736, apr 2008. 27

[44] H. Zhang, K. Haule, and D. Vanderbilt, "Effective J=1/2 insulating state in Ruddlesden-Popper iridates: an LDA + DMFT study," *Physical Review Letters*, vol. 111, p. 246402, dec 2013. 27

[45] N. A. Benedek, J. M. Rondinelli, H. Djani, P. Ghosez, and P. Lightfoot, "Understanding ferroelectricity in layered perovskites: new ideas and insights from theory and experiments," *Dalton Transactions*, vol. 44, no. 23, pp. 10543–10558, 2015. 27

[46] E. A. Nowadnick and C. J. Fennie, "Domains and ferroelectric switching pathways in $Ca_3Ti_2O_7$ from first principles," *Physical Review B*, vol. 94, p. 104105, sep 2016. 28, 67, 83, 89

[47] D. Meier, "Functional domain walls in multiferroics," *Journal of Physics: Condensed Matter*, vol. 27, p. 463003, 11 2015. xi, 28, 35

[48] F. Ajejas, V. Křižáková, D. de Souza Chaves, J. Vogel, P. Perna, R. Guerrero, A. Gudin, J. Camarero, and S. Pizzini, "Tuning domain wall velocity with Dzyaloshinskii-Moriya interaction," *Applied Physics Letters*, vol. 111, p. 202402, nov 2017. 29

[49] D. Lee, R. K. Behera, P. Wu, H. Xu, Y. L. Li, S. B. Sinnott, S. R. Phillpot, L. Q. Chen, and V. Gopalan, "Mixed Bloch-Néel-Ising character of 180° ferroelectric domain walls," *Physical Review B*, vol. 80, p. 060102, aug 2009. xi, 35

[50] X. Xu, Y. Wang, F. Huang, K. Du, E. A. Nowadnick, and S. Cheong, "Highly tunable ferroelectricity in hybrid improper ferroelectric $Sr_3Sn_2O_7$," *Advanced Functional Materials*, vol. 30, p. 2003623, oct 2020. xii, 29, 36, 51

[51] X. Wu, K. Du, L. Zheng, D. Wu, S.-W. Cheong, and K. Lai, "Microwave conductivity of ferroelectric domains and domain walls in a hexagonal rare-earth ferrite," *Physical Review B*, vol. 98, p. 081409, aug 2018. 30, 119

[52] K. Du, B. Gao, Y. Wang, X. Xu, J. Kim, R. Hu, F.-T. Huang, and S.-W. Cheong, "Vortex ferroelectric domains, large-loop weak ferromagnetic domains, and their decoupling in hexagonal (Lu, Sc)FeO_3," *npj Quantum Materials*, vol. 3, p. 33, dec 2018. xii, xxii, 30, 37, 38, 51, 112, 115, 116

[53] L. Lin, H. M. Zhang, M. F. Liu, S. Shen, S. Zhou, D. Li, X. Wang, Z. B. Yan, Z. D. Zhang, J. Zhao, S. Dong, and J.-M. Liu, "Hexagonal phase stabilization and magnetic

orders of multiferroic $Lu_{1-x}Sc_xFeO_3$," *Physical Review B*, vol. 93, p. 075146, feb 2016. 30

[54] S. G. Jabarov, D. P. Kozlenko, S. E. Kichanov, A. V. Belushkin, B. N. Savenko, R. Z. Mextieva, and C. Lathe, "High-pressure effect on the ferroelectric-paraelectric transition in $PbTiO_3$," *Physics of the Solid State*, vol. 53, pp. 2300–2304, nov 2011. 31

[55] D. P. Kozlenko, A. A. Belik, A. V. Belushkin, E. V. Lukin, W. G. Marshall, B. N. Savenko, and E. Takayama-Muromachi, "Antipolar phase in multiferroic $BiFeO_3$ at high pressure," *Physical Review B*, vol. 84, p. 094108, sep 2011. 31

[56] F. Ye, J. Wang, J. Sheng, C. Hoffmann, T. Gu, H. J. Xiang, W. Tian, J. J. Molaison, A. M. dos Santos, M. Matsuda, B. C. Chakoumakos, J. A. Fernandez-Baca, X. Tong, B. Gao, J. W. Kim, and S.-W. Cheong, "Soft antiphase tilt of oxygen octahedra in the hybrid improper multiferroic $Ca_3Mn_{1.9}Ti_{0.1}O_7$," *Physical Review B*, vol. 97, p. 041112, jan 2018. xii, 31, 40, 92

[57] T. Wen, Y. Wang, C. Li, D. Jiang, Z. Jiang, S. Qu, W. Yang, and Y. Wang, "Site-specific pressure-driven spin-crossover in Lu_{1-x} Sc_xFeO_3," *The Journal of Physical Chemistry Letters*, vol. 11, pp. 8549–8553, oct 2020. xii, 32, 41, 111

[58] F. N. D. Kurie, "Present-day design and technique of the cyclotron: a description of the methods and application of the cyclotron as developed by Ernest O. Lawrence and his associates at the Radiation Laboratory, Berkeley," *Journal of Applied Physics*, vol. 9, pp. 691–701, nov 1938. 47

[59] H. Wiedemann, *Particle Accelerator Physics*. Advanced Texts in Physics, Berlin, Heidelberg: Springer Berlin Heidelberg, 2003. 47

[60] H. K. Mao, J. Xu, and P. M. Bell, "Calibration of the ruby pressure gauge to 800 kbar under quasi-hydrostatic conditions," *Journal of Geophysical Research*, vol. 91, no. B5, p. 4673, 1986. 49, 50, 62

[61] P. Wang, D. He, C. Xu, X. Ren, L. Lei, S. Wang, F. Peng, X. Yan, D. Liu, Q. Wang, L. Xiong, and J. Liu, "High-pressure x-ray diffraction study of YBO_3 /Eu^{3+} , $GdBO_3$,

and $EuBO_3$: pressure-induced amorphization in $GdBO_3$," *Journal of Applied Physics*, vol. 115, p. 043507, jan 2014. 62

[62] P. Hohenberg and W. Kohn, "Inhomogeneous electron gas," *Physical Review*, vol. 136, pp. B864–B871, nov 1964. 64

[63] P. E. Blöchl, "Projector augmented-wave method," *Physical Review B*, vol. 50, pp. 17953–17979, dec 1994. 64

[64] G. Kresse and J. Furthmüller, "Efficient iterative schemes for ab initio total-energy calculations using a plane-wave basis set," *Physical Review B*, vol. 54, pp. 11169–11186, oct 1996. 64

[65] J. P. Perdew, A. Ruzsinszky, G. I. Csonka, O. A. Vydrov, G. E. Scuseria, L. A. Constantin, X. Zhou, and K. Burke, "Restoring the density-gradient expansion for exchange in solids and surfaces," *Physical Review Letters*, vol. 100, p. 136406, apr 2008. 64

[66] K. Momma and F. Izumi, "VESTA 3 for three-dimensional visualization of crystal, volumetric and morphology data," *Journal of Applied Crystallography*, vol. 44, pp. 1272–1276, dec 2011. 64

[67] M. M. Elcombe, E. H. Kisi, K. D. Hawkins, T. J. White, P. Goodman, and S. Matheson, "Structure determinations for $Ca_3Ti_2O_7$, $Ca_4Ti_3O_10$, $Ca_3.6Sr_0.4Ti_3O_10$ and a refinement of $Sr_3Ti_2O_7$," *Acta Crystallographica Section B Structural Science*, vol. 47, pp. 305–314, jun 1991. 67

[68] A. M. Glazer, "The classification of tilted octahedra in perovskites," *Acta Crystallographica Section B Structural Crystallography and Crystal Chemistry*, vol. 28, pp. 3384–3392, nov 1972. 67

[69] A. K. Tagantsev, L. E. Cross, and J. Fousek, *Domains in ferroic crystals and thin films*. New York, NY: Springer New York, 2010. 67, 73, 78, 122

[70] W. Cao and G. R. Barsch, "Landau-Ginzburg model of interphase boundaries in improper ferroelastic Perovskites of D_{4h}^{18} symmetry," *Physical Review B*, vol. 41, pp. 4334–4348, mar 1990. 73, 78

[71] J. G. Cherian, T. Birol, N. C. Harms, B. Gao, S.-W. Cheong, D. Vanderbilt, and J. L. Musfeldt, "Optical spectroscopy and band gap analysis of hybrid improper ferroelectric $Ca_3Ti_2O_7$," *Applied Physics Letters*, vol. 108, p. 262901, jun 2016. 73

[72] P. V. Yudin, M. Y. Gureev, T. Sluka, A. K. Tagantsev, and N. Setter, "Anomalously thick domain walls in ferroelectrics," *Physical Review B*, vol. 91, p. 060102, feb 2015. 74, 122

[73] E. K. Salje, "Ferroelastic materials," *Annual Review of Materials Research*, vol. 42, pp. 265–283, aug 2012. 78

[74] A. Schiaffino and M. Stengel, "Macroscopic polarization from antiferrodistortive cycloids in ferroelastic $SrTiO_3$," *Physical Review Letters*, vol. 119, p. 137601, sep 2017. 78

[75] F. Xue, Y. Gu, L. Liang, Y. Wang, and L.-Q. Chen, "Orientations of low-energy domain walls in perovskites with oxygen octahedral tilts," *Physical Review B*, vol. 90, p. 220101, dec 2014. 78

[76] W. Cao, G. R. Barsch, and J. A. Krumhansl, "Quasi-one-dimensional solutions for domain walls and their constraints in improper ferroelastics," *Physical Review B*, vol. 42, pp. 6396–6401, oct 1990. 78

[77] X.-Z. Lu and J. M. Rondinelli, "Epitaxial-strain-induced polar-to-nonpolar transitions in layered oxides," *Nature Materials*, vol. 15, pp. 951–955, sep 2016. 78

[78] K. Kim, S. Y. Lim, J.-U. Lee, S. Lee, T. Y. Kim, K. Park, G. S. Jeon, C.-H. Park, J.-G. Park, and H. Cheong, "Suppression of magnetic ordering in XXZ-type antiferromagnetic monolayer $NiPS_3$," *Nature Communications*, vol. 10, p. 345, dec 2019. 80

[79] H.-H. Kung, R. E. Baumbach, E. D. Bauer, V. K. Thorsmolle, W.-L. Zhang, K. Haule, J. A. Mydosh, and G. Blumberg, "Chirality density wave of the "hidden order" phase in URu_2Si_2," *Science*, vol. 347, pp. 1339–1342, mar 2015. 80

[80] D. V. S. Muthu, P. Teredesai, S. Saha, Suchitra, U. V. Waghmare, A. K. Sood, and C. N. R. Rao, "Pressure-induced structural phase transitions and phonon anomalies in ReO_3: Raman and first-principles study," *Physical Review B*, vol. 91, p. 224308, jun 2015. 80

[81] S. Yoshida, H. Akamatsu, R. Tsuji, O. Hernandez, H. Padmanabhan, A. Sen Gupta, A. S. Gibbs, K. Mibu, S. Murai, J. M. Rondinelli, V. Gopalan, K. Tanaka, and K. Fujita, "Hybrid improper ferroelectricity in $(Sr,Ca)_3Sn_2O_7$ and beyond: universal relationship between ferroelectric transition temperature and tolerance factor in n = 2 Ruddlesden–Popper phases," *Journal of the American Chemical Society*, vol. 140, pp. 15690–15700, nov 2018. ix, xviii, 83, 84, 87, 92, 94, 95, 97

[82] S. Yoshida, K. Fujita, H. Akamatsu, O. Hernandez, A. Sen Gupta, F. G. Brown, H. Padmanabhan, A. S. Gibbs, T. Kuge, R. Tsuji, S. Murai, J. M. Rondinelli, V. Gopalan, and K. Tanaka, "Ferroelectric $Sr_3Zr_2O_7$: competition between hybrid improper ferroelectric and antiferroelectric mechanisms," *Advanced Functional Materials*, vol. 28, p. 1801856, jul 2018. ix, xix, 83, 87, 94, 95, 98

[83] R. G. Amorim, M. Veríssimo-Alves, and J. P. Rino, "Energetics of phase transitions in BaO through DFT calculations with norm-conserving pseudopotentials: LDA vs. GGA results," *Computational Materials Science*, vol. 37, pp. 349–354, sep 2006. 87

[84] S. Ehsan, A. Tröster, F. Tran, and P. Blaha, "DFT study of the electronic properties and the cubic to tetragonal phase transition in $RbCaF_3$," *Physical Review Materials*, vol. 2, p. 093610, sep 2018. 87

[85] S. Javaid and M. Javed Akhtar, "Pressure-induced magnetic, structural, and electronic phase transitions in $LaFeO_3$: a density functional theory (generalized gradient approximation) + U study," *Journal of Applied Physics*, vol. 116, p. 023704, jul 2014. 87

[86] J. Kaczkowski, "First-principles study of structural, electronic, ferroelectric, and vibrational properties of $BiInO_3$ under high pressure," *Journal of Physics and Chemistry of Solids*, vol. 134, pp. 225–237, nov 2019. 87

[87] J. J. Lu, X. Q. Liu, X. Ma, M. S. Fu, A. Yuan, Y. J. Wu, and X. M. Chen, "Crystal structures, dielectric properties, and phase transition in hybrid improper ferroelectric $Sr_3Sn_2O_7$-based ceramics," *Journal of Applied Physics*, vol. 125, p. 044101, jan 2019. 87

[88] X. Sun, X. Yang, C. Xu, X. Gan, W. Zhang, Z. Gao, H.-L. Cai, and X. Wu, "Effects of Ba doping on the phase transition of $Sr_3Sn_2O_7$," *Chemical Physics Letters*, vol. 728, pp. 74–79, aug 2019. 87, 97

[89] W. Cochran, "Crystal stability and the theory of ferroelectricity," *Advances in Physics*, vol. 9, pp. 387–423, oct 1960. 89

[90] W. Cochran, "Crystal stability and the theory of ferroelectricity part II. Piezoelectric crystals," *Advances in Physics*, vol. 10, pp. 401–420, oct 1961. 89

[91] P. Peercy, ""Soft" mode and coupled modes in the ferroelectric phase of KDP," *Solid State Communications*, vol. 16, pp. 439–442, feb 1975. 89

[92] T. Marqueño, D. Errandonea, J. Pellicer-Porres, D. Martinez-Garcia, D. Santamaria-Pérez, A. Muñoz, P. Rodríguez-Hernández, A. Mujica, S. Radescu, S. N. Achary, C. Popescu, and M. Bettinelli, "High-pressure polymorphs of gadolinium orthovanadate: X-ray diffraction, Raman spectroscopy, and ab initio calculations," *Physical Review B*, vol. 100, p. 064106, aug 2019. 89

[93] F.-T. Huang, B. Gao, J.-W. Kim, X. Luo, Y. Wang, M.-W. Chu, C.-K. Chang, H.-S. Sheu, and S.-W. Cheong, "Topological defects at octahedral tilting plethora in bi-layered perovskites," *npj Quantum Materials*, vol. 1, p. 16017, dec 2016. 89

[94] F. Pomiro, C. Ablitt, N. C. Bristowe, A. A. Mostofi, C. Won, S.-W. Cheong, and M. S. Senn, "From first- to second-order phase transitions in hybrid improper ferroelectrics through entropy stabilization," *Physical Review B*, vol. 102, p. 014101, jul 2020. 92

[95] Y. Feng, "Unpublished work," 92, 97

[96] N. C. Harms, "Unpublished work," 92, 94

[97] F. T. Huang, F. Xue, B. Gao, L. H. Wang, X. Luo, W. Cai, X. Z. Lu, J. M. Rondinelli, L. Q. Chen, and S. W. Cheong, "Domain topology and domain switching kinetics in a hybrid improper ferroelectric," *Nature Communications*, vol. 7, p. 11602, sep 2016. 94

[98] V. M. Goldschmidt, "Uber das krystallochemische und geochemische Verhalten des Germaniums," *Die Naturwissenschaften*, vol. 14, pp. 295–297, apr 1926. 94

[99] H. J. Xiang, M. Guennou, J. Íñiguez, J. Kreisel, and L. Bellaiche, "Rules and mechanisms governing octahedral tilts in perovskites under pressure," *Physical Review B*, vol. 96, p. 054102, aug 2017. 96

[100] N. A. Benedek and C. J. Fennie, "Why are there so few perovskite ferroelectrics?," *The Journal of Physical Chemistry C*, vol. 117, pp. 13339–13349, jul 2013. ix, 95

[101] I. D. Brown, "Bond valences—a simple structural model for inorganic chemistry," *Chem. Soc. Rev.*, vol. 7, no. 3, pp. 359–376, 1978. ix, 95

[102] M. W. Lufaso and P. M. Woodward, "Prediction of the crystal structures of perovskites using the software program SPuDS," *Acta Crystallographica Section B Structural Science*, vol. 57, pp. 725–738, dec 2001. ix, 95

[103] M. M. Elcombe, E. H. Kisi, K. D. Hawkins, T. J. White, P. Goodman, and S. Matheson, "Structure determinations for $Ca_3Ti_2O_7$, $Ca_4Ti_3O_{10}$, $Ca_{3.6}Sr_{0.4}Ti_3O_{10}$ and a refinement of $Sr_3Ti_2O_7$," *Acta Crystallographica Section B Structural Science*, vol. 47, pp. 305–314, jun 1991. ix, 95

[104] B. Gao, F.-T. Huang, Y. Wang, J.-W. Kim, L. Wang, S.-J. Lim, and S.-W. Cheong, "Interrelation between domain structures and polarization switching in hybrid improper ferroelectric $Ca_3(Mn,Ti)_2O_7$," *Applied Physics Letters*, vol. 110, p. 222906, may 2017. ix, 95

[105] X. Q. Liu, J. W. Wu, X. X. Shi, H. J. Zhao, H. Y. Zhou, R. H. Qiu, W. Q. Zhang, and X. M. Chen, "Hybrid improper ferroelectricity in Ruddlesden-Popper $Ca_3(Ti,Mn)_2O_7$ ceramics," *Applied Physics Letters*, vol. 106, p. 202903, may 2015. ix, 95

[106] M. V. Lobanov, M. Greenblatt, E. a. N. Caspi, J. D. Jorgensen, D. V. Sheptyakov, B. H. Toby, C. E. Botez, and P. W. Stephens, "Crystal and magnetic structure of the $Ca_3Mn_2O_7$ Ruddlesden–Popper phase: neutron and synchrotron x-ray diffraction study," *Journal of Physics: Condensed Matter*, vol. 16, pp. 5339–5348, jul 2004. ix, 95

[107] P. M. Woodward, "Octahedral tilting in perovskites. I. Geometrical considerations," *Acta Crystallographica Section B Structural Science*, vol. 53, pp. 32–43, feb 1997. 96

[108] J. Zhao, N. L. Ross, and R. J. Angel, "New view of the high-pressure behaviour of $GdFeO_3$-type perovskites," *Acta Crystallographica Section B Structural Science*, vol. 60, pp. 263–271, jun 2004. 96

[109] P. Bouvier and J. Kreisel, "Pressure-induced phase transition in laalo3," *Journal of Physics: Condensed Matter*, vol. 14, no. 15, p. 3981, 2002. 99

[110] K. A. Müller, W. Berlinger, and F. Waldner, "Characteristic structural phase transition in perovskite-type compounds," *Phys. Rev. Lett.*, vol. 21, pp. 814–817, Sep 1968. 99

[111] B. Chakoumakos, D. Schlom, M. Urbanik, and J. Luine, "Thermal expansion of laalo 3 and (la, sr)(al, ta) o 3, substrate materials for superconducting thin-film device applications," *Journal of applied physics*, vol. 83, no. 4, pp. 1979–1982, 1998. 99

[112] R. J. Angel, J. Zhao, and N. L. Ross, "General rules for predicting phase transitions in perovskites due to octahedral tilting," *Physical Review Letters*, vol. 95, p. 025503, jul 2005. 99

[113] T. Tohei, A. Kuwabara, T. Yamamoto, F. Oba, and I. Tanaka, "General rule for displacive phase transitions in perovskite compounds revisited by first principles calculations," *Physical review letters*, vol. 94, no. 3, p. 035502, 2005. 99

[114] S. H. Skjærvø, Q. N. Meier, M. Feygenson, N. A. Spaldin, S. J. L. Billinge, E. S. Bozin, and S. M. Selbach, "Unconventional continuous structural disorder at the order-disorder phase transition in the hexagonal manganites," *Physical Review X*, vol. 9, p. 031001, jul 2019. xx, 103, 113

[115] P. Gao, Z. Chen, T. A. Tyson, T. Wu, K. H. Ahn, Z. Liu, R. Tappero, S. B. Kim, and S.-W. Cheong, "High-pressure structural stability of multiferroic hexagonal RMnO$_3$ (R = Y, Ho, Lu)," *Physical Review B*, vol. 83, p. 224113, jun 2011. 106, 111

[116] S. H. Jabarov, N. T. Dang, S. E. Kichanov, D. P. Kozlenko, L. S. Dubrovinsky, J.-G. Park, S. Lee, A. I. Mammadov, R. Z. Mehdiyeva, B. N. Savenko, N. X. Nghia, L. H. Khiem, N. T. T. Lieu, and L. T. P. Thao, "Crystal structure and vibrational spectra of hexagonal manganites YMnO$_3$ and LuMnO$_3$ under high pressure," *Materials Research Express*, vol. 6, p. 086110, may 2019. 106, 111

[117] C. Lin, J. Liu, X. Li, Y. Li, S. Chu, L. Xiong, and R. Li, "Phase transformation in hexagonal ErMnO$_3$ under high pressure," *Journal of Applied Physics*, vol. 112, p. 113512, dec 2012. 106, 111

[118] L. J. Wang, S. M. Feng, J. L. Zhu, Q. Q. Liu, Y. C. Li, X. D. Li, J. Liu, and C. Q. Jin, "Structure transition of multiferroic hexagonal TmMnO$_3$ compound under high pressure," *High Pressure Research*, vol. 30, pp. 258–264, jun 2010. 106, 111

[119] A. Dwivedi, H. K. Poswal, R. Shukla, S. Velaga, B. D. Sahoo, V. Grover, and M. N. Deo, "High pressure structural investigations on hexagonal YInO$_3$," *High Pressure Research*, vol. 39, pp. 17–35, jan 2019. 106, 111

[120] A. G. Gavriliuk, G. N. Stepanov, I. S. Lyubutin, A. S. Stepin, I. A. Trojan, and V. A. Sidorov, "High pressure studies of magnetic, electronic, and local structure properties in the rare-earth orthoferrites RFeO$_3$ (R = Nd, Lu)," *Hyperfine Interactions*, vol. 126, pp. 305–311, 2000. 109

[121] N. W. Ashcroft and N. D. Merman, *Solid State Physics*. Philadelphia: Saunders College, 1976. 109

[122] E. T. Ritz and N. A. Benedek, "Interplay between phonons and anisotropic elasticity drives negative thermal expansion in $PbTiO_3$," *Physical Review Letters*, vol. 121, p. 255901, dec 2018. 109

[123] K. Sinha, Y. Zhang, X. Jiang, H. Wang, X. Wang, X. Zhang, P. J. Ryan, J.-W. Kim, J. Bowlan, D. A. Yarotski, Y. Li, A. D. DiChiara, X. Cheng, X. Wu, and X. Xu, "Effects of biaxial strain on the improper multiferroicity in $LuFeO_3$ films studied using the restrained thermal expansion method," *Physical Review B*, vol. 95, p. 094110, mar 2017. 111

[124] F.-T. Huang, X. Wang, Y. S. Oh, K. Kurushima, S. Mori, Y. Horibe, and S.-W. Cheong, "Delicate balance between ferroelectricity and antiferroelectricity in hexagonal $InMnO_3$," *Physical Review B*, vol. 87, p. 184109, may 2013. 113

[125] H. A. Bechtel, S. C. Johnson, O. Khatib, E. A. Muller, and M. B. Raschke, "Synchrotron infrared nano-spectroscopy and -imaging," *Surface Science Reports*, vol. 75, p. 100493, aug 2020. 116

[126] E. A. Eliseev, A. N. Morozovska, S. V. Kalinin, Y. Li, J. Shen, M. D. Glinchuk, L.-Q. Chen, and V. Gopalan, "Surface effect on domain wall width in ferroelectrics," *Journal of Applied Physics*, vol. 106, p. 084102, oct 2009. 119

[127] B. Guzelturk, A. B. Mei, L. Zhang, L. Z. Tan, P. Donahue, A. G. Singh, D. G. Schlom, L. W. Martin, and A. M. Lindenberg, "Light-induced currents at domain walls in multiferroic $BiFeO_3$," *Nano Letters*, vol. 20, pp. 145–151, jan 2020. 119

[128] J. Chrosch and E. K. H. Salje, "Temperature dependence of the domain wall width in $LaAlO_3$," *Journal of Applied Physics*, vol. 85, pp. 722–727, jan 1999. 119, 122

[129] G. Catalan, J. Seidel, R. Ramesh, and J. F. Scott, "Domain wall nanoelectronics," *Reviews of Modern Physics*, vol. 84, pp. 119–156, feb 2012. 119, 122

[130] R. Moreno, R. F. L. Evans, S. Khmelevskyi, M. C. Muñoz, R. W. Chantrell, and O. Chubykalo-Fesenko, "Temperature-dependent exchange stiffness and domain wall width in Co," *Physical Review B*, vol. 94, p. 104433, sep 2016. 119, 122

[131] J. Seidel, L. W. Martin, Q. He, Q. Zhan, Y.-H. Chu, A. Rother, M. E. Hawkridge, P. Maksymovych, P. Yu, M. Gajek, N. Balke, S. V. Kalinin, S. Gemming, F. Wang, G. Catalan, J. F. Scott, N. A. Spaldin, J. Orenstein, and R. Ramesh, "Conduction at domain walls in oxide multiferroics," *Nature Materials*, vol. 8, pp. 229–234, mar 2009. 119

[132] J. Seidel, P. Maksymovych, Y. Batra, A. Katan, S.-Y. Yang, Q. He, A. P. Baddorf, S. V. Kalinin, C.-H. Yang, J.-C. Yang, Y.-H. Chu, E. K. H. Salje, H. Wormeester, M. Salmeron, and R. Ramesh, "Domain wall conductivity in La-doped $BiFeO_3$," *Physical Review Letters*, vol. 105, p. 197603, nov 2010. 119

[133] P. Maksymovych, J. Seidel, Y. H. Chu, P. Wu, A. P. Baddorf, L.-Q. Chen, S. V. Kalinin, and R. Ramesh, "Dynamic conductivity of ferroelectric domain walls in $BiFeO_3$," *Nano Letters*, vol. 11, pp. 1906–1912, may 2011. 119

[134] J. Guyonnet, I. Gaponenko, S. Gariglio, and P. Paruch, "Conduction at domain walls in insulating $Pb(Zr_{0.2}Ti_{0.8})O_3$ thin films," *Advanced Materials*, vol. 23, pp. 5377–5382, dec 2011. 119

[135] I. Stolichnov, L. Feigl, L. J. McGilly, T. Sluka, X.-K. Wei, E. Colla, A. Crassous, K. Shapovalov, P. Yudin, A. K. Tagantsev, and N. Setter, "Bent ferroelectric domain walls as reconfigurable metallic-like channels," *Nano Letters*, vol. 15, pp. 8049–8055, dec 2015. 119

[136] L. Liu, K. Xu, Q. Li, J. Daniels, H. Zhou, J. Li, J. Zhu, J. Seidel, and J. Li, "Giant domain wall conductivity in self-assembled $BiFeO_3$ nanocrystals," *Advanced Functional Materials*, vol. 31, p. 2005876, jan 2021. 119

[137] M. Bartels, V. Hagen, M. Burianek, M. Getzlaff, U. Bismayer, and R. Wiesendanger, "Impurity-induced resistivity of ferroelastic domain walls in doped lead phosphate," *Journal of Physics: Condensed Matter*, vol. 15, pp. 957–962, feb 2003. 119

[138] R. K. Vasudevan, W. Wu, J. R. Guest, A. P. Baddorf, A. N. Morozovska, E. A. Eliseev, N. Balke, V. Nagarajan, P. Maksymovych, and S. V. Kalinin, "Domain wall conduction

and polarization-mediated transport in ferroelectrics," *Advanced Functional Materials*, vol. 23, pp. 2592–2616, may 2013. 119

[139] T. Xu, T. Shimada, Y. Araki, J. Wang, and T. Kitamura, "Multiferroic domain walls in ferroelectric $PbTiO_3$ with oxygen deficiency," *Nano Letters*, vol. 16, pp. 454–458, jan 2016. 122

[140] J. A. Seijas-Bellido, C. Escorihuela-Sayalero, M. Royo, M. P. Ljungberg, J. C. Wojdeł, J. Íñiguez, and R. Rurali, "A phononic switch based on ferroelectric domain walls," *Physical Review B*, vol. 96, p. 140101, oct 2017. 122

[141] M. Yelisieiev, P. Maksymovych, and A. N. Morozovska, "Probing phonon softening in ferroelectrics by scanning probe microwave spectroscopy," *Physical Review B*, vol. 104, p. 174105, nov 2021. 122

[142] Y. Kumagai and N. A. Spaldin, "Structural domain walls in polar hexagonal manganites," *Nature Communications*, vol. 4, p. 1540, jun 2013. 122, 127

Vita

Kevin A. Smith Jr. was born in Lock Haven, Pennsylvania. He attended the University of Tennessee between 2010 and 2014 where he received a B. S. degree in Chemistry. Kevin joined the research group of Dr. Janice L. Musfeldt in the summer of 2015 to pursue his Ph.D. degree from the University of Tennessee. His research focuses on the spectroscopic analysis of ferroic oxides using novel, synchrotron-based techniques. Kevin A. Smith Jr. received his Doctor of Philosophy degree from the University of Tennessee in December of 2022.